Computed tomography of critical raw materials: method development and mineralogical characterisation for graphite and tungsten ores

Von der Fakultät für Georessourcen und Materialtechnik der
Rheinisch-Westfälischen Technischen Hochschule Aachen

zur Erlangung des akademischen Grades eines

Doktors der Naturwissenschaften

genehmigte Dissertation

vorgelegt von

Leonard Theodor Krebbers, M.Sc.

Berichter: Herr Univ.-Prof. Dr. Bernd Georg Lottermoser
Herr Prof. Dr. Hylke Glass

Tag der mündlichen Prüfung: 27.03.2025

- this page is intentionally left blank -

Zusammenfassung

Kritische Rohstoffe (KR) sind essenziell für eine moderne Gesellschaft. In dieser Arbeit wurden Graphit und Wolfram als repräsentative Beispiele für KR näher untersucht. Beide Rohstoffe werden hauptsächlich aus komplexen Erzen gewonnen, die sorgfältig charakterisiert werden müssen, um Lagerstätten umfassend bewerten und die Rohstoffgewinnung maximieren zu können. Konventionelle Charakterisierungsmethoden liefern zwar wertvolle Informationen über Mineralogie und Geochemie, erfordern jedoch eine aufwändige, destruktive Probenvorbereitung und sind auf zweidimensionale (2D) Informationen beschränkt. Darüber hinaus kann die Übertragung dieser 2D-Informationen in dreidimensionale (3D) Informationen zu stereologischen Fehlern führen.

Die Röntgen-Computertomographie (CT) ermöglicht eine zerstörungsfreie 3D-Analyse von Objekten auf Basis ihrer Röntgenabschwächung bei einer Auflösung von bis zu 1 µm. In den vergangenen zwei Jahrzehnten hat CT in der Untersuchung von Erzen zunehmend an Bedeutung gewonnen, da sie beispielsweise die räumliche Darstellung von Mineralverteilungen sowie die Quantifizierung von Korngrößen, -formen und -volumen ermöglicht. Die Anwendung von CT zur mineralogischen Charakterisierung von Erzen kann jedoch eine Herausforderung insbesondere aufgrund der unterschiedlichen Röntgenabschwächungseigenschaften verschiedener Minerale und des Fehlens spektraler Informationen darstellen. Deshalb wurden verschiedene Bildaufnahme- und Bildverarbeitungsmethoden entwickelt und eingesetzt, um die Bildqualität zu verbessern und die Menge der extrahierbaren Informationen zu erhöhen. CT wurde vor allem zur Analyse von Gold- und PGE-Erzen verwendet; die Anwendung von CT zur Analyse von Graphit- und Wolframerzen ist bislang unzureichend erforscht. Um eine hinreichende Charakterisierung dieser Erze mit CT zu ermöglichen, ist die Entwicklung geeigneter Analysestrategien unerlässlich.

Die Hauptforschungsfrage dieser Dissertation lautete: „Wie kann CT optimiert werden, um zuverlässige qualitative und quantitative mineralogische Informationen über die kritischen Rohstoffe Graphit und Wolfram in Erzen zu gewinnen?“ Das Hauptforschungsziel bestand in der Untersuchung des Potenzials von CT für die mineralogische Charakterisierung von Graphit- und Wolframerzen. Die Hauptforschungsfrage und das Hauptforschungsziel wurden durch drei begutachtete wissenschaftliche Studien adressiert, die den experimentellen Kern dieser Arbeit bilden. Als Methoden wurden CT mit entsprechender Rekonstruktions- und Verarbeitungssoftware, Röntgendiffraktometrie (XRD), optische Mikroskopie (OM), ultraviolettes (UV) Licht, optische Emissionsspektrometrie mit induktiv gekoppeltem Plasma (ICP-OES), Rasterelektronenmikroskopie gekoppelt mit energiedispersiver Röntgenspektroskopie (SEM-EDS) sowie eine SEM-basierte automatisierte Mineralogie-Software eingesetzt.

Studie 1 untersuchte die Eignung von CT zur Charakterisierung von Flockengraphiterz. Dabei lag der Schwerpunkt auf der Entwicklung eines CT-Analyseprotokolls, um wichtige mineralogische Eigenschaften von Graphit zu bestimmen. Unter Berücksichtigung der mineralogischen Zusammensetzung des Erzes und der heterogenen Abschwächungseigenschaften, die mit her-

kömmlichen mineralogischen Methoden identifiziert wurden, konnten hochwertige CT-Daten aufgenommen werden. Die Anwendung von Deep Learning (DL)-basierten Segmentierungsstrategien führte zu einer Reduktion der inhärenten Einschränkungen von CT-Bilddaten, die sich aus der ähnlichen Röntgenabschwächung von Graphit und Silikatmineralen ergaben. Das entwickelte Analyseprotokoll ermöglichte eine genaue quantitative Analyse der Graphitflockengrößenverteilung, -form, -verunreinigungen und des Gesamtgraphitgehalts. Die Validierung mit herkömmlichen Methoden bestätigte die Genauigkeit der Daten und zeigte den Mehrwert der CT für die mineralogische Charakterisierung von Flockengraphiterz auf.

Da die Röntgenabschwächung der Phasen mit der eingestellten Röntgenenergie variiert und damit den Bildkontrast bestimmt, wurde in der zweiten Studie die Effektivität der Dual-Energy-CT (DECT) zur Verbesserung der Bildqualität untersucht. Dazu wurde ein sequentieller Fusionsansatz bei einer Graphiterzprobe angewendet, um CT-Daten aus verschiedenen Single-Energy-CT (SECT) Scans mit hoher räumlicher Auflösung vor der Rekonstruktion zu kombinieren und DECT-Daten zu erzeugen. Zusätzlich wurden unterschiedliche Gewichtungsfaktoren angewendet, um den optimalen Beitrag der verwendeten Energiespektren zu ermitteln. Die Ergebnisse zeigten, dass alle DECT-Datensätze im Vergleich zu den SECT-Datensätzen einen signifikant verbesserten Bildkontrast aufwiesen. Darüber hinaus erwies sich die entwickelte Methode zur Messung der Bildqualität als effektiv für den quantitativen Vergleich von Datensätzen mit heterogenen Grauwertinformationen.

Während in den Studien 1 und 2 der Schwerpunkt auf der Methodenentwicklung lag, handelte es sich bei Studie 3 um eine Fallstudie, bei der zwei Scheeliterzproben aus der australischen Fe-W-Lagerstätte Kara mittels CT untersucht wurden. Ziel der Studie war die Bestimmung der modalen Mineralogie und des Wolframgehalts sowie die Untersuchung des Erzgefüges. Zu diesem Zweck wurde das in Studie 1 entwickelte CT-Analyseprotokoll angewendet und unter Berücksichtigung der spezifischen mineralogischen Eigenschaften der Erzproben optimiert. Zusätzlich wurde das in Studie 2 entwickelte CT-Fusionsverfahren auf eine Probe angewendet. Die Untersuchung ergab, dass Scheelit hauptsächlich mit wasserhaltigen Phasen vergesellschaftet war und überwiegend als massive oder disseminierte Aderfüllung in geringer Konzentration beziehungsweise in Spuren vorkam. Die Studie zeigte, dass CT eine genaue 3D-Visualisierung der Textur von Scheeliterz ermöglichte und valide quantitative Daten zur modalen Mineralogie sowie zum WO_3-Gehalt der untersuchten Proben lieferte. Die gewonnenen Informationen tragen somit zum Verständnis der Erzgenese und zur Entwicklung geeigneter Aufbereitungsstrategien von Scheelit aus der Fe-W-Lagerstätte Kara bei.

Die Synthese der Forschungsergebnisse zeigte, dass durch die Entwicklung spezieller Analyseprotokolle gültige und genaue mineralogische 3D-Informationen von Graphit- und Wolframerz gewonnen werden konnten, die den Mehrwert der CT bei der Anwendung auf diese Erze verdeutlichen. Die Fähigkeit, graustufenkontrastbedingte Analyseeinschränkungen zu verringern, insbesondere durch den Einsatz der DL-basierten Segmentierung, stellt einen bedeutenden Fortschritt in der CT-Erzanalyse dar. Obwohl CT für Graphit- und Wolframerze optimiert wurde, bieten die entwickelten Strategien die Möglichkeit, auch auf andere komplexe Erze mit ähnlichen mineralogischen Eigenschaften erfolgreich angewendet zu werden. Somit trägt diese Arbeit zur methodischen Entwicklung und einer breiteren Anwendung von CT in der Erzanalyse bei. Allerdings bestehen nach wie vor inhärente methodische Schwächen, die in Verbindung mit langen Analysezeiten, Probenkomplexität, begrenzter Standardisierung und hohen Analysekosten erhebliche Einschränkungen für die breite Nutzung von CT im Bergbausektor darstellen. Aktuelle

und zukünftige Forschung, die sich auf die Integration von künstlicher Intelligenz entlang der CT-Analysekette und Automatisierung konzentriert, könnte diese Einschränkungen erheblich verringern.

- this page is intentionally left blank -

Abstract

Critical raw materials (CRMs) are essential to modern society, with graphite and tungsten serving as two examples in this work. Graphite and tungsten are primarily sourced from complex ores requiring rigorous characterisation for evaluating ore deposit quality and maximising recovery. Conventional characterisation methods, while providing essential insights into the mineralogy and geochemistry of ores, involve destructive sample preparation, require careful sectioning and are limited to two-dimensional (2D) information. Moreover, translating this 2D information into three-dimensional (3D) information can introduce stereological bias.

X-ray computed tomography (CT) allows for non-destructive 3D analysis of both bulk volume and spatially resolved microstructures of scanned objects, based on the X-ray attenuation information of their constituents, with a resolution down to 1 μm. Over the past two decades, CT has gained increasing attention in the study of ores, enabling, for example, the spatial visualisation of mineral distributions and quantification of grain sizes, shapes and volumes. However, applying CT in ore characterisation presents challenges, particularly due to the varying X-ray attenuation properties of different minerals and the lack of spectral information. To address these challenges, several acquisition and image processing methods have been developed and applied to enhance image quality and the amount of extractable mineralogical information, optimising CT for specific ores. Against this background, CT has been particularly successful in analysing gold and PGE ores. In contrast, the comprehensive mineralogical characterisation of graphite and tungsten ores remains relatively underexplored, highlighting the need for proper CT analysis protocols.

This thesis addressed these gaps and aimed to answer the main research question: 'How can CT be optimised for the characterisation of the critical raw materials graphite and tungsten ores, to obtain reliable qualitative and quantitative mineralogical information?' The main research aim was to investigate the potential of CT for the characterisation of graphite and tungsten ores. The main research question and the main research aim were addressed through three peer-reviewed scientific studies, forming the experimental work of this thesis. The methods employed included CT with corresponding reconstruction and processing software, X-ray diffraction (XRD), optical microscopy (OM), ultraviolet (UV) light, inductively coupled plasma optical emission spectroscopy (ICP-OES), scanning electron microscopy coupled with energy-dispersive X-ray spectroscopy (SEM-EDS) as well as SEM-based automated mineralogy software.

Study 1 evaluated the potential of CT for characterising flake graphite ore, focusing on the development of a CT analysis protocol in order to establish critical mineralogical aspects. By considering the ore's mineralogical composition, accounting for the heterogeneous attenuation characteristics identified using conventional mineralogical methods, high-quality CT data were acquired. The application of deep learning (DL)-based segmentation strategies successfully reduced inherent limitations associated with CT image data, resulting from the similar X-ray attenuation properties of graphite and silicate minerals. The protocol developed enabled accurate quantit-

ative analysis of graphite flake size distribution, shape, impurities, and overall graphite content. Validation against conventional methods confirmed the accuracy of the data, demonstrating the added value of CT for the mineralogical characterisation of flake graphite ore.

Study 2 addressed the constraints related to the limited grey value contrast of similar X-ray attenuating materials such as graphite and silicates. Considering that the X-ray attenuation properties of the phases vary with the X-ray energy applied, this study investigated the effectiveness of dual-energy CT for improving image contrast. A sequential fusion approach was employed on a graphite ore sample to combine CT data obtained from different single-energy CT (SECT) scans at high spatial resolution prior to reconstruction, establishing dual-energy CT (DECT) data. In addition, varying weighting factors were applied to determine the optimal contribution of each energy level and spectrum. To evaluate the image quality obtained, a method was developed for quantitatively measuring the image contrast between individual phases. The findings demonstrated that all DECT datasets showed significantly improved image contrast compared to SECT datasets. Furthermore, the image quality measure method developed proved to be an effective tool for comparing image quality between multi-material datasets comprising heterogeneous grey value information.

While studies 1 and 2 primarily focused on method development, study 3 formed a case study. Two scheelite ore samples from the Australian Kara Fe-W deposit were examined using CT to establish modal mineralogy, mineral textures, scheelite distribution and tungsten grade. The CT analysis workflow developed in study 1 was applied and optimised to the ores' specific mineralogical properties. In addition, the fusion approach developed in study 2 was applied to increase the image quality, mitigating acquisition issues. The results showed that scheelite was primarily associated with hydrous phases and occurred predominantly as massive or disseminated vein-fill mineralisation at minor and trace concentrations. The study demonstrated that CT of scheelite ore enabled accurate 3D texture visualisation and yielded valid quantitative data on modal mineralogy and WO_3 grade of the samples investigated, ultimately providing relevant information on ore formation and for comminution strategies of scheelite at the Kara Fe-W deposit.

The synthesis of the research findings showed that by developing dedicated analysis protocols, reliable mineralogical 3D information of graphite and tungsten ore was generated, showcasing the added value of CT applied to these ores. The ability to reduce greyscale contrast-based analysis constraints, particularly through the use of DL-based segmentation, marks a significant advancement in CT ore analysis. While CT was optimised for graphite and tungsten ores, the strategies developed hold potential for application to other complex ores with similar mineralogical characteristics, contributing to broader applications of CT. However, inherent methodological constraints persist, which, in conjunction with extended analysis time, sample complexity and limited standardisation, present a significant barrier to adoption in the raw materials sector, particularly for operators. Future research focusing on integrating AI along the CT analysis chain and automatisation could significantly lower this barrier.

Acknowledgements

I am deeply grateful to Univ.-Prof. Dr. Bernd Lottermoser for granting me the opportunity to undertake my doctoral project, providing the essential infrastructure and resources needed. His mentorship throughout my doctoral studies has significantly contributed to the development of my scientific skills. My sincere thanks also extend to Prof. Dr. Hylke Glass for his time and effort in supporting my research, as well as for his guidance and stimulation at international conferences.

I am thankful to the entire MRE staff for fostering a supportive and engaging environment at the MRE Institute, which greatly enriched my experience over the four years spent together. In this context, I appreciate my friend Nils Schlatter, for the scientific exchange that enriched every phase of my studies. Furthermore, I wish to express my sincere gratitude to my friend Dr. Johannes Sieger and my former colleague Dr. Stephanie Lohmeier for their fruitful discussions and providing constant and invaluable feedback throughout my work.

I would like to thank Natalia Grozmani for introducing me to the research field of DECT; our numerous discussions have deepened my knowledge in this area. Additionally, I am grateful to Dr. Julie Hunt for her support during my third study phase. I am also thankful for the assistance of my Master's and Bachelor's students, particularly Xinmeng Liu and Ytong Qian, helping in preparing some of the experimental work.

My appreciation goes to the staff at the AMR Institute, especially Devrim Güersel, Vincent Merz, and Christoph Stepphuhn, for allowing me to utilise their infrastructure whenever needed. I extend my gratitude to Dr. Sven Sindern and Roman Klinghardt for providing me with the opportunity to perform SEM-EDS analysis, which was vital for my research. I am grateful to NGS Graphite for supplying the graphite samples and sharing their expertise, and to Michael Köhler from MKfactory for preparing the samples for my experiments.

I also would like to thank my family for their support, especially my parents, for having always given me the freedom to pursue my path. Last but certainly not least, I owe my deepest gratitude to my dear girlfriend, Hannah, for her relentless patience and unwavering support throughout my doctoral studies. Her encouragement was indispensable at every step, and I cannot express enough how grateful I am. Thank you my love.

- this page is intentionally left blank -

Publications related to this thesis

Peer-reviewed articles

L. T. Krebbers, B. G. Lottermoser, X. Liu, Computed tomography of flake graphite ore: Data acquisition and image processing, Minerals 13 (2) (2023) 247. doi:10.3390/min13020247.

L. T. Krebbers, N. Grozmani, B. G. Lottermoser, R. H. Schmitt, Dual-energy computed tomography for improved contrast on a polyphase graphitic ore, Tomography of Materials and Structures 4 (100021) (2024). doi:10.1016/j.tmater.2023.100021.

L. T. Krebbers, J. A. Hunt, B. G. Lottermoser, Computed tomography of scheelite ore, Kara, Australia: Morphological characterisation and modal mineralogy, Minerals 14 (4) (2024) 345. doi:10.3390/min13020247.

Conference contributions

L. T. Krebbers, B. G. Lottermoser, S. Safari, D. Alessi, Computed tomography of graphite ore: implications for product use, in: Geometallurgy, 7 - 8 July 2022, London (United Kingdom).

L. T. Krebbers, B. G. Lottermoser, X. Liu, Mineralogical analysis of flake graphite ore using computed tomography, in: 1st European Conference on Teaching and Research in Sustainable Resource Extraction: TERRA, 6 - 8 September 2023, Boppard (Germany).

Other

L. Krebbers, Gainov, Ramil, B.G. Lottermoser, A. Hennig, S. Lohmeier, Applications of industrial computed tomography in the mining sector, Mining Report: Glückauf! 157 (4) (2021).

L. T. Krebbers, N. Grozmani, B. G. Lottermoser, R. H. Schmitt, Application of multi spectral computed tomography for the characterisation of natural graphite, e-Journal of Nondestructive Testing 28 (3) (2023). doi:10.58286/27710.

- this page is intentionally left blank -

Contributors to this thesis

Main author

Leonard T. Krebbers is the principal author and administrator of this dissertation, responsible for the conceptualisation, research design, investigation, and formal analysis, ultimately providing the original drafts for all peer-reviewed articles and this manuscript.

Co-authors of peer-reviewed articles

Bernd G. Lottermoser, co-author of all articles and supervisor of this thesis, offered invaluable feedback on the thesis concept, article drafts, and the draft version of this thesis.

Xinmeng Liu, co-author of the first article, provided valuable support in the formal analysis and investigation of the experimental data.

Natalia Grozmani, co-author of the second study, contributed to the conceptualisation, investigation and formal analysis. In addition, she reviewed the draft version of the article and provided valuable support during the revision process.

Julie Hunt, co-author of the third article, acquired the sample material, supplied some of the mineralogical analysis and provided valuable feedback on the research design and original draft.

- this page is intentionally left blank -

Contents

- this page is intentionally left blank -

List of Figures

List of Tables

List of abbreviations, acronyms and symbols

2θ	Scattering angle (X-ray diffraction parameter)
2D	Two dimensional
3D	Three dimensional
AI	Artificial intelligence
AMICS	Advanced Mineral Identification and Characterisation System
CL	Cathodoluminescence
CNN	Convolutional neural network
CNR	Contrast-to-noise ratio
Co	Cobalt
CRM	Critical Raw Material
CT	Computed tomography
DECT	Dual-energy computed tomography
DL	Deep learning
DTA	Differential thermal analysis
e.g.	for instance (Latin: exempli gratia)
EMPA	Electron probe micro-analysis
Eq.	Equation
ESD	Equivalent sphere diameter
EU	European Union
Fe	Iron
Fig.	Figure
HCl	Hydrochloric acid
HNO_3	Nitric acid
ICP-MS	Inductively coupled plasma mass spectrometry
ICP-OES	inductively coupled plasma optical emission spectroscopy
LA-ICP-MS	Laser ablation inductively coupled plasma mass spectrometry

LIB	Lithium-ion battery
MA	Material area
max	Maximum
min	Minimum
ML	Machine learning
MLA	Mineral Liberation Analyser
n	Number
OM	Optical microscopy
PGE	Platinum group elements
PPL	Plane polarised light
PVE	Partial volume effect
QEMSCAN	Quantitative evaluation of minerals by scanning electron microscopy
QXRD	Quantitative X-ray diffraction
ROI	Region of interest
SECT	Single-energy computed tomography
SEM	Scanning electron microscopy
SEM-EDS	Scanning electron microscopy with energy-dispersive X-ray spectroscopy
SIMS	Secondary ion mass spectrometry
SNR	Signal-to-noise ratio
TG	Thermogravimetry
UV	Ultra violet
W	Tungsten
WO_3	Tungsten trioxide
wt.	Weight
XRD	X-ray diffraction
XRF	X-ray fluorescence analysis
Z	Atomic number
Z_{eff}	Effective atomic number
μ	Linear attenuation coefficient
µXRF	Micro X-ray fluorescence analysis
π	Pi

List of units

cm	Centimetre
cm^3	Cubic centimetre
g	Gram
keV	Kilo electron volt
kV	Kilo volt
L	Litre
mA	Milli Ampere
MeV	Mega electron volt
mg	Milligram
mm	Millimetre
mm^2	Square millimetre
mm^3	Cubic millimetre
nA	Nano Ampere
W	Watt
µm	Micrometre

Chapter 1

General introduction

This chapter contextualises this cumulative thesis by outlining the motivation, providing essential background information, and reviewing the development of computed tomography (CT) in the light of ore characterisation to identify research gaps. The main research question and aim are subsequently derived, with the thesis structure and significance detailed in the final two sections of the chapter. Further information on selected terms used in this manuscript is compiled in a Glossary at the end of this thesis (p. 107ff).

1.1 Motivation

From ancient stone tools to complex electronics powering modern society, raw materials have always been the foundation for technological advancements [1–3]. Today, confronting the climate crisis, the transition to green technologies as outlined in the European green deal depends on a specific group of raw materials: Critical Raw Materials (CRMs) [4]. CRMs, as defined by the EU, encompass a range of elements, metals, minerals, or substances that possess high economic value coupled with a significant supply risk [5–7] and are mainly derived from complex ores (cf. Glossary, p. 107ff) [8–11]. Two prominent CRMs are graphite, a major component in lithium-ion batteries [12], and tungsten, essential for high-performance alloys [13], serving as two examples in this work.

Efficient and responsible sourcing of graphite and tungsten requires a sound understanding of the geological, mineralogical, and geochemical characteristics of their ore deposits [14–16]. This knowledge is fundamental for making informed decisions throughout the mining lifecycle—from exploration to mine closure. Therefore, a comprehensive characterisation of these ores is crucial to develop efficient and sustainable strategies that optimise extraction and mineral processing, maximising resource utilisation and minimising waste [14–16].

Traditional characterisation of graphite and tungsten ores typically involves various well-established techniques, such as optical microscopy (OM), X-ray diffraction (XRD), scanning electron microscopy with energy dispersive spectrometry (SEM-EDS), inductively coupled plasma mass spectrometry (ICP-MS), and X-ray fluorescence analysis (XRF). While ICP-MS and XRF provide valuable bulk chemical information, XRD offers insights into the main mineralogical composition. Imaging techniques like OM, SEM-EDS, and SEM-based automated mineralogy systems such as Advanced Mineral Identification and Characterisation System (AMICS) offer critical mineralogical data on composition and ore texture (cf. Glossary, p. 107ff) including mineral size, habit,

spatial distribution, and associations, yielding two-dimensional (2D) information [17, 18]. However, these methods are time-consuming, destructive, and rely on careful sectioning of samples to obtain representative material information. Furthermore, translating 2D analysis results into the third dimension (3D) can introduce stereological bias, as the selected cross-section may not reflect the actual distribution, sizes and spatial relationships of the constituents within the ore [19, 20], potentially leading to inaccuracies in the analysis.

Since graphite and tungsten ores and their derived products are inherently 3D structures, a comprehensive understanding of their mineralogy and texture requires tools capable of capturing this information in 3D. Computed tomography (CT) is a X-ray computerised imaging method for studying multicomponent materials and constructions in a 3D regime. It is currently the only non-destructive method that allows the observation and analysis of internal and external microstructures of objects without exhaustive sample preparation and without strong limitations on the size, typically up to 5 cm for CT applications in the geosciences [21], and the shape of the objects studied [21].

While being well established in fields such as medicine, dimensional metrology and additive manufacturing [e.g., 22–25], CT has gained increasing attention in the geosciences and the raw materials sector in the past two decades, including the study of ores [21, 26]. CT enables the identification and visualisation of minerals within ore samples based on their X-ray attenuation properties, allowing 3D analysis of mineral distributions and spatial relationships [21]. It has been used to examine mineral textures, providing information on grain size, shape and orientation [21, 27]. However, effective CT analysis is not without challenges. Since CT does not provide spectral information for direct phase identification, the quality and success of the analysis depends on various factors, including the inherent properties of the ore (e.g., mineral density and effective atomic number (Z_{eff}) (cf. Glossary, p. 107ff) and the developed analysis protocol (e.g., image acquisition and processing strategies). For example, low-density minerals like graphite require different scanning parameters than high-density phases such as tungsten containing scheelite. Moreover, mineral differentiation becomes more challenging when ores contain minerals with similar X-ray absorption properties [28].

Historically, CT has been successfully applied to ores like gold and platinum group elements (PGEs), where target minerals (cf. Glossary, p. 107ff) exhibit sufficient X-ray attenuation contrast relative to the gangue [e.g., 26, 29–32]. However, its application to CRMs like graphite and tungsten ores—characterised by heterogeneous mineralogy and textures—remains underexplored. Notably, only a few studies have focused on using CT for graphite ores [33, 34] and tungsten ores [35, 36], with no research dedicated to a comprehensive mineralogical characterisation of these ores.

This thesis addresses these gaps and investigates the potential of CT for the mineralogical characterisation of graphite and tungsten ores. By developing proper acquisition protocols and image processing strategies CT workflows are established optimised to these ores' properties to obtain high-quality CT data. The findings of this thesis will be of significance for the optimal utilisation of CT in the context of graphite and tungsten ores. In addition, this thesis will contribute to the existing body of knowledge, aiding in the development of CT for ore characterisation. Finally, the results presented in this work will serve as a foundation for future research that may result in a better understanding of other types of CRM ores and thus contribute to more sustainable mining practices.

1.2 Background - computed tomography

CT scanners consist of an X-ray source, a detector, and a rotary sample stage positioned between them (Fig. 1.1A), on which the sample to be scanned is mounted. During a CT measurement procedure, a conical X-ray beam is emitted from the source and traveses the specimen which rotates through a range of angles, typically spanning up to 360°. As the X-rays interact with the material, their intensity is attenuated based on the materials density, Z_{eff}, thickness and the X-ray energy applied [37, 38]. The detector captures the intensity of the transmitted X-rays and converts it into a raw image projection, or projection (cf. Glossary, p. 107ff). This process is repeated as the stage rotates, thereby generating a series of projections from different angular positions. The resulting projection data is then computationally reconstructed to generate 2D image slices and a 3D volumetric representation of the specimen, which can be further processed for segmentation tasks and feature extraction [28, 39].

The following subsections will delve into the principles of CT analysis (Fig. 1.1B), including X-ray generation, X-ray attenuation, raw data collection, reconstruction and image processing. The technical specifications of the CT scanner employed for the experimental work performed can be found in Appendix A.

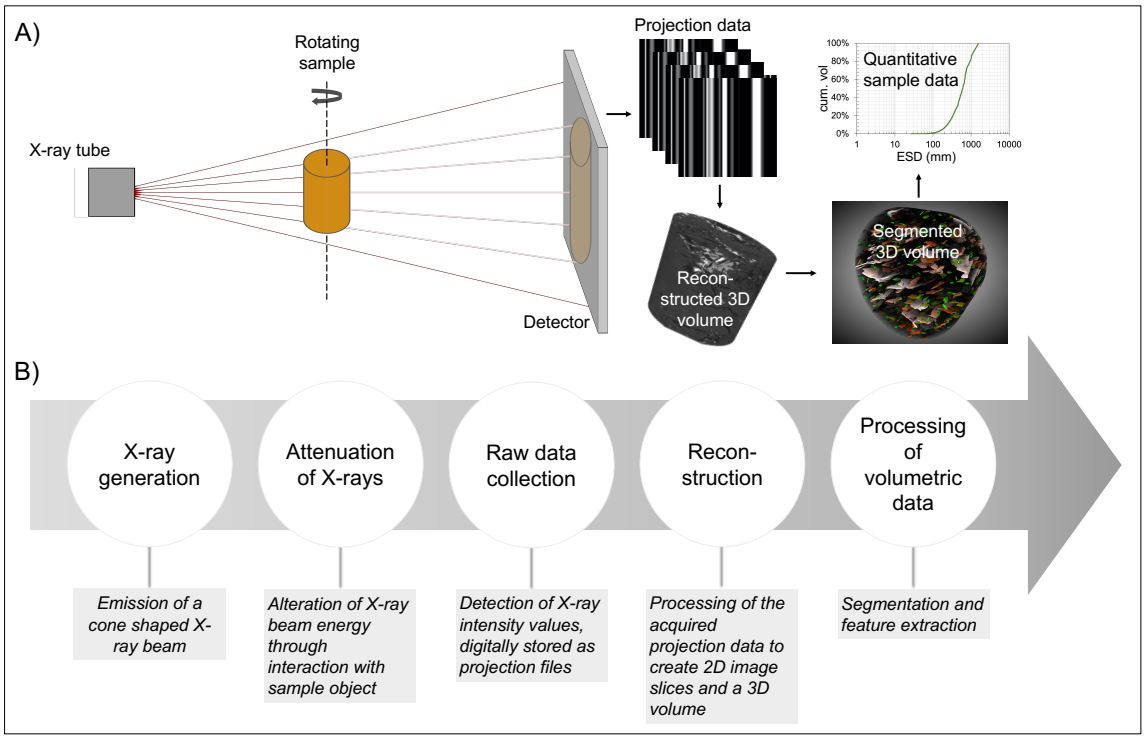

Figure 1.1: CT analysis: **A**) Schematic representation of a CT scan and the subsequent computerised processes. **B**) CT analysis principles and general processing steps.

1.2.1 X-ray generation

X-rays, a form of electromagnetic radiation, are usually generated within an X-ray tube [40]. In this process, a high voltage (cf. Glossary, p. 107ff) is applied to accelerate electrons emitted by a heated filament. These electrons are then directed towards a positively charged anode,

typically composed of tungsten. As electrons collide with the anode, they produce X-rays through bremsstrahlung, where deceleration results in energy emission. This process generates a broad spectrum of energies, forming a polychromatic X-ray beam [40].

A further type of X-rays produced by the X-ray tube is characteristic X-ray emission. Such X-rays occur when the high-energy electrons collide with inner shell electrons of the anode material, causing the removal of these electrons from their orbits. Subsequent filling of these vacancies by outer-shell electrons releases energy in the form of characteristic X-rays, which possess discrete energies characteristic of the anode material [40]. The proportion of bremsstrahlung and characteristic X-rays in the emitted polychromatic X-ray beam depends on various factors, including the accelerating voltage applied to the X-ray tube and the atomic composition of the anode material. While the exact proportions can vary, a typical estimation is that bremsstrahlung radiation accounts for ≥75% of the X-ray intensity, while characteristic X-rays contribute to ≤25% [41].

1.2.2 X-ray attenuation

When X-rays interact with matter, one can measure the attenuation of the initial intensity. Thus, X-ray attenuation describes the reduction in energy of an X-ray beam as it passes through an object. This attenuation results from interactions between the X-ray photons and the object's material properties mentioned earlier (density, Z_{eff}, and thickness) [37, 38]. The extend of the attenuation is proportional to the increase in these parameters. For example, high-density phases attenuate more X-rays than low-density phases [28].

In general, four mechanisms contribute to X-ray attenuation, namely, (1) photoelectric absorption, (2) Compton scattering, (3) pair production, and (4) coherent scattering. The relative significance of each mechanism varies with the X-ray energy applied. For instance, pair production predominates at X-ray energies greater than 1.02 MeV [42], while coherent scattering is notable at very low X-ray energies, typically below 10 keV [42]. However, in the context of this thesis, pair production and coherent scattering can be disregarded as the X-ray energies employed in this study ranged between 60 kV and 190 kV. Consequently, the photoelectric absorption and Compton scattering are the major prevailing mechanisms.

1. *Photoelectric Absorption*: This process occurs when an X-ray photon interacts with an inner shell electron of an atom, transferring its entire energy to eject the electron from its orbit [42]. The energy difference between the initial and final states of the atom is then emitted as a characteristic X-ray photon. The probability of photoelectric absorption is strongly influenced by the atomic number (Z) of the material and the X-ray energy. It dominates at lower energies (approximately 50-100 keV) and is proportional to Z^{4-5}.

2. *Compton Scattering*: This becomes the dominant process at higher X-ray energies (>5 MeV). It involves the interaction between an X-ray photon and a loosely bound outer-shell electron, where the photon imparts only part of its energy to the electron, causing it to recoil and the scattered photon to change direction [43]. Compton scattering is more dependent on the material's electron density than its atomic number and is less sensitive to material composition, especially at lower energies. The probability of Compton scattering depends more on the overall electron density of the material than its atomic number. This makes Compton scattering less sensitive to the specific material composition compared to the photoelectric effect, especially at lower energies.

The X-ray attenuation is quantified by the Beer-Lambert law [44]. The law states that the intensity of the X-ray beam $I(x)$ after passing through a homogenous material with the thickness x is related to the initial intensity I_0 and the linear attenuation coefficient μ of the material according to the equation:

$$I(x) = I_0 \cdot e^{-\mu x} \tag{1.1}$$

whereby μ represents the probability of X-ray interaction (absorption or scattering) within the material per unit length. It is a constant that describes the fraction of attenuated incident photons and is influenced by the material's Z_{eff} and density. Materials with higher μ values have a greater likelihood of interacting with X-rays, leading to a higher rate of intensity reduction in the beam [45].

1.2.3 Raw data collection

Converting X-ray attenuation information to raw data is the actual computerisation process in CT [24]. Eq. (1.1) assumes a uniform material (μ = constant). For inhomogeneous materials, such as ores, typically comprising various minerals with different attenuation properties, Eq. (1.1) needs to be modified as a single μ is inadequate. Hence, it must be supplemented with a line integral (cf. Glossary, p. 107ff) that considers different materials with varying $\mu(x)$ along the X-ray beam's travel path d:

$$I(d) = I_0 \cdot e^{-\int_0^d \mu(x)dx} \tag{1.2}$$

where $I(d)$ is the intesity of the X-ray beam after traveling a distance d through the object, accounting for the cumulative effect of the varying $\mu(x)$ along the path. To adapt the relation to a polychromatic X-ray beam spectrum, Eq. (1.2) must be further modified to to account for varying photon energies:

$$I(d) = \int_0^{E_{max}} I_0(E) \cdot e^{-\int_0^d \mu(E,x)dx} dE \tag{1.3}$$

whereby $I_0(E)$ represents the initial intensity at each energy level E, and $\mu(E,x)$ represents the attenuation coefficient as a function of both energy and position along the beam path (d).

However, as the spectral data is irretrievably lost during the acquisition process in conventional CT, the spectral component in Eq. (1.3) must be disregarded. Therefore, mathematical algorithms for CT reconstructions extracting the attenuation information are usually based on Eq. (1.2) assuming a monochromatic X-ray beam. In addition, considering the rotation of the object during a CT scan, the beam angle θ must be included to the formula resulting in:

$$p(d_\theta) = -ln\frac{I(d_\theta)}{I_0} = \int_0^{d_\theta} \mu(x)dx. \tag{1.4}$$

Eq. (1.4) represents the projection image $p(d_\theta)$, acquired at given d and θ, which is proportional to the integrated attenuation coefficient of a sample from a certain beam direction.

Acquisition parameters

To acquire CT projection data, a set of scanning parameters including voltage, beam current, exposure time, frame averaging, number of projections, pre-filtering, and focal spot size (cf. Glossary, p. 107ff) must be applied affecting the X-ray beam properties and attenuation by the material and consequently the image quality [46]. General information on scanning parameters can be

found in [47]. The overall image quality is influenced by signal-to-noise ratio (SNR), spatial resolution (cf. Glossary, p. 107ff), and image contrast [44]. Selecting the optimal scanning parameters requires careful consideration of the sample's properties (e.g., size, mineralogical composition) to obtain high image quality. Striking the right balance between these factors can be challenging, yet essential for establishing CT data suitable for effective ore analysis.

1.2.4 Reconstruction

Reconstruction in CT bridges the gap between the acquired X-ray projection data and the 3D representation of the scanned object. This computational process involves mathematically transforming a series of one-dimensional (1D) X-ray intensity measurements (line integrals, Eq. (1.4)), acquired at various angles around the object, into a 2D image. The most widely used reconstruction method is filtered back projection (FBP) (cf. Glossary, p. 107ff), which applies the Fourier transform to process the projection data. This transformation is carried out by a reconstruction software, which, following the completion of the reconstruction operation, renders the 2D images into a 3D volume. This volume is represented as a cubical matrix of greyscale voxels (3D pixels), each voxel assigned a grey value based on the calculated X-ray attenuation coefficient for the corresponding region in the scanned object, thereby reflecting the local density and effective atomic number of the material. The reconstruction process is computationally demanding, and while a detailed mathematical explanation of FBP is beyond the scope of this thesis, further information is available in the literature [24, 48]. The reconstruction software used in this work was VGStudio Max 3.5 [49].

Scanning artefacts

Neglecting the spectral information in Eq. (1.4) used to generate a CT projection can lead to inconsistencies and scanning artefacts (cf. Glossary, p. 107ff) in the reconstructed CT data. These appear as structures in the reconstructed image that do not correspond to real features within the scanned object. Artefacts arise from discrepancies between the actual attenuation properties of the object and the values used during image reconstruction. The most prominent artefact is beam hardening (cf. Glossary, p. 107ff). A detailed summary on scanning artefacts can be found in [50].

1.2.5 Image processing

Image filtering

The reconstructed CT data can be affected by image noise, scanning artefacts or low contrast. In this case, digital image filters can be applied to enhance the image quality by smoothing the image or increasing image sharpness [28, 39]. Despite being a useful and effective step, it is important to note that filtering alters the original CT dataset, impacting the accuracy and reliability of subsequent analyses and data interpretation [51].

Segmentation

Segmentation refers to the process of digitally partitioning the 3D image data into distinct regions within the object [52], facilitating their visualisation and analysis. It involves identifying and isolating voxels with similar features (e.g., grey values, textures) into discrete group of voxels (classes). In the context of ore analysis, segmentation classifies voxels into different mineral phases or mineral groups within the reconstructed data, providing insights into mineralogical composition

and textural information such as grain size, volume, and shape. There are various segmentation techniques applied in literature [e.g., 27, 53, 54]. However, given the scope of this work, only thresholding and watershed segmentation, representing conventional segmentation techniques, as well as artificial intelligence (AI)-based methods (cf. Glossary, p. 107ff), representing advanced segmentation techniques [55, 56], will be described in the following.

Conventional segmentation Thresholding is a common segmentation technique where classes are identified based on their grey value differences. It divides the grey value histogram of reconstructed CT data into classes with each class representing the grey value range of a specific mineral or mineral group. This process involves selecting a threshold value that separates the greyscale intensities of different mineral phases. Pixels with intensities above the threshold are typically assigned to one class, while those below are assigned to another [57]. It is either used as a pre-processing segmentation step to generate a binary image for an additional segmentation algorithm, or as a primary step. The accuracy of this method depends upon the choice of the threshold value and the degree to which the greyscale values uniquely represent each mineral class [57].

In watershed segmentation, the image is treated as a topographic map, with grey values representing elevation [27]. The algorithm identifies catchment basins and their boundaries. By simulating flooding from marker points within these basins, the algorithm is particularly effective for separating touching or overlapping objects [27]. Similar to the manually chosen threshold value in threshold segmentation, the accuracy of watershed segmentation depends on the correct placement of marker points.

Advanced segmentation AI-based segmentation methods consider both greyscale information and textural features for mineral identification [58]. In this thesis, deep learning (DL)-based segmentation (cf. Glossary, p 107ff) was employed. Deep learning is a subset of machine learning in which artificial neural networks are trained on large datasets to learn patterns and features directly from the data [59]. This approach leverages interconnected processors (neurons) organised in layers, emulating the human brain's ability to recognise complex patterns through training. These processors are primarily built on a convolutional neural network (CNN) architecture. While a full elaboration on CNNs is beyond the scope of this thesis, a concise explanation of their operational principles follows. For a comprehensive understanding of deep learning and CNNs, please refer to [59, 60].

The foundation of CNNs lies in their convolutional layers, comprising learnable filters, also known as kernels. These kernels are small matrices that systematically slide across the CT image, performing a mathematical operation known as convolution on each local region. This convolution operation allows the network to detect local features, such as edges, grain boundaries, and shapes, based on the greyscale gradients present in the image. Following each convolutional layer, activation functions attribute significance to the information extracted by the kernels (kernel weights), thereby determining the proportion of information passed to the next layer. This mechanism allows the network to focus on the distinct features (grey values and textures) characteristic of specific mineral classes. Through the stacking of multiple convolutional layers, CNNs progressively build upon these identified local patterns, enabling the extraction of increasingly complex information, including textural variations like grain boundaries and shapes, enabling the recognition of mineral phases.

The ability of CNNs to recognise mineral phases hinges on the processes of training and validation allowing for adjusting the kernel weights. The training process involves presenting the CNN with a set of manually labelled representative regions of different CT image slices, where each pixel is assigned to a class corresponding to a specific mineral. This labelled dataset serves as ground truth data (Glossary, p. 107ff), guiding the network's learning process. Through an iterative process known as backpropagation, the network adjusts its internal parameters (kernel weights) to minimise the discrepancy between its predicted segmentation after a training step and the ground truth labels. This iterative refinement usually requires several manual segmented CT image regions, ultimately enhancing the network's capacity to discern patterns that differentiate mineral phases.

In the present work, the image processing software ORS Dragonfly 2022.1 [61] was used to apply DL-based segmentation. The software features pre-built CNN architectures that can be fine-tuned (e.g., number of kernels, filter sizes) according to the sample's complexity for optimal segmentation performance. The accuracy of the model can be monitored using the Dice score (Glossary p. 107ff) that overlap the discrepancy between the predicted segmentation data and the ground truth data. However, it is important to note that while a high Dice score suggests high accuracy, it does not automatically guarantee correctness of the segmentation result. Once sufficient training has been employed, the model can be applied to the remaining unseen CT image slices to generate a segmented 3D volume.

Feature extraction

Feature extraction, performed using ORS Dragonfly 2022.1, bridges the gap between the visual representation of the segmented sample volume and the quantitative data needed for further analysis and interpretation. By isolating specific visual or spatial characteristics from the segmented CT data, it generates a set of numerical descriptors, or measurements [62] (e.g., grain size, mineral distributions), enabling quantitative analysis of ore characteristics.

1.3 Background - Materials selection

Both graphite and tungsten are designated as CRMs. Graphite is indispensable for the production of lithium-ion batteries, which are essential components of the rapidly growing sectors of electric vehicles and energy storage systems [63]. The mineralogical characteristics of graphite—specifically flake size, shape, and purity—are key determinants of its quality and its suitability for these applications and as such directly related to product price [14]. The flake size is deposit specific and decisive for the economic viability of a deposit, necessitating proper analysis. Tungsten, on the other hand, is typically found in nature in scheelite and wolframite [64], with scheelite being examined in this work. Within the ore, the mineral is often present in very low concentrations, requiring precise mineralogical assessment, for example to determine the degree of recovery achievable during processing, as grain size and distribution significantly impact extraction efficiency [65]. Consequently, advancing the understanding of the mineralogical characteristics of both graphite and tungsten ores is essential to support a secure and sustainable supply of these materials.

From a CT analysis standpoint, graphite and scheelite were selected due to their specific as well as contrasting physical properties, implying different usage of this method. Graphite has a density of 2.26 g/cm³ and an Z_{eff} of 6 (Appendix B), whereas scheelite exhibits a much higher density of

6.1 g/cm³ and a Z_{eff} of ~67 (Appendix B). These differences indicate that the two materials have distinct X-ray attenuation characteristics which may be further influenced by the mineralogical composition and texture of their ores. Therefore it is considered that both graphite and scheelite ores require individual analysis protocols for proper characterisation. For example, in terms of data acquisition, graphite is anticipated to exhibit weak X-ray attenuation owing to its physical properties compared to many ore minerals, and potentially similar X-ray absorption properties compared to common gangue minerals (e.g., quartz, feldspar). In contrast, scheelite has a very high density and large Z_{eff}, which leads to very high X-ray attenuation, suggesting different acquisition settings.

1.4 Review - CT ore analysis

X-ray CT imaging was developed in the early 1970s [66, 67] and revolutionised the field of medical diagnostics by enabling non-invasive visualisation of the human body and brain [68]. Recognising its potential beyond medicine, researchers quickly adapted medical CT (mCT) to other fields including geosciences. From the early 1980s onwards, a surge of publications explored mCT's application in various geoscientific areas, including soil science [69, 70], meteoritics [71], petroleum geology [72, 73], palaeontology [74], and sedimentology [75]. In the 1980s, micro-CT, or industrial CT (hereafter referred to 'CT') emerged [76–78] further expanding the technologies' capabilities. Unlike mCT scanners, CT systems are not constrained by limitations on radiation dose and vivid sample objectives, allowing for the use of higher X-ray energies and longer exposure times, flat-panel detectors, and more precise positioning [79]. Moreover, the smaller sample size (typically between 1 mm and 5 cm in geosciences [80]), allowed the use of a smaller focal spot that enabled significantly improved spatial resolution, reaching down to 1 µm [80]. These developments provided key advances that greatly enhanced the potential for applications of CT to geological investigations (in particular rock analysis) that commenced in the middle of the 1990s [81].

Comprehensive reviews on the history and development of CT are provided by [23, 44, 45]. Various reviews in the context of geosciences [21, 80, 82–84], including ore analysis [21, 26, 27, 54, 85] using CT have been published. These reviews elaborate on the CT fundamentals discussing different scanning techniques and how to acquire and process CT data in general as well as highlighting applications, developments and challenges in the field of ore geology and mineral processing. CT has also been explored for structural, textural characterisation, liberation of ore concentrates [27, 54]. In the following and with regard to the scope of this study, a condensed review is given that provides an overview of the state-of-the-art of CT in ore analysis, focussing on methods developed for data acquisition and processing, specifically for mineralogical characterisation, and the ore types studied. The research gaps are documented in the following Section 1.5.

1.4.1 Ore types studied

CT has been predominantly applied to the study of gold and PGE ores [29–32, 85–96]. These metals are among the highest value mineral commodities, requiring usually only trace concentrations to achieve commercial viability [97, 98]. Their X-ray attenuation properties, significantly different from common gangue minerals (e.g., quartz, feldspar, olivine), enable clear differentiation in CT images. This allowed for effective visualisation of their 3D in situ distribution within the

ores, providing valuable genetic information [32, 85, 87]. In addition, CT has been used to study zinc and iron ores [99, 100]. In terms of CRMs others than PGE's, few studies have investigated copper, chromite and tungsten ores [35, 36, 101–103].

1.4.2 Method development in ore characterisation

Acquisition

Beyond the visualisation and differentiation of ore minerals from gangue, CT has also been employed to differentiate between individual ore minerals that typically exhibit similar X-ray attenuation properties. In this regard, several tools have been developed to aid in optimising CT data acquisition and for maximising mineral differentiation in CT imaging. For example, Mote et al. [95]; Kyle et al. [32] explored to which extent metallic minerals representative of typical assemblages can be distinguished from one another. In addition, the development of a comprehensive X-ray attenuation database [104] has permitted researchers to identify the potential of differentiating between selected ore minerals. On this basis, researchers have developed specific linear attenuation coefficient databases to predict mineral discrimination in high-density ores using CT prior to scanning and analysis, providing valuable guidance for CT experimental design and data interpretation [83, 105–107]. Using their method, Bam et al. [106] found that discriminating between minerals with attenuation coefficient differences of less than 6% is problematic.

In addition, research was carried out to evaluate the impact of different scanning parameters on CT image data of ores with high-density target minerals [100]. Furthermore, synchrotron CT (Glossary, p. 107ff) has been explored to enhance mineral identification [34, 108]. Moreover, researchers have combined spectral information from energy-discriminating detectors with CT to further enhance mineral discrimination. By identifying specific elements based on their unique K-edge absorption energies [109, 110], this approach has provided an additional layer of information beyond conventional X-ray attenuation. Similarly, Ghorbani et al. [99]; Martini et al. [111] combined two energy spectra using dual-energy CT (DECT) to calculate the electron density of minerals and their Z_{eff} comprising the sample, allowing for their identification. Notably, while DECT has been successfully used for contrast enhancement in medical imaging [112], its application for this purpose in ore analysis remains unexplored.

Image processing

Similar to optimising CT data acquisition, researchers have explored a number of segmentation techniques, varying in complexity and computational intensity [27, 54] to isolate individual mineral phases in CT images, enabling the quantification of their mineralogical and textural properties (e.g., grain size, and volume). Thresholding has been successfully used for segmenting between high X-ray absorbing grains and the usually low X-ray absorbing mineral matrix. This method has been effective in determining particles in crushed ores or in quantifying between the high X-ray absorbing minerals and gangue [35, 36, 93, 113, 114]. Similarly, watershed segmentation was used to segment ores, thereby establishing mineralogical and textural information [115]. This technique proved to be more resistant to image noise in CT datasets compared to thresholding [27]. Furthermore, this technique proved effective in separating between touching grains of ore particles [e.g., 101, 116, 117].

When aiming for multi-mineral segmentation, researchers have used complementary imaging techniques to retrieve quantitative mineral information of ores using CT [115]. Combining CT

with conventional analytical techniques like SEM-EDS has allowed for the correlation of 2D compositional information with 3D CT data. This correlation has then been used to identify minerals and guide the labelling process [93, 103, 115], to calibrate the 2D data with CT data [118] or to train machine learning algorithms with 2D image data [119] throughout the segmentation process. Using this combined approach, Warlo et al. [115] applied watershed segmentation for multi-mineral quantification in complex ores, finding it effective for phases with distinct X-ray attenuation but inaccurate for small or similarly absorbing phases. In response to these constraints, several machine learning-based segmentation techniques have been explored in enhancing mineralogical characterisation using CT [58, 105, 119–122]. Recent advancements in this field have introduced DL-based segmentation [88]. Although initial results are promising, the number of studies is still very limited and the accuracy of these methods require further validation.

1.5 Research gaps

The review revealed several research gaps in the context of ore analysis. In the following, these gaps are further elaborated and shall be addressed throughout this thesis:

1. Limited studies aiming to enhance CT image quality prior to reconstruction:
   While a lot of research has focused on enhancing the mineral differentiation through a) dedicated scanning protocols for high X-ray absorbing ores [30, 100, 105–107], b) combining spectral information [109, 110], or c) using synchrotron CT [34, 108], it appears that no study has been devoted to enhance image quality through the CT acquisition process and also to quantify this improvement. While DECT is successfully used in medical scanning, its effectiveness for contrast enhancement in geomaterials has not yet been explored.

2. Limited studies exploring the utility of DL-based segmentation of complex ores:
   With recent advances in DL-based segmentation for mineral quantification [88], further studies are needed to assess its potential, particularly for segmenting complex ores with similarly X-ray absorbing minerals and for establishing multi-mineral segmentation for modal mineralogical analysis. This includes the need to validate the results to be obtained with conventional mineralogical techniques.

3. Limited studies on CRMs:
   While the majority of researchers focused on the study of gold and PGE-bearing ores [29–32, 85–96], with minor contributions of copper [102, 103], chromite [101], and tungsten [35, 36] ores, studies focusing on examining CRMs bearing ores using CT are still scarce. Consequently, developing appropriate CT protocols for the acquisition and processing of these geomaterials is essential to establish valid and reliable CT data for this class of materials.

   Regarding graphite ore: Research on graphite ores in the context of CT is very limited with one study examining minor graphite-bearing drill cores to distinguish between high and low X-ray attenuating minerals [33] and another exploring the use of synchrotron CT on a graphite-bearing mica schist [34]. Consequently, studies focusing on developing proper CT analysis protocols for graphite ores, enabling their mineralogical characterisation are lacking. Notably, knowledge of CT analysis of low-density ore minerals and their associated gangue minerals is limited, with most CT studies being devoted to high-density ore minerals (e.g., magnetite). This limitation under-

scores the need for developing CT analysis protocols to characterise ores comprising low X-ray absorbing ore minerals properly, such as graphite.

Regarding tungsten ore: Previous studies applying CT to tungsten ores, focused on developing methods to establish tungsten content [35] or to examine tungsten concentrates [36]. However, comprehensive case studies on tungsten ores are lacking, particularly those optimising CT for establishing morphological information and modal mineralogy, crucial aspects for discussions on ore formation and mineral processing.

1.6 Research question, aims and objectives

On the basis of the previous sections, the main research question and the main research aim can be deduced. As the research gaps revealed, it is essential to study CT for its application to graphite and tungsten ore. Dedicated methods must be developed to establish proper CT analysis of these ores, allowing for their comprehensive CT-based analysis. Therefore, the ***main research question*** is as follows:

How can CT be optimised for the characterisation of the critical raw materials graphite and tungsten in ores to obtain reliable qualitative and quantitative mineralogical information?

Optimising CT in this perspective will allow to pursue the ***main research aim***:

To investigate the potential of CT for the mineralogical characterisation of graphite and tungsten ore.

The experimental work of this thesis addresses the main research question through three dedicated studies. Each study is guided by a key objective and reported in a peer-reviewed research article. The experimental work focuses on optimising the key factors of the CT analysis chain including developing effective analysis workflows, generating high-quality CT datasets, and applying advanced image processing strategies, suited to the characteristics of graphite and tungsten (scheelite) ore. This shall ultimately allow assessment of the potential identification of mineralogical and textural properties with CT.

Key objectives

Article 1 - CT of graphite ore: developing an analysis protocol for mineralogical characterisation

Considering complex ores, comprising low-density target minerals such as graphite, are underexplored, the first logical step for optimising CT is to investigate the factors required to generate proper CT data on graphite ores. Consequently, the key objective of study 1 is:

To develop a CT analysis protocol for the mineralogical characerisation of graphite ore.

Article 2 - DECT of graphite ore: enhancing image contrast

Anticipating the heterogeneous attenuation properties of graphite ore, which suggest limited grey value contrast between individual phases present in the ore, methods are needed to optimise image contrast in CT image data of graphite ores. Consequently, the key objective of study 2 is:

To investigate the effectiveness of high-resolution DECT for enhancing image contrast on a graphite ore.

Article 3 - CT of tungsten ore: case study on morphological characterisation and modal mineralogy

It is important to validate the previously developed methods by applying them to different ore types. In addition to investigating the use of CT for graphite ores, this work also aims to optimise CT for tungsten ores. Consequently, the key objective of study 3 is:

To examine the mineral texture, modal mineralogy and WO_3 grade of scheelite ores from Kara Fe-We deposit using CT.

1.7 Methodology and structure

Chapter 1 – General introduction: The first chapter contains the introduction presenting the motivation, background information, research gaps, scope, and significance of this thesis. Fig. 1.2 shows the general structure of this work.

Chapters 2 - 4 – Experimental studies: Chapters 2-4 present the three experimental peer-reviewed studies, addressing the main research aim and question through the key objectives and sub-questions developed for each study. In Chapters 2 and 3, the CRM investigated was graphite ore, with a focus on method development, while in Chapter 4, which presents a case study, the CRM investigated was scheelite ore. The 3D data generated by CT is mainly presented in 2D figures; a video produced in the first study, visualising the 3D information, is also included in the Supplementary material. It should be noted that the research articles presented in the following Chapters have been included with minor adjustments regarding content and formatting, resulting in some, inevitable repetitions of content between the individual chapters of this thesis.

Chapter 2 – CT of graphite ore: developing an analysis protocol for mineralogical characterisation: Chapter 2 explored whether CT provided valuable mineralogical information for the characterisation of flake graphite ore. Given that the limited data on CT analysis of graphite ore, the chapter focused on developing an appropriate CT analysis protocol to generate high-quality CT data, aiming to establish qualitative and quantitative mineralogical information. The results were then cross-validated using conventional mineralogical methods. Additionally, the chapter addressed challenges associated with selecting suitable acquisition parameters for graphite ore. The findings of this study laid the groundwork for the subsequent chapters, informing the optimisation of image contrast (Chapter 3) and contributing to both practical and theoretical knowledge in CT analysis (Chapter 4).

Chapter 3 – DECT of graphite ore: enhancing image contrast: Chapter 3 investigated the effectiveness of dual-energy CT in enhancing image contrast of a graphite ore sample, thereby addressing challenges associated with differentiating phases with similar grey values in single-energy CT scans. The chapter detailed the development of a DECT scanning approach fusing data from single-energy CT scans acquired at low and high X-ray energies prior to reconstruction. To evaluate the significance of the outcomes, a method was developed for quantitatively measuring image contrast between individual phases within the ore, allowing for a robust comparison of image quality between multi-material datasets comprising heterogeneous grey value information.

Chapter 4 – CT of tungsten ore: case study on morphological characterisation and modal mineralogy Chapter 4 showcased the practical application of CT by examining the mineral texture, modal mineralogy, and WO_3 grade of two scheelite ore samples from the

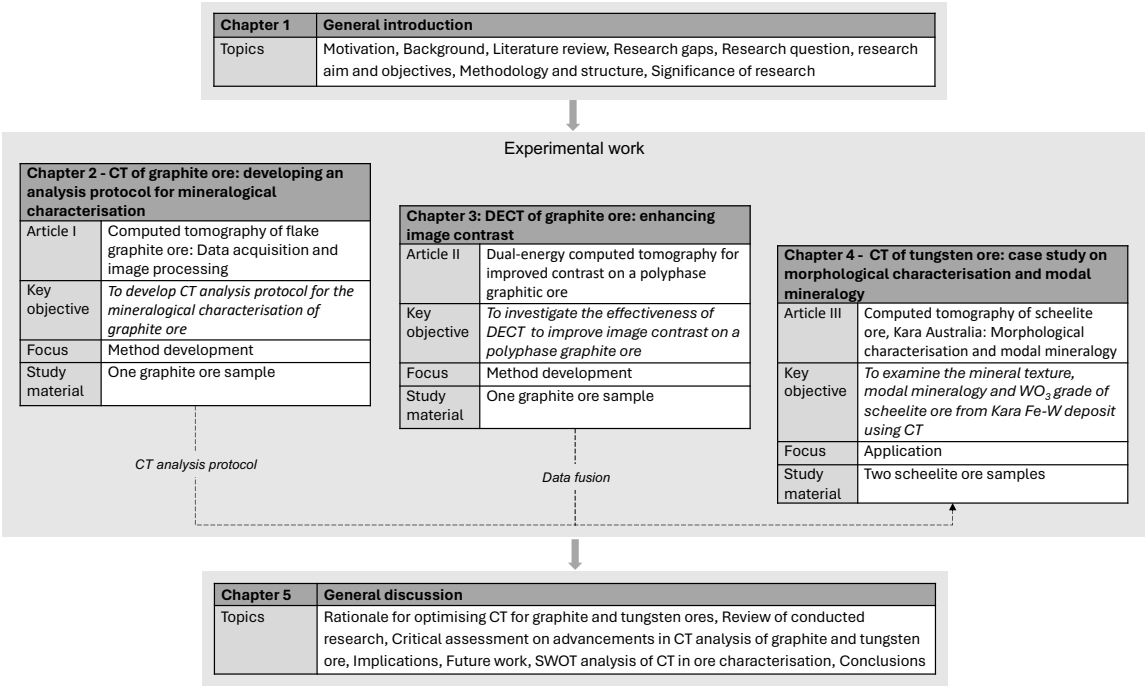

Figure 1.2: Flow sheet of the structure of this cumulative PhD thesis.

Kara Fe-W deposit in Tasmania, Australia. The CT analysis protocol developed in Chapter 2 was adapted and optimised for scheelite ore, including applying data fusion (Chapter 3) for one sample to mitigate acquisition constraints. This approach enabled examining ore textures in 3D, and establishing quantitative information on grain size distribution, scheelite volume, WO_3 grade, and modal mineralogy.

Chapter 5 – General discussion: Chapter 5 presents the general discussion, reviewing the research findings, answering the main research question and reflecting on the main research aim. Moreover, a critical assessment on the advances made in CT analysis of tungsten and graphite ores is conducted. Additionally, this chapter provides implications and recommendations for future work, followed by a SWOT analysis of using CT for ore analysis and concluding remarks.

1.8 Significance

Sustainable and efficient extraction of CRMs requires a comprehensive understanding of the mineralogical characteristics of their host material (ore). Traditional imaging techniques used for mineralogical analysis techniques are limited to 2D and subject to stereological bias when translating into 3D. While CT enables 3D mineralogical analysis, establishing accurate and reliable CT data can be challenging, particularly when applied to complex ores like graphite and tungsten ores. Given the limited knowledge on the application of CT to such ores, this study investigates the potential of CT for their characterisation, presenting the following significant contributions:

- *Enhancing the understanding of ore properties:* By generating high-quality 3D data, this thesis will contribute to improving the understanding of the mineralogical characteristics of graphite and tungsten ores studied.
- *Advancing method development:* By establishing dedicated acquisition and image processing workflows, this research will aid the methodological advancement of CT for the study of

graphite and tungsten ores. The results will support future research and characterisation for these materials.

- *Expanding the knowledge base of CT applications:* This research will ultimately provide valuable insights into the potential and limitations of CT for CRMs like graphite and tungsten ores. These findings will enrich the growing body of knowledge on CT applications in ore characterisation, fostering the ongoing development of CT as an advanced tool in mineralogical analysis.
- *Developing model systems:* As highlighted in Section 1.3, graphite and scheelite exhibit significantly contrasting physical properties, determining their specific X-ray attenuation characteristics. The findings from these studies can inform the development of CT protocols applicable to other CRMs with similar characteristics. For example, the protocols developed can potentially be adapted for low-density minerals like lithium-bearing spodumene and high-density minerals such as rare earth element-bearing fluorocarbonates (e.g., bastnäsite) and monazite. Consequently, this work will extend the application of CT to a broader range of CRMs.

- this page is intentionally left blank -

Chapter 2

CT of graphite ore: developing an analysis protocol for mineralogical characterisation

Key objective:	To develop a CT analyis protocol for the mineralogical characterisation of graphite ore
Focus:	Method development
Study material:	One sample of flake graphite ore

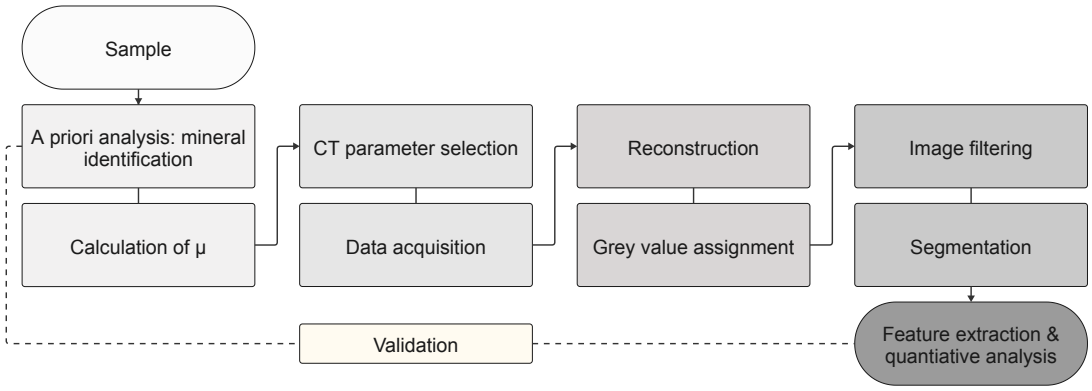

Authors: *Leonard T. Krebbers, Bernd G. Lottermoser, Xinmeng Liu*
Journal: *Minerals*
Accepted: *6 February 2023*
Citation: *L.T. Krebbers, B.G. Lottermoser, X. Liu, Computed tomography of flake graphite ore: data acquisition and image processing, Minerals 13 (2) (2023) 247. doi:10.3390/min13020247.*

2.1 Introduction

Natural graphite is an allotrope of carbon consisting of layers of graphene, i.e., one-atom thick, hexagonal lattice layer of carbon with carbon atoms connected to each other by covalent bonds [123]. The individual graphene layers are held together by van der Waals forces. These weak interplanar interactions endow the mineral graphite with exceptional properties such as refractoriness, high heat and electrical conductivity, greasiness and high thermal resistance [124]. Graphite is applied in a variety of technological applications including lithium-ion batteries (LIB), fuel cells, two-dimensional graphene electronics and fibre optics [124, 125]. Consequently, natural graphite has been recognised as a critical raw material by mega economies such as the United States and the European Union because of its high economic importance and supply risk [5, 126]. Today, China accounts for almost 75% of the global natural graphite production, followed by Mozambique and Brazil. Together, the three countries represent around 90% of the world's production [127]

Natural graphite is found in the Earth's crust in a variety of geological settings and results from the conversion of carbonaceous matter through metamorphic processes into graphite (graphitisation) or by deposition from carbon-bearing fluids [128, 129]. There are various classification schemes, one of which subdivides graphite deposits according to their formation conditions into (1) lump (vein), (2) flake and (3) amorphous (microcrystalline) graphite [128]. In market terms, graphite is classified according to the particle (flake) size (Table 2.1). In contrast to many other mineral resources, the quality of graphite ore is not solely determined by grade, but rather on its mineralogical properties such as grain (flake) size, distribution, shape and purity. These properties will inform market applications and product price [14, 130]. Graphite deposits that contain a high proportion of large graphite flakes tend to have higher purities and carbon content. The flake size distribution is deposit-specific and decisive for the economic viability of a deposit as well as the ultimate use of the concentrates produced [131]. To date, only graphite with high purity and large flake sizes can be used for LIB [132]. Recent developments allow the use of smaller flakes for LIB manufacturing. Regardless, rigorous characterisation of the raw material is key to assessing ore quality and achieving the best possible beneficiation product.

Graphite raw materials are conventionally characterised using X-ray powder diffraction (XRD), differential thermal analysis/thermogravimetry (DTA/TG), inductively coupled plasma mass spectrometry (ICP-MS), scanning electron microscopy coupled with an energy dispersive detector (SEM-EDS), Raman spectroscopy and optical microscopy (OM) as well as SEM-based automated mineralogy systems such as QEMSCAN (quantitative evaluation of minerals by scanning electron microscopy) and MLA (mineral liberation analyser) [e.g., 133–136]. Results of these techniques provide vital information on the presence and properties of graphite ores. In some cases, the acquired information cannot be related to any dimensional geometries of the analysed samples (e.g., XRD). By contrast, OM, SEM-EDS, QEMSCAN and MLA allow for 2D visualisation of graphite ores. However, these techniques are time-consuming, and their sample preparation is destructive and requires careful sectioning of the original sample (e.g., drill hole) to select representative sample material. Moreover, results of the above-mentioned methods must be translated into the third dimension and are therefore subject to stereological bias [20]. For ores of complex mineralogy and microstructure such as graphite ores, where grain size distribution is an important assessment feature, this can be challenging. While graphite ores and their products represent 3D arrays of mineral assemblages, there is a need to acquire information on the 3D distribution of the quality-determining properties (i.e., flake size, intergrowth) of graphite in ores to achieve optimal processing and target use of graphite ores.

Table 2.1: Market terminology of natural graphite and general properties (modified after [14, 137]).

Classification	Size (µm)	Carbon content of concentrates (%)
Amorphous	<75	75-90
Small flake	75-150	90-97
Medium flake	150-180	90-97
Large flake	180-300	90-97
Jumbo	300-500	90-97
Super Jumbo	>500	90-97

A novel tool to display the 3D distribution of mineral phases is X-ray microfocus computed tomography (CT). For example, several scientific studies have demonstrated the use of CT to define the in situ location of gold grains and their distribution within gold ores [31, 32, 90, 93]. Ghorbani et al. [99] successfully used CT for the 3D characterisation of crack and mineral dissemination in sphalerite ore particles. Godel et al. [30]; Godel et al. [85]; Sittner et al. [88] studied the 3D distribution of platin group metals (PGMs) to understand ore-forming processes. Le Roux et al. [35] quantified tungsten ore mineral content and ore grade using CT to assess the quality of the tungsten ore. Similarly, Rozendaal et al. (2017) demonstrated the ability to quantify the final product quality grain size distribution, perform grain shape definition and identify external and internal mineral textures of a Ti-Zr placer deposit [113].

To date, however, the use of CT has not been comprehensively tested to characterise graphite raw materials. This study explores the application of CT for the characterisation of graphite ores. An acquisition protocol was developed to acquire appropriate CT data. Furthermore, an advanced image processing strategy was established that was based on deep learning algorithms to extract quantitative information on key microstructural features of the flake graphite ore in 3D. This study demonstrates that CT imaging of graphite ores requires careful development of image protocols and processing strategies, which can then produce new insights into graphite ore properties.

2.2 Materials and methods

2.2.1 Materials, preparation and conventional techniques

A flake graphite ore sample was provided by the German-based company NGS Trading & Consulting GmbH (Leinburg, Germany) from the Yanxin graphite mine (Shangdong province, China). XRD was carried out on a ~2.5 g aliquot of the sample, which was ground in 100% ethanol in a McCrone micronising mill using synthetic agate pellets for 5 min. Micronised aliquots were air-dried and subsequently analysed on a Rigaku Ultima IV powder X-ray diffractometer (Department of Earth and Atmospheric Sciences, University of Alberta, Edmonton, Canada). The Rigaku Ultima IV XRD is equipped with a Co source that was operated at 38 kV and 38 mA. XRD patterns were collected from 5 to 80° 2θ using a step size of 0.02° 2θ at a rate of 1.2° 2θ/minute. Qualitative phase identification was performed using the JADE (Rigaku, Tokyo, Japan) and EVA (Bruker, Billerica, MA, USA) software packages. Mineral phases were identified with reference to the International Center for Diffraction Data Powder Diffraction File 4+ database (ICDD PDF4+). For petrographic analysis, a thin section and cylindrical-shaped polished block were prepared

by MK Factory (Stahnsdorf, Germany). Both samples were examined using a LEICA DM 2700P polarization microscope (Institute of Mineral Resource Engineering, RWTH Aachen University, Aachen, Germany). Microphotographs were taken with a LEICA FLEXCAM C1 camera to establish an image mosaic of the polished section using the LEICA LAS software. Scanning electron microscopy combined with an electron dispersive spectrometer (SEM-EDS) was used to provide further insights on the mineralogy and microstructure of the graphite ore specimen, using a FEI 650F scanning electron microscope equipped with two Bruker XFlash 5030 detectors (Institute of Mineralogy and Economic Geology, RWTH Aachen University, Aachen, Germany) (15 kV, 10 nA).

2.2.2 Computed tomography

In this study, a ProCon Alpha micro-CT system was used, which is equipped with a five-axes-manipulation system between an XWT-240-TCHE plus X-ray tube with a maximum voltage of 240 kV and an XRD 1611 AP3 detector system with 4064 x 4064 pixels (100 mm^2) (Institute of Mineral Resources Engineering, RWTH Aachen University, Aachen, Germany). For the scanning procedure, a cylindrically shaped, polished graphite sample (14 mm diameter, 11.5 mm thickness) was investigated. CT measures the attenuation of an X-ray that passes through sample object. The X-ray attenuation depends on the material density and atomic number as well as the X-ray energy applied [84, 138]. A CT measurement is the collection of 2D sample projections (radiographs), which are taken as the sample rotates 360° around the vertical axis between the X-ray tube and the detector. The detector collects the number and intensity of transmitted X-rays of each projection and thus provides X-ray attenuation information. Based on this information, an X-ray attenuation coefficient is calculated for each pixel of the acquired sample projection. This coefficient is displayed as a distinct grey-scale value in the projection image [26]. The collection of radiographs is then stacked to create a 3D volume, comprising a cubical matrix of grey-scale voxels (3D pixels). Thus, CT allows for the 3D analysis of multicomponent materials such as ore and rocks, providing nondestructive internal microstructural information on mineral volume, mineral size, mineral distribution, association, orientation and porosity [21, 139–141].

Data acquisition

Scan parameters were determined in the course of several test measurements and iteratively optimised to obtain low-noise, high-contrast images with as few artefacts as possible in the shortest possible time. Attenuation curves were calculated based on the samples' mineralogy, as determined by XRD, OM and SEM-EDS (Fig. 2.1). Attenuation curves were calculated by multiplying the mass coefficient by mass density. The nature of X-ray attenuation is predominantly a function of photoelectric absorption and Compton scattering. Photoelectric absorption occurs when the total energy of an incoming X-ray photon is transferred to an inner electron, causing the electron to be ejected. The probability of this effect is heavily dependent on the atomic number (Z) of the absorbing material and the X-ray energy; photoelectric absorption is proportional to Z^{4-5} [42, 104]. In Compton scattering, the probability of X-ray absorption is proportional to only Z, as the incoming X-ray photon interacts with a free or outer electron, ejecting the electron. Hence, the probability of this effect is more dependent on the electron density of the material [43]. The photoelectric effect prevails in low energies (approximately 50 - 100 keV), whereas Compton scattering dominates in energies >5 MeV [82]. Thus, to increase the attenuation contrast between graphite and similar attenuating gangue phases as well as the epoxy resin, the application of lower voltages is recommended. However, using lower voltages results in decreasing penetration capability and

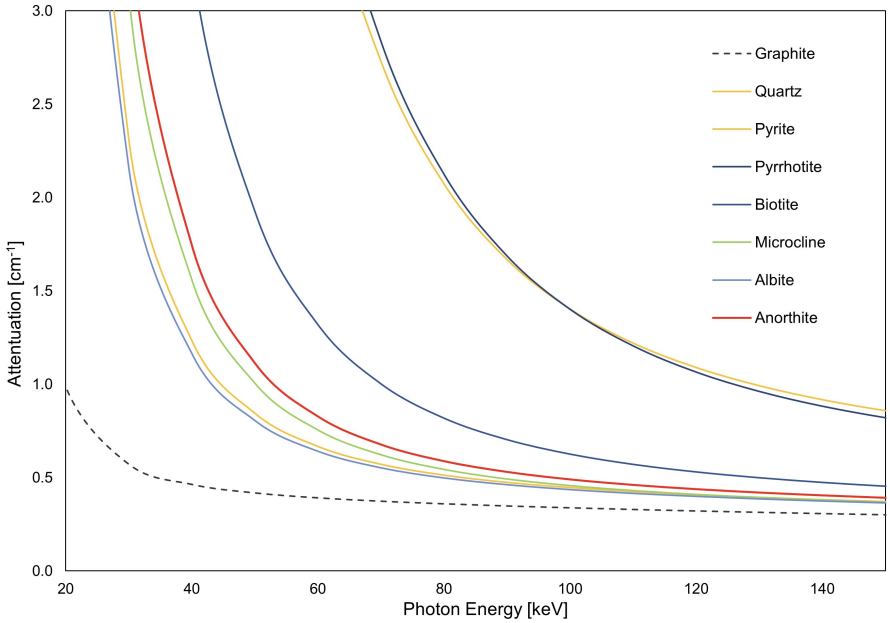

Figure 2.1: Linear attenuation coefficients as a function of X-ray energy for the major minerals occurring in the scanned sample. The values displayed in the graph calculated based on end member compositions, and densities and were calculated using the XCOM Photon Cross-Sections Database NIST [104].

the production of more artefacts, especially when high absorbing phases are present. To achieve a good signal-to-noise ratio, a longer exposure time is required in this case, as this is proportional to the number of photons recorded per projection. Thus, given that the sample contains highly absorbing phases, voltage and exposure time were adjusted accordingly to achieve minimum beam hardening on one hand and maximum contrast on the other. To further reduce noise, the number of averages per projection was adjusted accordingly. Lastly, to maintain optimal focal spot size, which determines the X-ray flux and resolution capability of the XCT system, the applied power of the X-ray beam was set slightly higher than the scan resolution. The final scanning conditions are summarised in (Table 2.2). Reconstruction of the scanned sample was performed with the

Table 2.2: Scanning conditions of the scanned flake graphite ore sample.

Acquisition parameters	
Voltage (kV)	100
Current (µA)	110
Exposure time (s)	1.35
No. of averages ()	4
Binning (-)	1 x 1
No. of projections ()	2500
Scanning time (h:m)	9:05

VGStudio Max 3.5. software [49] based on filtered back-projection (FBP) and a beam hardening correction to address cupping artefacts and streak artefacts generated due to the polychromatic nature of the beam.

Image filtering

When the attenuation coefficient values are converted into CT numbers, a certain amount of noise is always present in the CT images due to random variations. Therefore, digital image filters were applied prior to segmentation to enhance the quality of the scan by reducing noise and increasing grey value contrast. The actual operation is applied on a 2D CT slice image. The software used, ORS Dragonfly (Version 2022.1) [61], offers a broad range of filtering operations, which can be applied iteratively. A three-filter combination produced the best results (Fig. 2.2). First, a median filter was applied to denoise the image. This was followed by the unsharp filter, using an unsharp factor of 3 to increase the edge contrast of grains. Since the unsharp filter produces noise, the median filter was applied again to denoise the image.

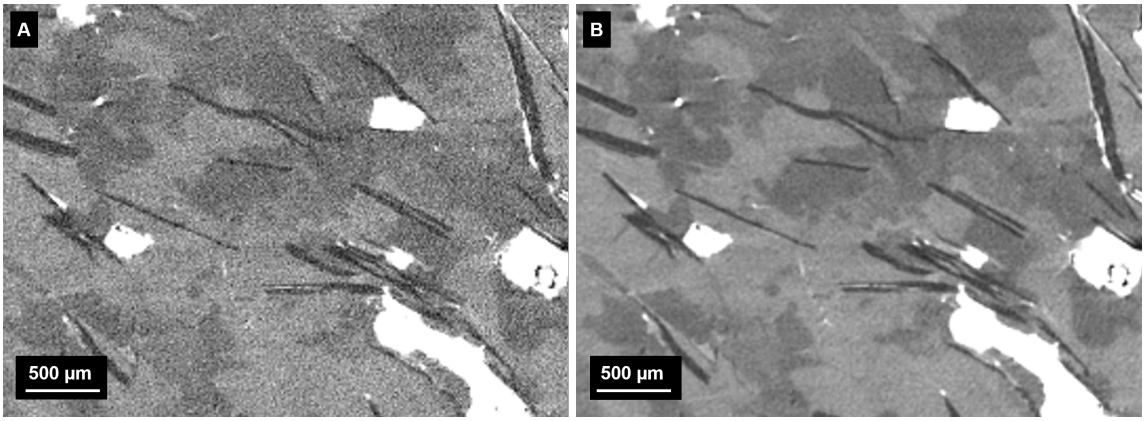

Figure 2.2: CT volume slice **A**) before and **B**) after image filtering. Phases are represented by grey values, ranging from darkest to lightest: graphite; combined quartz, albite and clay minerals; combined microcline, biotite and clinochlore; and combined pyrite and pyrrhotite.

Segmentation

Image processing was carried out using ORS Dragonfly. The software possesses different machine learning and deep learning algorithms that can be used for segmenting different phases simultaneously. Machine learning (ML) refers to a class of model-based computational techniques for processing data [142]. Deep learning (DL) is a subset of ML, featuring many interconnected processors (neurons) that work in parallel. These processors are predominately built on a convolutional neural network (CNN) architecture, which is particularly efficient for image processing [60]. To achieve accurate segmentation, the network must be trained to identify structures and learn how to make predictions (inference stage) for subsequent calculations [60]. Therefore, single or multiple regions of interest on different 2D image slices are created and used to manually select groups of voxels which belong to different segmentation classes. These slices are considered ground truth data, on which basis the algorithm is trained and validated (supervised classification). Consequently, the network allows for automatic segmentation of the entire data set.

The segmentation procedure was performed on a digitally cut cylindrical subvolume (10.53 mm diameter, 8.21 mm thickness) so that (a) the epoxy mount, in which the section was embedded,

was excluded as well as the cone-beam effect (depth-related greyscale gradients); (b) operation time was accelerated by reducing the data size; (c) each horizontal slice was of equal area; and (d) the topmost slice had the same surface as that of the polished section to enable subsequent comparison with mineralogical and petrographic OM and SEM-EDS data. Regarding the model architecture, Random Forest [143], U-Net [144] and sensor3D [145] models were tested and trained. The mineralogical and petrographic information obtained using XRD, SEM-EDS and OM was essential to interpret the CT radiographs and to identify the phases according to their grey-scale values. Three classes were determined, comprising graphite, high X-ray attenuating phases (i.e., pyrite, pyrrhotite, rutile, zircon) and the remaining gangue minerals. These were labelled manually on a randomly selected area (frame) of a 2D slice to establish a first training data set. The model was then tested on a new slice, and wrongly classified voxels were corrected and attributed to the training data. The accuracy of a model and thus the segmentation result depends on the network parameters, which need to be selected properly in accordance with the properties of the data information to be segmented. After several trial runs with different combinations of parameters and training slices, the sensor3D network was identified to perform best, and therefore, it was used for subsequent segmentation operations until no further improvement could be achieved (Fig. 2.3). The final model architecture is summarised in Table 2.3.

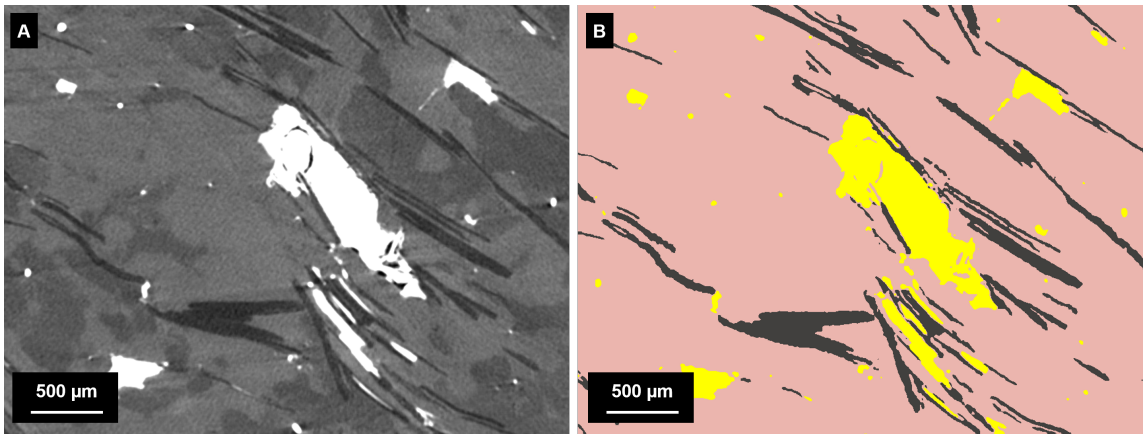

Figure 2.3: CT volume slice of the scanned specimen **A**) before, and **B**) after segmentation. The colours represent the segmented classes: graphite (dark grey), high X-ray absorbing phases (pyrrhotite, pyrite and accessories of zircon and rutile) (yellow) and the silicate matrix (pink).

Table 2.3: Model architecture of the DL network chosen. All listed parameters are dimensionless.

Model parameter	**Value**	**Explanation**
Patch size	64	Size of the areas (patches) into which the input image is divided
Batch size	32	Input layer, defines number of patches being evaluated
Epochs per frame	20	One training operation
Stride-to-input ratio	0.1	Defines the position of the neighbouring patches
Dice score	0.9971	Measurement of the accuracy of a deep learning model based on the similarity of prediction and ground truth data

In total, 6 frames were created, and the training time was 216 min. A total of 80% of the labelled data were selected by default for training the model and the remaining 20% for validating the model. Furthermore, the sensor3D model was trained for 20 epochs with early stopping enabled to avoid overfitting, whereby the model stopped automatically if the validation loss increased. The model applied reached a dice coefficient of 0.9971, which is an indicator of the model's accuracy (Glossary p. 107ff).

2.3 Results

2.3.1 Mineralogy and 2D petrography

The flake graphite ore samples consist of a quartz-dominated matrix with plagioclase (anorthite and albite), microcline, biotite, pyrite and pyrrhotite as well as small quantities of rutile, clinochlore and clay minerals. Zircon is present as an accessory. Foliation structure is present primarily due to graphite and biotite ± clinochlore arrangement. Graphite occurs as deformed euhedral–subhedral, platy-shaped crystals, varying in grain size from ~15 to 1900 µm, with most of the flakes >100 µm. The graphite particles are mostly disseminated in the matrix with some large particles attached to each other. Some flakes are deformed and broken apart along the cleavage plains. The grain boundaries of the flakes are of straight or polygonal structure. Quantities of rutile as well as pyrrhotite and pyrite are present as subhedral to euhedral crystals in the matrix. Both pyrite and pyrrhotite are occasionally attached to graphite flakes, where they may occur as elongated crystals along basal cleavage planes of graphite Fig. 2.4. Biotite is occasionally moderately replaced by clinochlore and mostly associated with graphite. Clay minerals are present along cracks, cleavages of feldspar and grain boundaries. Given the high quartz content, secondary minerals and foliation texture, the ore can be considered an altered graphite gneiss.

2.3.2 Computed tomography

Fig. 2.5 shows a CT volume slice from the scanned flake graphite ore sample. The assignment of grey values to their corresponding phases was based on the XRD, SEM-EDS and OM examinations. Graphite appears dark grey and can be recognised by its typical flaky shape. The phases with the brightest grey values are pyrite and pyrrhotite. In addition, two grey value ranges can be identified: (1) combined quartz, albite and clay minerals, as well as (2) combined biotite, clinochlore, anorthite and microcline. The differentiation between the individual minerals within the respective grey value ranges is not possible, as their grey values are too similar.

For the quantitative analysis of the CT data, the volume, aspect ratio and voxel count were calculated from the segmented classes. Based on these parameters, the graphite volume was refined so that particles wrongly labelled as graphite could be removed from the segmented data. To ensure that realistic grain shapes could be imaged, only particles >4.64 × 4.64 × 4.64 µm (100 voxels) were considered for the analysis. A total of 1877 graphite particles were identified. The segmented volume comprises 533.99 mm^3 and the graphite volume 19.77 mm^3. This corresponds to a volumetric proportion of 3.7% graphite (Table 2.4).

Fig. 2.6 shows the individual graphite particles (Fig. 2.6A) comprising the sample as well as their volumetric distribution (Fig. 2.6B) in 3D. Graphite flakes are aligned and occur mostly disseminated in the ore matrix. The flakes exhibit a subhedral to euhedral shape and vary in grain size. A few, and particularly larger, flakes are subparallel to parallel attached together.

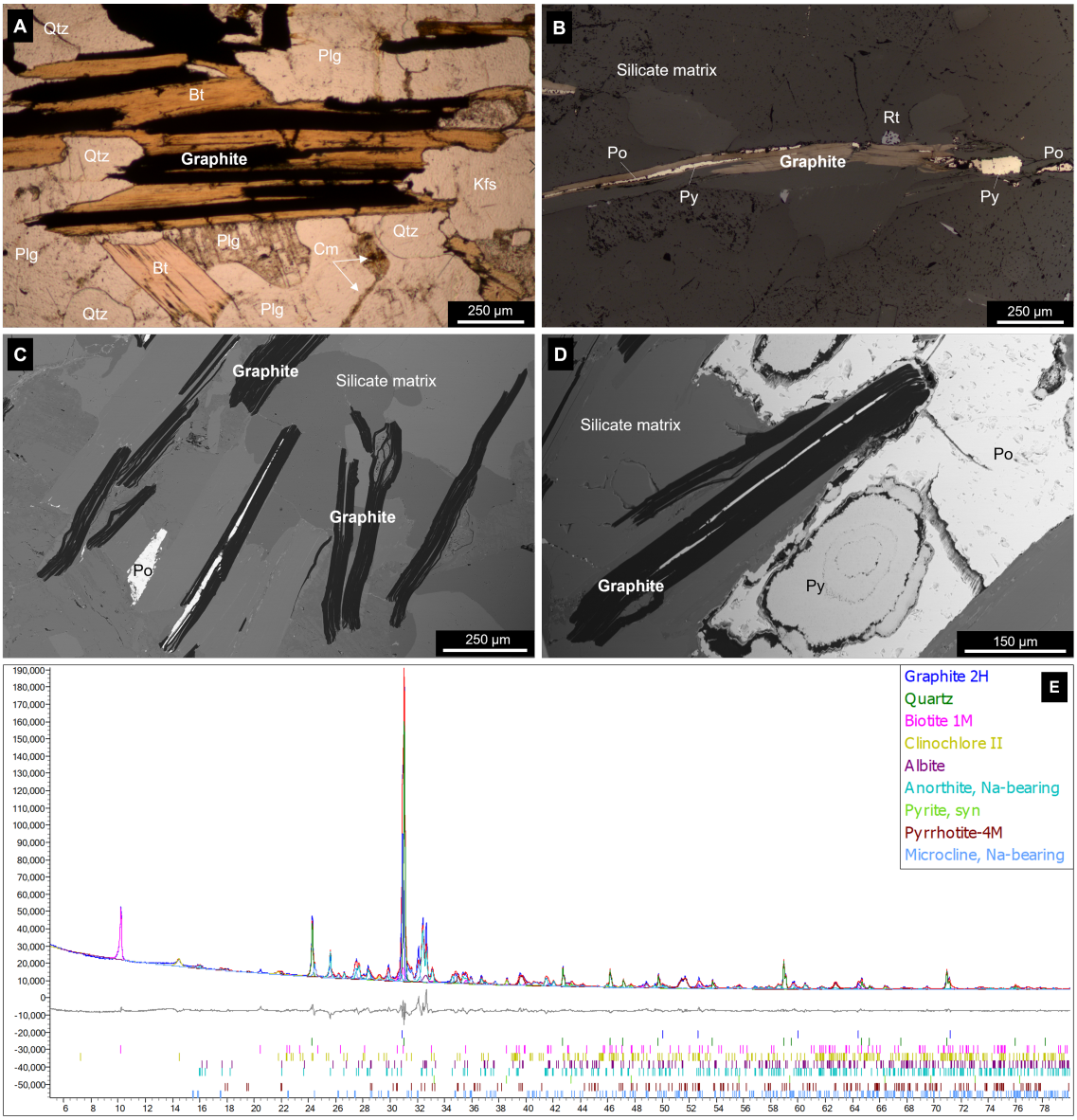

Figure 2.4: **A**, and **B**) OM, **C**, and **D**) SEM images as well as (**E**) XRD patterns of the flake graphite ore sample. **A**) Parallel aligned graphite flakes intergrown with biotite. Graphite flakes are embedded in a silicate matrix comprising quartz, plagioclase (anorthite and albite), biotite and alkali feldspar (microcline). Secondary clay minerals occasionally replace plagioclase and appear along grain boundaries (transmitted light, PPL). **B**) Disseminated super jumbo flake with intergrowth of pyrite and pyrrhotite along basal cleavage planes embedded in silicate matrix. Pyrite, pyrrhotite and rutile are also present as subhedral crystals (reflected light, PPL). **C**) Disseminated parallel to subparallel oriented graphite flakes, partly deformed and broken apart along basal cleavage planes. **D**) Graphite flake intergrown with a subhedral crystal of pyrrhotite. Note the colloform nodule of pyrite in the pyrrhotite grain. Abbreviations: Po = pyrrhotite, Py = pyrite, Qtz = quartz, Bt = biotite, Kfs = alkali feldspar, Plg = plagioclase, Rt = rutile, Cm = clay minerals, PPL = plane-polarised light.

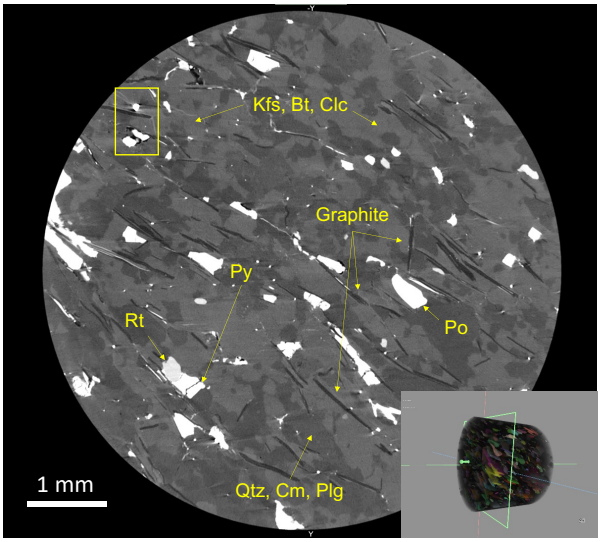

Figure 2.5: CT volume slice of the cylindrical subvolume of the scanned graphite sample. Note the imaging artefacts in the yellow framed box (bright streaks above a graphite flake and dark areas between and around two Po crystals) due to the highly X-ray absorbing iron phases present in the sample. Abbreviations: Qtz = quartz, Bt = biotite, Kfs = alkali feldspar, Plg = plagioclase, Clc = clinochlore, Cm = clay minerals, Po = pyrrhotite, Py = pyrite.

Table 2.4: Segmentation and analysis result of the sample.

Properties of the subvolume	
Length	8
Diameter	10.53 mm
Volume cylinder	533.99 mm³
Volume-% graphite	19.77 mm³
Number of graphite particles	1877

To assess the quality of the sample based on the grain size distribution, the equivalent spherical diameter was calculated using the volume of each particle (Eq. (2.1)):

$$ESD = \sqrt[3]{\frac{6 \cdot volume}{\pi}} \tag{2.1}$$

Fig. 2.7A shows the cumulative in situ particle size distribution of graphite as determined by CT. In terms of particle numbers, small flakes represent the largest proportion of all particles, followed by amorphous and large flake particles (Fig. 2.7B). In relation to the volume of all graphite particles, super jumbo flakes account for the highest proportion of all classes (Fig. 2.7C). Properties of each class are summarised in Table 2.5. The volumetric distribution of the classes is further illustrated in Fig. 2.8. Highlighting the individual graphite classes (Fig. 2.8B-E) shows that the super jumbo and jumbo fractions are occasionally parallel to subparallel attached to each other, forming a clustered arrangement. The other classes are predominantly disseminated throughout the ore matrix, suggesting variable formation conditions.

Since graphite deposits can be very heterogeneous in terms of flake size and graphite content distribution, it is important to measure a large and representative sample volume. Fig. 2.9 illustrates

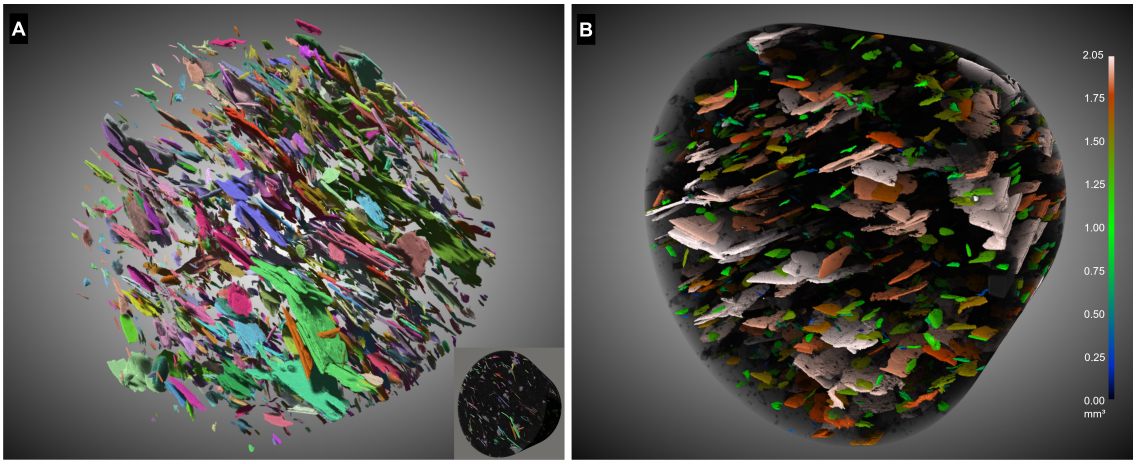

Figure 2.6: Three-dimensional CT images of the cylindrical subvolume after segmentation: **A**) colour-coded graphite particles, and **B**) volumetric distribution of the graphite flakes. The gangue minerals comprising the ore matrix are semi-transparent. The cylinder has a diameter of 10.53 mm and a thickness of 8.21 mm.

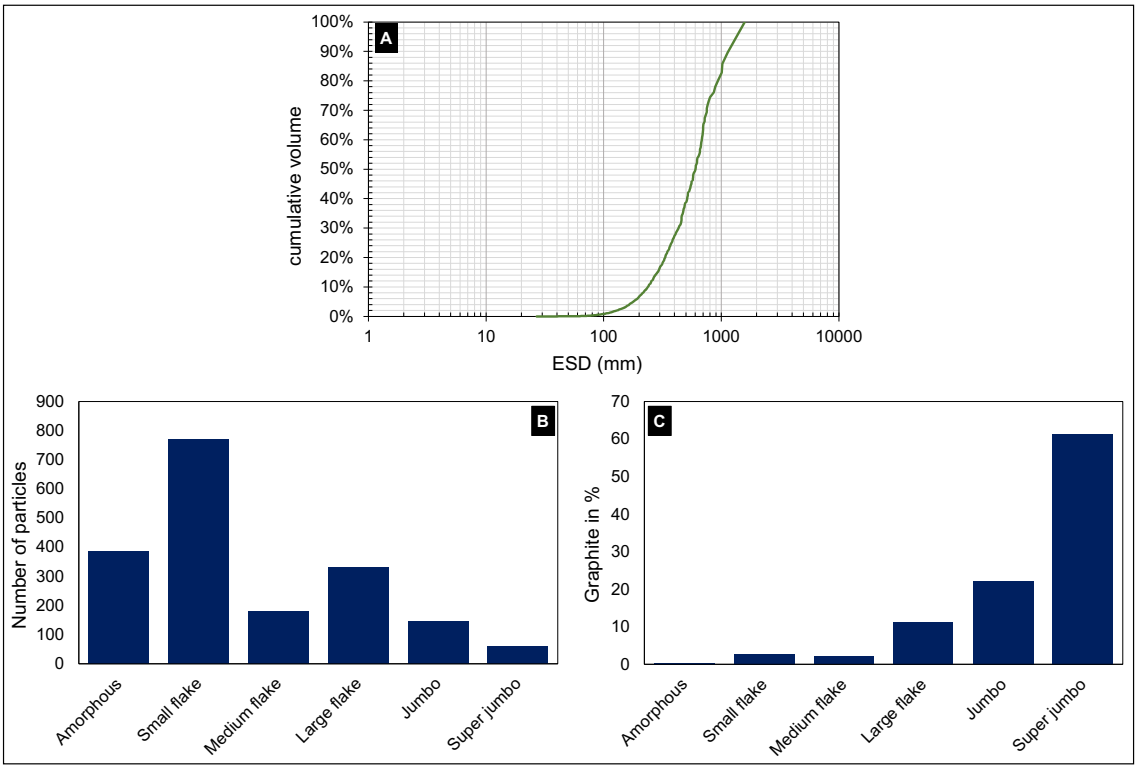

Figure 2.7: Distribution of graphite classes according to CT measurements. **A**) Cumulative particle analysis, **B**) number of particles corresponding to each class, and **C**) volumetric proportion of each class in the sample. While the majority of flakes fall into categories smaller than jumbo and super jumbo, the latter two classes account for 83.6% of the total graphite volume.

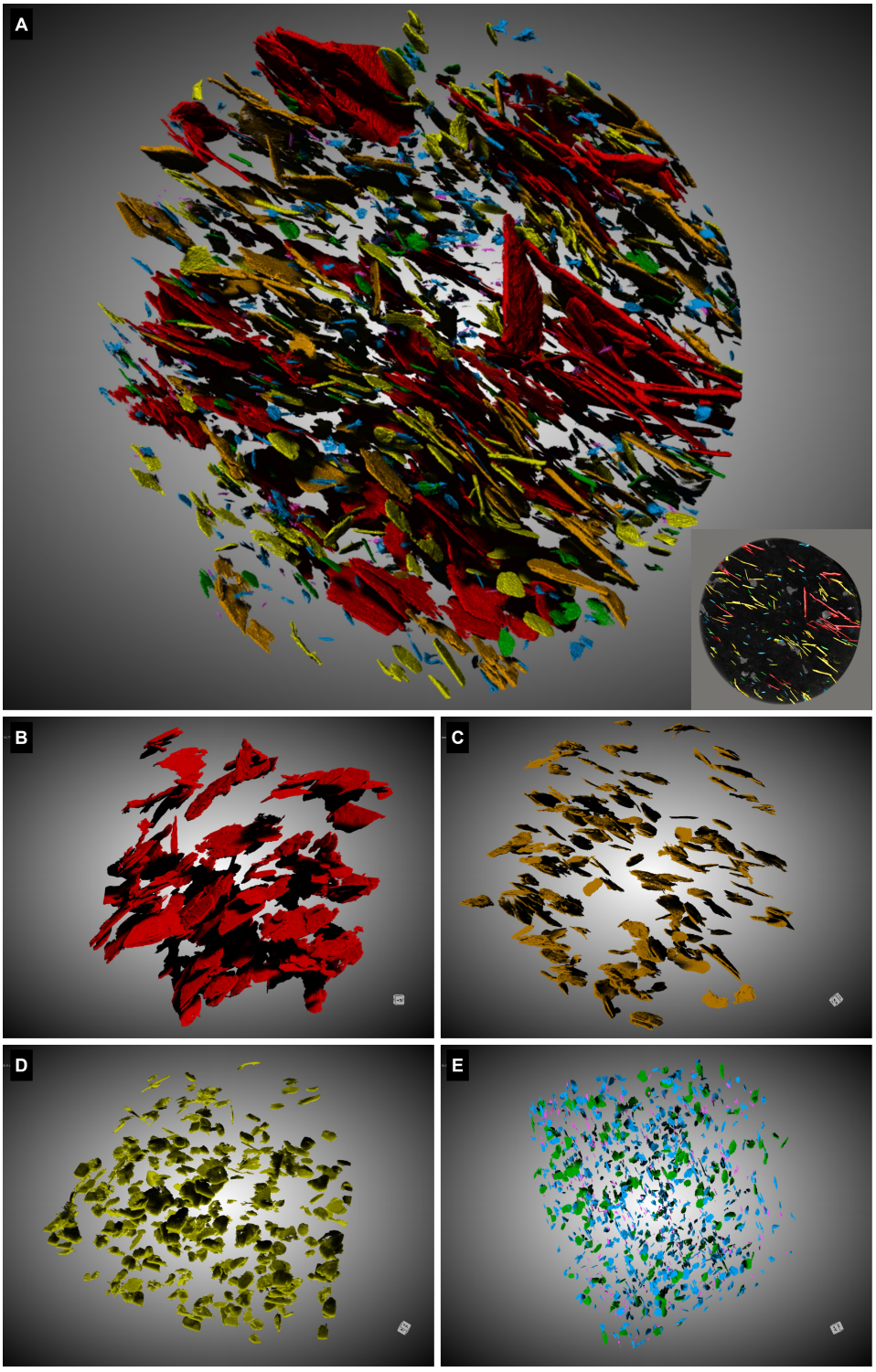

Figure 2.8: Three-dimensional CT images of the segmented subvolume. **A**) Volumetric distribution of the graphite flakes in terms of market-related classes comprising super jumbo size (red), jumbo (orange), large flake (yellow), medium flake (green), small flake (blue) and amorphous (violet). The gangue matrix is set to be fully transparent. A corresponding video is provided in Supplementary Materials. **B**-**E**) individual classes highlighted: **B**) super jumbo size flakes, **C**) jumbo flake graphite, **D**) large flake graphite, and **E**) combined medium flake (green), small flake (blue) and amorphous graphite (violet).

Table 2.5: Properties of the graphite classes determined.

	Amorphous	Small flake	Medium flake	Large flake	Jumbo	Super jumbo
Particles (n)	387	770	180	333	146	61
Particles (%)	20.62	41.02	9.59	17.74	7.78	3.25
Volume (mm²)	0.05	0.55	0.42	2.23	4.4	12.13
Volume (%)	0.23	2.78	2.11	11.28	22.23	61.36

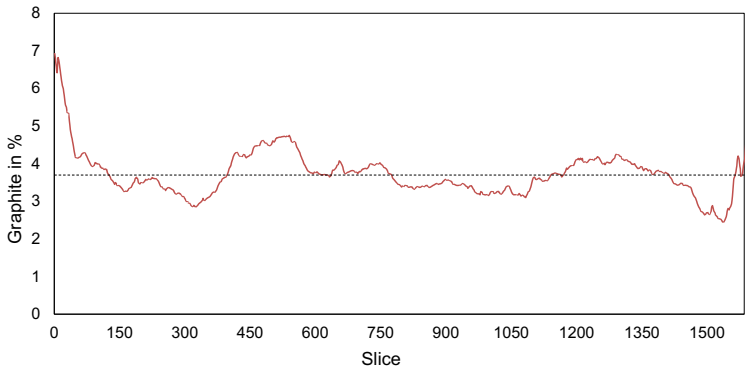

Figure 2.9: Graphite content per slice of the cylindrical subvolume. The dashed horizontal line represents the average graphite concentration of 3.7%.

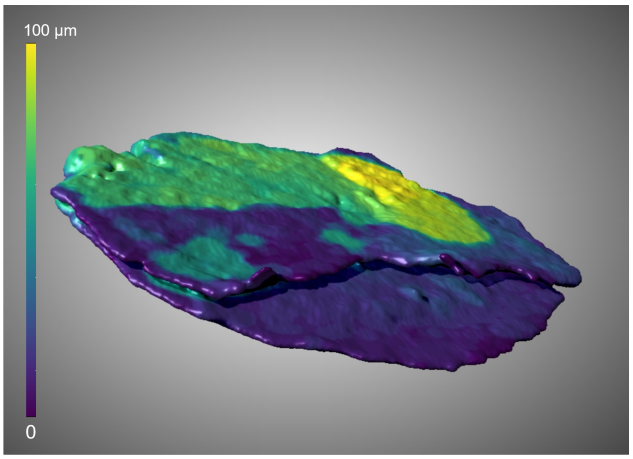

Figure 2.10: Jumbo flake after thickness measurement. The ESD of the flake is 421 µm.

the distribution of graphite concentration from top to bottom in the cylindrical subvolume. The graphite concentration for each slice was measured by subtracting the segmented graphite area per slice from the area of the cylinder. In total, 1600 slices were measured, with a thickness of 5.3 µm per slice. The graphite concentration varies significantly throughout the volume, from 2.46 to 6.97%. Particularly in the upper range of the subsample (slice 0 to 60), the graphite concentration is higher than in the rest of the sample, where the concentration varies from 2.46 to 4.66%.

In addition to particle size distribution and graphite content, textural properties such as flake thickness or impurities also play an important role in the evaluation of a graphite ore. Fig. 2.10 shows the analytical result of a single particle, exemplified by grain thickness. A jumbo flake

with an ESD of 421 µm and a volume of 0.04 mm^3 was extracted from the segmented graphite volume, and for the thickness measurement, the particle volume was extracted to a surface mesh. The differences in the colour markings indicate the differences in thickness along the flake. The average thickness is 56 µm. Further textural properties are listed in Table 2.6. The minimum Feret diameter exceeds the ESD due to the large planar area and small thickness of the flake. Fig. 2.11 features a subhedral graphite flake associated with an iron sulfide grain. In contrast to the 2D image, the 3D image exhibits that the flake is not only attached to the iron sulfide but also intergrown with it.

Table 2.6: Selected textural properties of an individual graphite flake.

Flake properties	
Volume	0.04 mm^3
ESD	421 µm
Thickness (mean)	56 µm
Feret diameter (max.)	1196 µm
Feret diameter (min.)	497 µm
Surface area	2.3 mm^2

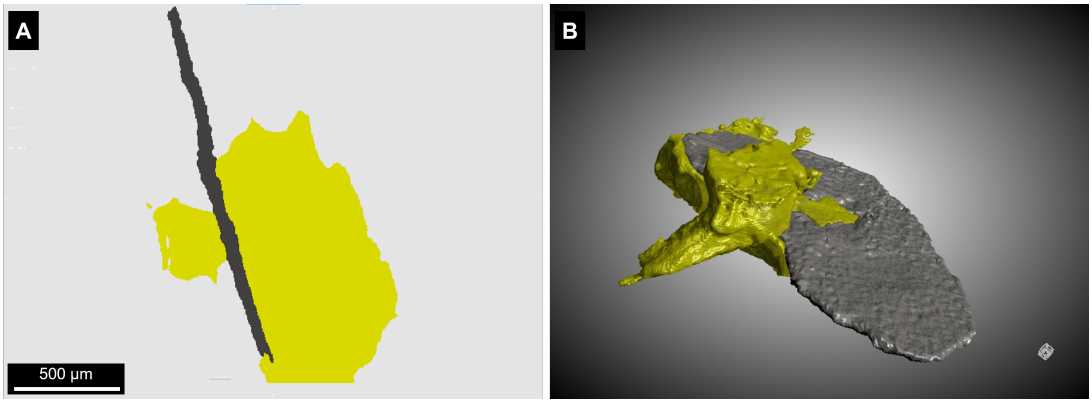

Figure 2.11: Jumbo-sized flake associated with an iron sulfide mineral in **A**) 2D, and 3D **B**). **A**) The CT volume slice shows that the graphite flake is attached to the sulfide mineral. By contrast, **B**) the rendered 3D image reveals that the sulfide mineral is intergrown with the graphite flake. The longest axis of the flake is 1690 µm.

2.3.3 Comparison of 2D petrographic data with 3D CT data

To evaluate the validity of the CT results, a modal mineralogy analysis obtained from optical microscopy analyses was compared with the topmost slice of the CT sample volume (Fig. 2.12). This slice was not part of the segmented cylinder due to abundant imaging artefacts. The topmost slice was trained using the same DL strategies as described above. A set of microphotographs was stitched together to reveal the total surface of the polished section. The stitched image was processed using ORS Dragonfly, applying a global threshold operation. Thereby, the graphite content was measured by subtracting the area of segmented flakes from the total area (86.92 mm^2). According to the OM analysis, the graphite content is 3.3%. The graphite content of the topmost

CT volume slice is 2.99%.

Details of graphite analyses as performed by OM and CT are given in Table 2.7 and Table 2.8. A total amount of 169 graphite flakes were identified using OM (Table 2.7), whereas 156 flakes were identified in the topmost slice using CT imaging (Table 2.8). In particular, more amorphous and small flake grains were found with OM compared to CT. On the other hand, more jumbo flakes were identified in the topmost slice by CT. Overall, the relative proportion of graphite in each class is similar for both OM and CT, with the exception of the jumbo and amorphous classes.

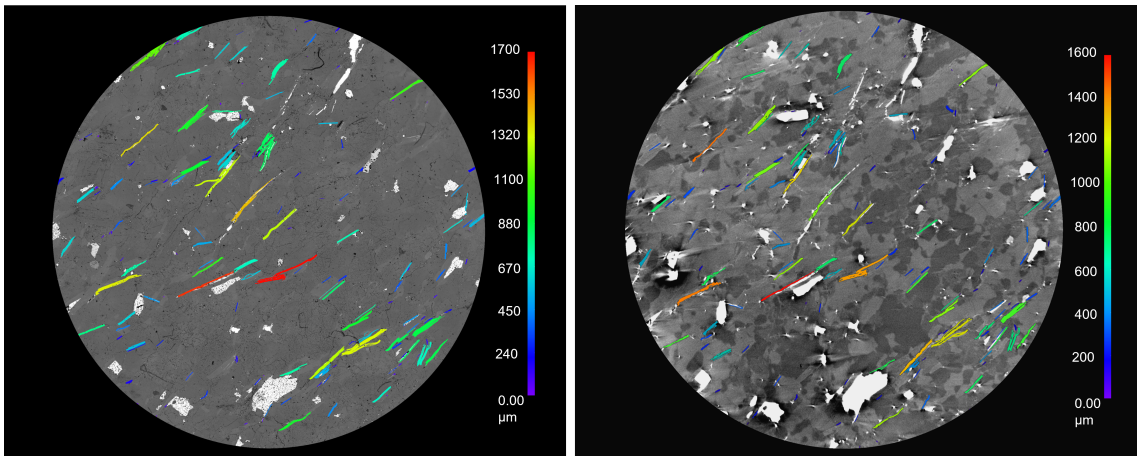

Figure 2.12: Segmentation results **A**) of the stitched OM image, **B**) and the CT volume topmost slice. The rainbow-coloured scale shows the distribution of the longest axis of the individual flakes.

Table 2.7: Physical properties of graphite as determined by OM in a polished section.

	Amorphous	**Small flake**	**Medium flake**	**Large flake**	**Jumbo**	**Super jumbo**	**Total**
Particles (n)	26	20	11	31	25	56	169
Particles (%)	15.38	11.83	6.51	18.34	14.79	33.14	100
Area (mm²)	0.02	0.04	0.04	0.09	0.24	2.44	2.87
Area (%)	0.63	1.44	1.27	3.07	8.50	85.09	100

Table 2.8: Physical properties of graphite as determined by CT in the topmost slice after segmentation.

	Amorphous	**Small flake**	**Medium flake**	**Large flake**	**Jumbo**	**Super jumbo**	**Total**
Particles (n)	22	20	10	20	35	49	156
Particles (%)	14.10	12.82	6.41	12.82	22.44	31.41	100
Area (mm²)	0.02	0.06	0.05	0.15	0.44	1.87	2.6
Area (%)	0.77	2.43	1.78	5.96	16.90	72.16	100

2.4 Discussion

2.4.1 Graphite characterisation

In recent years, an increasing number of scientific studies have recognised the utility of CT for ore characterisation [30–32, 35, 85, 88, 90, 93, 99]. Despite this, the application of CT to characterise graphite raw materials is limited, with prior studies having only provided rudimentary descriptions of graphite through the use of CT. Ren et al. [33] examined drill cores of graphite ore using CT to distinguish minerals with high and low X-ray attenuation, while Fatima et al. [34] analysed the spatial distribution of various ore minerals, including graphite, with CT.

Traditionally, information on graphite ore mineral properties is obtained by XRD, sieve analysis, SEM-EDS or OM examination, [e.g., 14, 135, 146]. These methods provide liberation sizes with accuracies of <120–150 µm [147]. SEM-based automated mineralogy has been recently introduced to establish more precise liberation information [135]. Furthermore, the method provides quantitative information on impurities, grain size distribution and modal mineralogy. MLA thereby extracts information on modal mineralogy on 2D surfaces and mineral associations, which are based on linear contacts and phases exposed at the samples' section surface. For ores with a heterogeneous grain size distribution, this may lead to erroneous information (Fig. 2.9). Moreover, graphite is a very soft mineral and may be affected by mechanical abrasion during sample preparation [135]. This can result in misinterpretations of key textural features. CT, in contrast, as demonstrated in this study, can assess a more representative volume and modal mineralogy nondestructively without stereological bias.

Information on graphite impurities is vital. During graphite ore genesis, other minerals may be deposited between graphite layers, stacks or clusters. Such impurities are attached to flake surfaces or are trapped between flakes (intercalated) [148]. Impurities adhering to the surface can be detached from the flake surface by attrition, without significantly influencing flake size. Those impurities between the layers can only be removed by additional thermal or chemical processes, and such ore treatment methods are costly. Characterising impurities appropriately is therefore crucial to effectively remove this material. Such information on impurities (Fig. 2.11), as provided by 3D CT imaging, allows the appropriate design of flow sheets for the beneficiation of graphite ores.

While OM exhibits better resolutions and information on the gangue mineralogy, it does not present information about the real spatial distribution and volume fraction of graphite within ore samples. CT provides exceptional 3D microstructural data of graphite ore and a more representative characterisation of the quality demanding properties of graphite particles such as in situ grain size, grain size distribution, shape and impurities. In addition, the CT method enables precise measurement of individual flake thickness (as shown in Fig. 2.10 and Table 2.6), which is important for predicting flake breakage during liberation. Thin flakes are more prone to breaking during comminution, making it more difficult to maximize their size. Knowledge on particle thickness therefore aids in selecting the appropriate comminution technique (crushing, grinding, milling). Lastly, it is also possible to generate 3D information on individual grains and their impurities (Fig. 2.11).

2.4.2 Data acquistion

In order to acquire valid CT images and data on geological materials, the mineralogy of the samples needs to be known. Thus, CT cannot be used as a stand-alone technique. Mineralogical methods such as XRD and OM are required to acquire and interpret CT data. Moreover, CT operation requires an experienced operator to achieve appropriate results, particularly for the resolution of minerals with similar attenuation coefficients. The contrast of the grey-scale image in the CT depends on different factors such as X-ray energy applied, as well as the atomic number and density of the phases comprising the sample measured [26]. The choice of the optimal beam intensity to resolve all minerals is infinite. As the investigated ore is rich in heavy minerals such as pyrite and pyrrhotite, it would have required high beam intensities for adequate X-ray penetration to prevent artefacts. This, however, decreases the X-ray absorption capacity of the lower absorbing minerals such as graphite, and silicates, because the attenuation using X-ray energies >100 kV is more sensitive to the mineral's density [43]. Choosing lower X-ray energies would have increased the attenuation differences between lower absorbing fraction (Fig. 2.1) as it is more sensitive to the atomic number [82], but it would have also increased beam hardening, particularly due to the presence of the iron sulfides. A possible solution to achieve high contrasts of the low X-ray attenuating minerals and to minimise beam hardening would be to combine multiple scans with different X-ray intensities. However, as the primary goal was to differentiate graphite from the gangue material, the acquisition parameter selected to image the graphite ore showed a good balance between contrast and beam hardening prior to the high absorbing phases. Thus, it was possible to differentiate between graphite, pyrite, pyrrhotite, rutile and silicate matrix based on the grey-scale contrast of the CT image.

Even though good scan quality was achieved, minerals may exhibit a large range of grey-scale values due to the polychromatic nature of X-rays and the co-occurrence of minerals with different X-ray attenuation. Reliable mineral segmentation of CT data, particularly of complex rock samples such as the specimen used for this study, is therefore challenging. However, using the deep learning algorithms for segmentation implemented in ORS Dragonfly, segmentation of minerals does not solely rely on grey value contrast, as it also considers textural features such as grain shape. By providing the DL model sufficient training data, it was possible to differentiate between areas exhibiting the same grey values. Such areas also contained imaging artefacts, produced by high-absorbing sulfide minerals (Fig. 2.5).

The accuracy of segmentation, however, may be limited due to certain factors. The first factor is the partial volume effect (PVE) (Glossary p. 107ff) [26]. If a single voxel consists of more than one phase, the CT number represents the average of the X-ray attenuation of all phases present. Consequently, all particles below voxel size are affected by the PVE and cannot be imaged. Directly related to the PVE is the blurring of the CT data, particularly in samples with phases of large attenuation differences, as in the investigated specimen [83]. Blurring complicates the interpretation of CT data, particularly at grain boundaries and for small particles, as it causes each voxel to contain portions of the surrounding voxels. Consequently, phases approaching the spatial resolution of the CT data also contain voxels that reflect the surrounding material. Segmentation will therefore lead to an over- or underestimation of the labelled volume [149]. One way to minimise the effect is to increase the image resolution, but this comes at the cost of sample size. Another method is to refine the segmentation result by eroding or dilating the segmented volume. However, it is not possible to fully eliminate these artefacts as they originated from the voxelised data themselves. In addition to imaging artefacts, another source of error is derived

from the manual segmentation process that must be conducted to provide the training data and at the inference stage (Glossary p. 107ff). These are the most time-consuming steps, and there will inevitably be some inadvertent errors in labelling among the large number of pixels (4064 × 4064) comprising each slice. Consequently, there will be some judgement errors for pixels located at grain boundaries and those reflecting small particles, due to the above mentioned PVE and blur artefacts but also regardless of them. Therefore, to minimise this bias, only graphite flakes comprising >100 voxels (ca. 25 µm ESD) were considered for the analysis.

A comparison of the topmost CT sample slice with the stacked OM image shows good agreement in terms of graphite content, number of particles and grain size distribution. However, several factors must be considered that hinder a direct comparison. Due to blurring, a complete overlap of the two cut surfaces was not possible. Further, the slight difference in the size of individual flakes (Fig. 2.12) and number of jumbo flakes, large flakes and super jumbo flakes (Table 2.7 and Table 2.8) may be explained by the fact that some flakes were not yet connected to the 2D radiograph and/or were incorrectly identified as two separate or one entire grain, respectively, because of the PVE. The PVE also affects the calculation of the total graphite content, as it results in an under- or overestimation of the segmented surface, as mentioned above. The lower number of identified amorphous flakes in the CT image can be attributed to both the scanning resolution and the PVE. Lastly, the slice was not part of the segmented volume as it represents the topmost slice of the cylinder. As mentioned above, the topmost slice is more affected by artefacts than inner slices. Surfaces that are parallel to the X-ray beam at the top and bottom of the sample will not penetrate properly, which will lead to image artefacts and thus a lack of detail in the data. Consequently, to be able to include the topmost slice in the volume, the scanning geometry should be mounted at a slight angle to avoid parallel alignment of the circular base and top surfaces of the cylinder to the X-ray beam. This reduces artefacts and thus enables a better comparison.

2.5 Conclusion

This study explored the use of CT for establishing the physical properties of graphite in geological ores. The results reveal that CT is a valid and innovative technique that can be effectively used to characterise graphite. It enables nondestructive, in situ 3D visualisation and provides quantitative information on critical mineralogical aspects such as flake size, flake size distribution, shape and impurities that cannot be determined with other currently available analytical tools.

Given that graphite raw materials should be assessed by their mineralogical properties [14, 130, 131, 137], the additional information provided by CT should allow improved resource recovery and beneficiation processes. By obtaining in situ information on flake size, flake size distribution and flake thickness before and after comminution, the yield of the process may be quantified. Thus, CT can provide information on ore characteristics and impurities in 3D, which may help to further improve the process design.

Prior knowledge on the samples' mineralogy is required to appropriately acquire quantitative CT data and allow the possibility of differentiating between similar attenuating phases. Furthermore, the resolution of CT is not as high as, for example, OM or SEM-EDS. Against this background, CT cannot be used as a stand-alone technology. Hence, in combination with traditional methods, CT allows for an improved understanding of graphite ores and products.

Chapter 3

DECT of graphite ore: enhancing image contrast

Key objective:	To investigate the effectiveness of DECT for enhancing image contrast on graphite ore
Focus:	Method development
Study material:	One sample of flake graphite ore

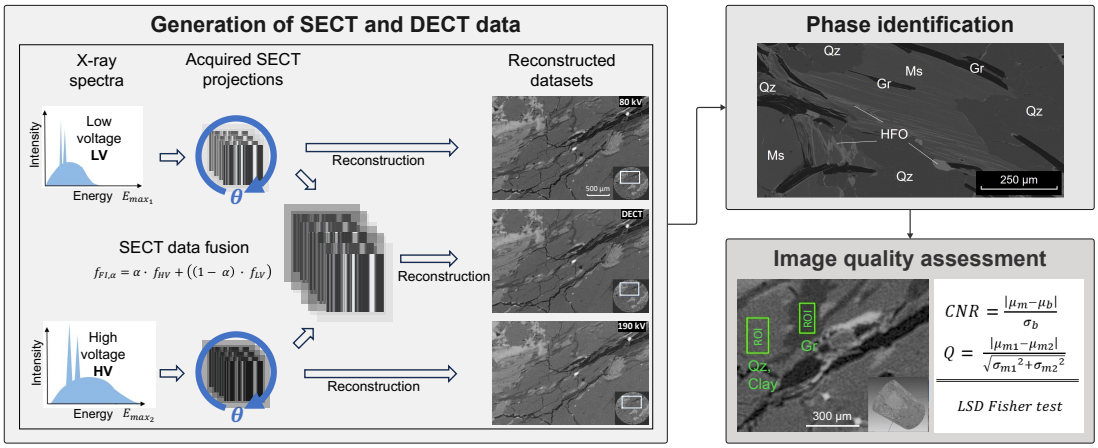

Authors:	*Leonard T. Krebbers, Natalia Grozmani, Bernd G. Lottermoser, Robert H. Schmitt*
Journal:	*Tomography of Materials and Structures*
Accepted:	*4 December 2023*
Citation:	*L.T. Krebbers, N. Grozmani, B.G. Lottermoser, R.H. Schmitt, Dual-energy computed tomography for improved contrast on a polyphase graphitic ore, Tomography of Materials and Structures 4 (100021) (2024). doi:10.1016/j.tmater.2023.100021.*

3.1 Introduction

An accurate assessment of ore deposits and the development of efficient extraction of ore minerals rely on a solid understanding of their mineralogy as well as their physical and chemical properties. To obtain this information, various analytical methods are employed, such as optical microscopy (OM), scanning electron microscopy equipped with an energy or wavelength dispersive X-ray analyser (SEM/E-WDX), electron microprobe analyser (EMPA), secondary ion mass spectrometry (SIMS), laser ablation inductively coupled plasma mass spectrometry (LA-ICP-MS), and X-ray diffraction (XRD) [150–153]. In recent decades, computed tomography (CT) has proven its added value in studying the mineralogical aspects of geological materials, with an increasing number of studies recognising its advantages for investigating rocks and ores [21, 32, 35, 84, 85, 94, 103, 139, 154]. Unlike conventional methods, CT offers quantitative and nondestructive 3D analysis with minimal sample preparation, eliminating the stereological bias [20, 155, 156]. This includes the ability to provide direct and more representative information on the shape, orientation, and size of phases without the need for time-consuming sectioning.

The CT principle is based on the X-ray attenuation behaviour of the phases comprising the sample, which is displayed by the contrast produced in the resulting greyscale image. The X-ray attenuation varies as a function of the material density, the Z_{eff}, and the thickness of the scanned object, as well as the X-ray energy applied [44, 47]. This difference in X-ray linear attenuation provides a contrast which can be used for mineral differentiation. The effective utilisation of CT depends on the X-ray beam's capability to penetrate the sample, enabling the visualisation of internal geometry [23, 47]. However, CT struggles to accentuate or distinguish between features that exhibit similar densities and effective atomic numbers. In this regard, ores often comprise complex polyphase geomaterials with a wide range of X-ray attenuation properties owing to their constituents' differences and/or similarities in density, atomic number, and particle sizes. This can make it challenging to acquire high-quality CT data of these materials, as it can lead to scanning artefacts and mixed attenuation coefficients that result in a partial overlap of grey values in the reconstructed CT greyscale image stack that hamper the interpretation and processing of CT data [46, 54, 118].

To obtain high-quality CT data, the proper X-ray energy must be selected, to optimise data quality, which is not always straightforward [157]. Higher X-ray energy is required to penetrate high-density materials or thicker sections, but it may cause a loss of contrast and unresolvable features. Conversely, using lower X-ray energy to obtain good quality imaging of light materials may not penetrate denser materials, resulting in loss of information [46, 158]. Thus, the choice of the advantageous beam intensity must be a trade-off between high and low-absorbing materials within the specimen to be examined.

Current and past research focused on the acquisition of high CT data primarily through the development of scanning protocols for the optimal scanning parameters to extract mineralogical and textural information in ore samples [26, 85, 100] and the development of an attenuation coefficient data bank in order to predict phase discrimination in ores [106, 107]. Another method that may contribute to the generation of high-quality CT scans of complex ores is dual-energy computed tomography (DECT). DECT has been widely established in medical imaging, sorting, and security applications [7, 159–161]. Notably, in the medical field, DECT has become a routine method for detecting anatomic structures and conducting contrast-enhanced studies to improve image quality [162–166]. In the context of analysing geomaterials, DECT has primarily been used for material decomposition [99, 111, 167, 168]. By utilising two different X-ray energies, DECT

enables the tracking of attenuation changes according to the X-ray spectra. This information can be harnessed to identify minerals in the samples and retrieve their density and effective atomic number Z_{eff} information. However, studies applying DECT to a polyphase ore and quantifying the improvement in image quality are sparse.

This study aimed to investigate the potential of high-resolution DECT for enhancing image contrast in a heterogeneous polyphase graphitic ore. The study utilised a sequential fusion approach to combine data obtained from different X-ray energy scans at high spatial resolution. Various X-ray energy spectra were combined with varying weighting factors to determine the favourable contribution of each energy level and spectrum, thereby aiming to provide the best possible attenuation of each phase. The findings of this study provided valuable insights into the establishment of DECT data and demonstrated the effectiveness of DECT in improving image quality in the context of complex geomaterials.

3.2 Materials and methods

3.2.1 Conventional analysis

A polymineralic flake graphite ore was provided by Westwater Resources, Inc. (Centennial, Colorado, USA). The specimen originates from the Bama Graphite Mine (Chilton Co., Alabama, USA), and consists of variable amounts of graphite as well as gangue phases (i.e., quartz, clay, muscovite, hydrated iron(III) oxide-hydroxides (HFO)). Mineralogical and petrographic investigations, including XRD, OM and SEM-EDS, were carried out prior to the CT measurements. XRD was used to determine the bulk mineralogy of the graphite ore sample. These steps are necessary to correctly interpret the CT data. For XRD analysis, a 2.5 g sample was ground in 100 % ethanol for 5 min using a McCrone micronising mill with synthetic agate pellets. After air-drying, the micronised aliquots underwent qualitative phase identification using the JADE (Rigaku, Tokyo, Japan) and EVA (Bruker, Billerica, MA, USA) software packages on a Rigaku Ultima IV powder X-ray diffractometer (Department of Earth and Atmospheric Sciences, University of Alberta, Edmonton, Canada). Mineral phases were identified by referencing the ICDD PDF4 + database. For petrographic analysis, a thin section, and a cylindrical-shaped polished block (12 mm in diameter, 5 mm in height) were prepared by MK Factory (Stahnsdorf, Germany). Both, the thin section, and the polished block were examined using a LEICA DM 2700 P polarisation microscope (Institute of Mineral Resources Engineering, RWTH Aachen University, Germany), and microphotographs were taken using a LEICA FLEXCAM C1 camera and the LEICA LAS software. The polished block was subject to SEM-EDS analysis to further investigate the mineralogy and microstructure of the graphite ore specimen, using a FEI 650 F scanning electron microscope equipped with two Bruker XFlash 5030 detectors (Institute of Mineralogy and Economic Geology, RWTH Aachen University, Germany) at 15 kV and 10 nA.

3.2.2 Computed tomography

A CT-ALPHA micro-CT system (ProCon X-ray GmbH, Sarstedt, Germany) was used, which is equipped with a five-axes-manipulation system between an XWT-240-TCHE plus X-ray tube with a maximum voltage of 240 kV and an XRD 1611 AP3 detector system with 4096 × 4096 pixels (100 mm^2) (Institute of Mineral Resources Engineering, RWTH Aachen University, Germany). The CT investigation was executed on the cylindrically shaped, polished block mentioned before. The specimen was placed between the X-ray source and the detector on the rotating table. The

resulting CT measurement is the collection of 2D sample projections (radiographs), taken as the sample rotates 360° around the vertical axis between the X-ray tube and the detector. The detector collects the intensity of transmitted X-ray photons of each projection and thus provides X-ray attenuation information. Based on this information, an X-ray attenuation coefficient is calculated for each pixel of the sample projection. This coefficient is displayed as a distinct grey-scale value in the projection image [169]. The acquired radiographs are subsequently processed using a reconstruction algorithm to produce a 3D volume represented by a cubic matrix of grayscale voxels (3D pixels).

3.2.3 Fundamentals of dual-energy computed tomography

Selecting appropriate acquisition parameters (e.g., voltage, current, integration time) for a polyphase sample like the one used in this study (i.e., a graphitic ore), comprising both, high and low X-ray attenuating minerals, is a crucial step that has to ensure that the radiation will also pass through the thickest and highest absorbing phase of the sample. Insufficient intensity can compromise the quality of the reconstructed image, complicating subsequent image processing. In theory, lower energy will increase the grayscale contrast of the reconstructed volume,while measuring with higher energy decreases any imaging artefacts but at the same time may reduce the contrast between low-absorbing phases with similar densities and different compositions. The main principle of dual-energy computed tomography (DECT) is to combine attenuation information from two conventional or single energy CT (SECT) scans performed at different X-ray energy levels to obtain a high-quality, single dataset. SECT scans can be fused before, after, or simultaneously with CT volume reconstruction. The CT scans fusion in this work was performed before the reconstruction and is based on a weighted linear combination of the respective low and high-voltage SECT projection stacks:

$$f_{FI,\alpha} = \alpha \cdot f_{HV} + ((1 - \alpha) \cdot f_{LV}) \tag{3.1}$$

where $f_{FI,\alpha}$ represents the fused projection image obtained through a weighted linear combination of the respective high-voltage f_{HV} and low-voltage projection f_{LV}. The weighting factor, α, is chosen from the range of [0,1].

3.2.4 CT data acquisition procedure

The cylindrical-shaped polished block was sequentially measured using five different voltage settings with 60 kV, and 80 kV reflecting the low voltage range (LV scans) as well as 170 kV, 180 kV and 190 kV comprising the high voltage range (HV scans). It is worth noting that maintaining an appropriate distance between the energy of the X-ray spectra of the two measurements is essential for obtaining appropriate DECT data [112]. Since the desired resolution was at the lower micron-scale, the block was positioned close to the X-ray source (SOD=24.5 mm). The focal spot size was set to microfocus beam mode to further increase spatial resolution. The beam current was adjusted accordingly for each scan to operate with 8 W, and the number of projections and averaging were kept constant. The exposure time was set to 1.6 s for all LV scans. To avoid saturating the detector, the exposure time in the HV range had to be adjusted to 0.8 s. The CT set-up parameters are summarised in Table 3.1. A Python script was used to generate the corresponding DECT raw data. Here, the weighting factors α were set to 0.3, 0.5, and 0.7 (Eq.1). A weight factor, of 0.3 for example results in 30 % of the high voltage projection, and 70 % of the low voltage projection image. All raw data collected were reconstructed using Volume Graphics

Table 3.1: Set-up parameters for the acquisition of low-voltage (LV) and high-voltage (HV) CT-scans.

Energy range	**LV**		**HV**		
Voltage [kV]	60	80	170	180	190
Power [W]	8		8		
Bining [#×#]	2 x 2		2 x 2		
Exposure time [s]	1.6		0.8		
Number of projections [#]	1600		1600		
Resolution [µm×µm×µm]	6.8		6.8		
Prefilter [-]	none		Al 0.4		
Part orientation [°,°]	0		0		
Averaging [#]	14		15		

VGStudio Max 3.5.0 [49]. Subsequently, 18 fused DECT datasets were generated, comprising six HV x LV combinations combined with three different weighting factors each.

3.2.5 Quality factors and statistical analysis

Grey value information for all reconstructed SECT and fused DECT datasets were obtained by placing regions of interest (ROI) in the following material areas (MA) (Fig. 3.1):

- Graphite attached to combined quartz and clay, hereafter referred to as MA1(Fig. 3.1A)
- Graphite in the vicinity of a void/crack (air), hereafter referred to as MA2 (Fig. 3.1B)
- Muscovite associated with HFO, hereafter referred to as MA3 (Fig. 3.1C)
- Muscovite associated with quartz and clay, hereafter referred to as MA4. (Fig. 3.1D)

The definition of the MAs was primarily based on the ore mineralogy's representativeness, target minerals focus, and grayscale intensity profiles. The material areas encompass five out of the seven identified phases and structures, with hematite and HFO excluded due to high mean grey value differences, facilitating straightforward segmentation. Every dataset contained 80 ROIs (10 ROIs for each phase and structure, or 20 ROIs per MA, respectively). After each ROI was created on the first analysed dataset, it was copied to the subsequent datasets to ensure they were identical in size, shape, and location. This resulted in 1840 ROIs considering all 23 datasets (five SECT acquisitions and 18 DECT datasets). Each individual ROI spanned multiple slices, with the specific three-dimensional extension determined by the attributes of the respective phases. Furthermore, care was taken to ensure that, to the greatest extent possible, each ROI exclusively contained a single material.

To simplify data extraction, two ROIs were placed adjacent to each other in each material area considered. This enabled the direct measurement of mean attenuation and standard deviation using the grey value analysis tool in VGStudio Max software, saving time, and streamlining the analysis process. Consequently, this approach allowed the generation of a dense amount of attenuation information. To quantitatively evaluate and compare the quality of each dataset, the contrast-to-noise ratio (CNR) was used to measure image quality in CT data. The CNR quantifies the ability to distinguish features in the scanned sample [170]. A higher CNR indicates higher grey value contrast and thus a better phase discrimination. Eq. (3.2) shows the calculation of the CNR, which measures the contrast as the difference between the mean grey values of the material and

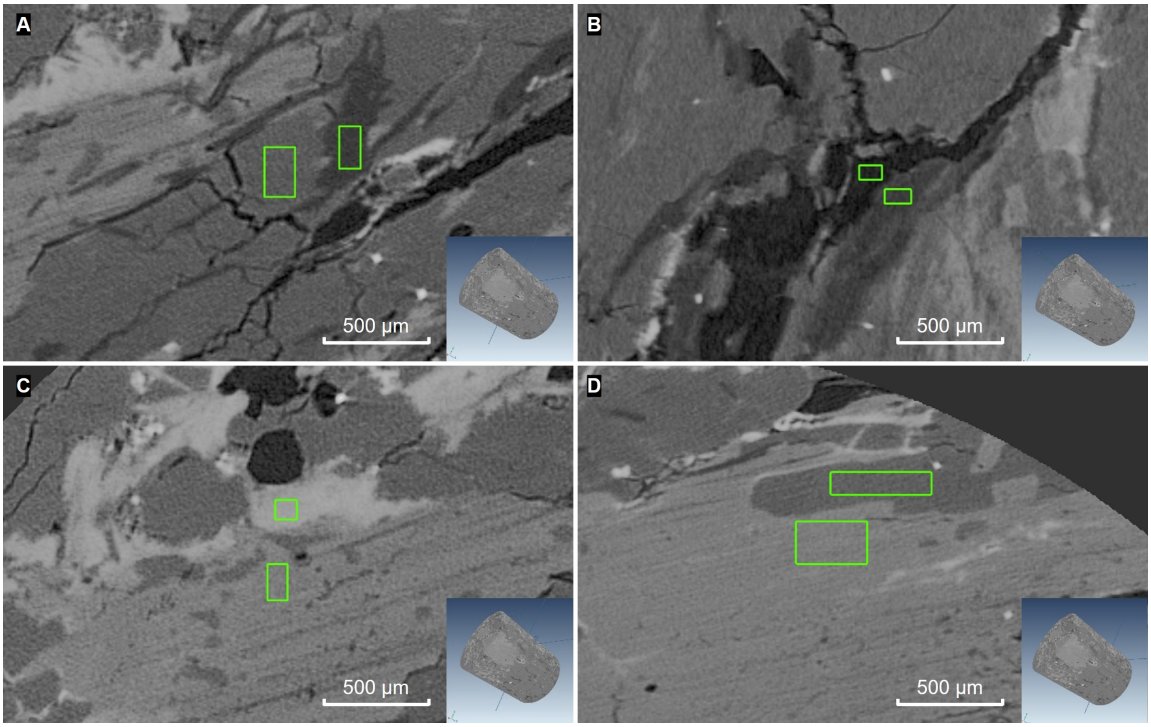

Figure 3.1: ROI pairs of the different material areas (MAs) evaluated: **A**) graphite associated with quartz combined clay (MA1), **B**) graphite in the vicinity of a void or crack (MA2), **C**) muscovite associated with HFO (MA3), and **D**) muscovite associated with quartz combined clay (MA4). An individual ROI consists of multiple slices and relies on the 3D shape of the respective constituent.

the background (μ_m and μ_b) divided by the background noise (σ_b):

$$CNR = \frac{contrast}{noise} = \frac{|\mu_m - \mu_b|}{\sigma_b} \tag{3.2}$$

Here, graphite and muscovite were the targeted minerals of the four material areas as listed above, and quartz combined with clay, HFO and void/air are background materials. However, in some other applications, both materials in the pair are equally relevant. To avoid the possible discussion of the background definition, the Q factors [158, 171, 172], which describe the materials separation degree, were additionally analysed:

$$Q = \frac{|\mu_m - \mu_b|}{\sqrt{\sigma_{m1}^2 + \sigma_{m2}^2}} \tag{3.3}$$

The results below focued on the CNR-based analysis. However, Q-factor-based analysis delivered the same trend (Table C.1, Table C.2). In both cases, the quality factors were calculated for each ROI of each material area and dataset (local quality factors). The local CNR/Q-factors are the quality factor values for a single ROI pair in the same material area (Fig. 3.1). The mean values and the standard deviations were calculated based on ten local quality factors of the same material area. The global CNR/Q-factor was calculated once per material area and parameter combination, so it has no standard deviation. The global mean and standard deviation for each constituent in an MA were calculated using the grey values for each ROI. Therefore, the global CNR/Q-factors show the trends but cannot verify the significance of the absolute differences. Thus, local CNR/Q-factors, their means and standard deviations were used to quantify the results. To prove the significance of the differences in image quality and material attenuation among the various SECT and DECT

measurements, a statistical analysis was performed. The multiple comparisons t-Test or paired t-tests with unequal variance, also known as the Fisher LSD test, was employed to compare the quality characteristics between the SECT and DECT datasets with different weighting factors. The Fisher LSD test starts from the hypothesis that the pair of given variances is similar and allocates them to two significantly distinguishable groups, if the probability of their similarity is less than a significance level. The significance level was set at 5 %. Each parameter combination was statistically analysed to define the significance of the mean value differences since calculated standard deviations were related to the mean values, not the global ones. Based on the test results, several significance groups were identified, and they are marked through letters from A to J (Group A reflects the highest CNR and Q factor values, and Group J (CNR) and Group G (Q factor) reflect the lowest). Parameter combinations in one significance group have no significant differences. Each parameter combination were compared to all other combinations of the same ROIs pairwise. Therefore, the parameter combination could belong to more than one group.

3.3 Results

3.3.1 Pre CT analysis

The sample comprised a heavily altered graphitic ore with a quartz-dominant matrix together with muscovite, clay, HFO, and hematite (Fig. 3.2). Graphite occured as euhedral to subhedral flakes ranging from large (up to 1000 µm in length), usually subparallel elongated clusters, to small, disseminated flakes (100 - 200 µm in length), which were occasionally bended or broken apart along basal cleavage (Fig. 3.2A-B). Some large clusters contained minor intergrowth of HFO. Quartz was present as primary subhedral (up to 600 µm in length) (Fig. 3.2A) or small recrystallised crystals (50 - 250 µm in lengths) showing triple junction texture. The ore were interspersed with cracks and features numerous cavities (Fig. 3.2B). Muscovite occured as euhedral to subhedral crystals (500 µm - 6 mm in length) showing different degrees of alteration with HFO occasionally occured along the basal cleavage planes (Fig. 3.2A). HFO were also present as veinlet and cracks infills as well as along grain boundaries (Fig. 3.2A), and Fig. 3.2C). Moreover, it appeared pseudomorph after muscovite and hematite (Fig. 3.2A).

3.3.2 Evaluation of CT image quality

Qualitative analysis

The volume slices depicted in Fig. 3.3 represent SECT scans conducted at different energy levels: a LV scan (*80 kV*), an HV scan (*190 kV*), and their corresponding fused DECT volume slices, generated using varying weighting factors of 0.3, 0.5, and 0.7. Seven different grey value intensities could be identified in both the SECT volume slices and DECT slices. These corresponded to (see numbers from 1 to 7 in (Fig. 3.3A):

1. air in voids and cracks (from dark grey to black),
2. graphite (dark grey),
3. combined quartz and clay (grey),
4. muscovite (from grey to light grey),
5. HFO after muscovite (light grey),
6. HFO vein-fill (from light grey to whitish), and
7. hematite (white).

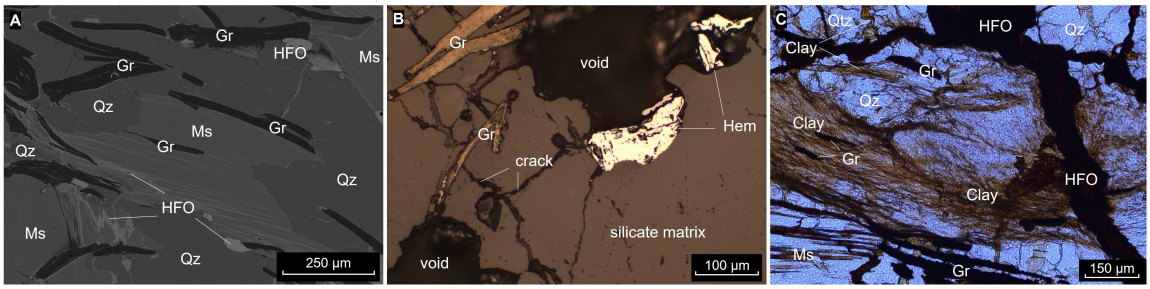

Figure 3.2: A) SEM image, **B**) reflected light microscopy microphotograph, and **C**) plane polarised light microscopy microphotograph of different areas of the graphite ore sample. **A**) Disseminated and subparallel orientated graphite flakes embedded in a silicate matrix of muscovite and quartz. HFO were present along cleavage planes of muscovite, pseudomorph after hematite (subhedral crystals) and occured along grain boundaries and in veins. **B**) Microphotograph showing two voids and two anhedral hematite grains. Graphite flakes were present. A network of cracks occured in the gangue matrix. **C**) Brown coloured microcrystalline clay were present throughout the specimen area. Note the thick vein fill of HFO. Abbreviations: Gr = graphite, Hem = hematite, HFO = hydrated iron(III) oxide-hydroxides, Ms = muscovite, Qz = quartz.

The SECT and DECT volume slices exhibited notable differences in noise, contrast, and sharpness. The SECT images generally appeared noisier compared to the DECT images (Fig. 3.3A-B). The DECT images with weighting factors of 0.3 and 0.5 showed similar noise, with the latter being slightly less noisy (Fig. 3.3C-D). In contrast, the DECT image with a weighting factor of 0.7 exhibited the highest noise level (Fig. 3.3E). Considering image contrast, the SECT volume slice obtained at 190 kV and the DECT with a weighting factor of 0.7 showed lower contrast than the other images. The other volume slices had similar contrast, with the data set reconstructed with a weighting factor of 0.3 appearing to have less contrast.

Regarding image sharpness, the SECT images exhibited partial blurring and occasionally showed double edges (see yellow box in Fig. 3.3A and Fig. 3.3F). These issues were alleviated in all the DECT images, with the one at 0.5 weighting factor appearing the sharpest among them (see red box in Fig. 3.3D and Fig. 3.3G). The histogram in Fig. 3.4 displays the grey value distribution of the *80 kV* scan (Fig. 3.4A), the *190 kV* scan (Fig. 3.4B), and the corresponding fused DECT data sets with a weighting factor of 0.5 (Fig. 3.4C). Each peak in the histogram corresponded to specific phases within the scanned sample. The better defined the peaks were, the less overlapping grey values existed, indicating a more definite phase assignment. The distinctness of the peaks and the degree of overlapping grey values differed significantly between the SECT and DECT histograms (Fig. 3.4D). The grey value material areas of materials like cavities and quartz were more compressed in the DECT histogram, indicating a more improved image contrast and a reduced overlap of grey values. Furthermore, the DECT histogram revealed an additional shoulder (Fig. 3.4C-D) that corresponded to graphite which is not visible in the other histograms (Fig. 3.4A-B).

Quantitative analysis

The quantitative analysis were based on the detailed CNR analysis of the established ROIs. Four different material areas (MA1, MA2, MA3, and MA4) were defined (Section 3.2.5), and the analysis was individually performed for each material area. The mean CNR values obtained for ten ROIs from all SECT and DECT volumes are shown in Table 3.2, and Table C.2. The mean CNR values for the SECT data within the ROIs range from 2.863 (MA2) to 5.745 (MA3), and global CNR

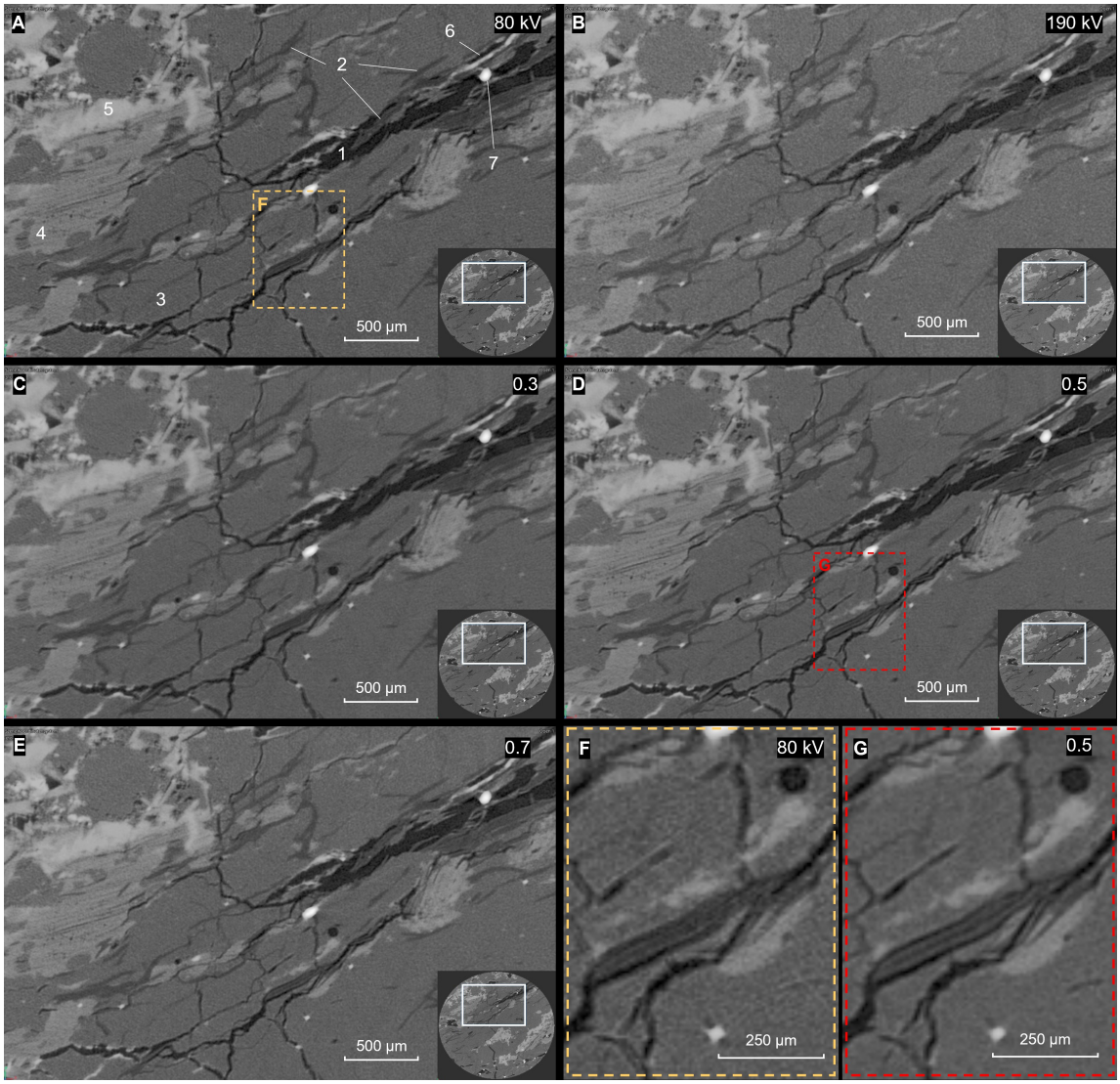

Figure 3.3: 2D volume slice of SECT and DECT volumes: **A**) 80 kV, **B**) 190 kV, fused dual energy scans with weighting factors of **C**) 0.3, **D**) 0.5, and **E**) 0.7. Numbering of phases: 1 = Air trapped in voids and cracks, 2 = graphite, 3 = combined quartz and clay, 4 = muscovite, 5 = HFO after muscovite, 6 = HFO vein-fill, and 7 = hematite. The **F**) yellow and **G**) red boxes, respectively, show a section of a graphite flake (centre of image) and N-S extending cracks and a small hematite crystal (lower centre). The graphite flake appears sharper, and the cracks are less blurred in the fused DECT scan with a weighting factor 0.5 (**G**). Note the small flake in the lower right of the slice, which is barely visible in the SECT volume slices compared to the DECT scan, and the reduced beam hardening introduced by a small hematite crystal. Window levelling was set to Smart Contrast for each slice to maximise contrast between each phase.

values – from 2.80 to 5.66 (Table 3.2). In contrast, mean CNR values for the DECT data ranged from 3.779 (MA2) to 7.646 (MA3), and global CNR values – from 3.73 to 7.44. Notably, in every ROI, most of the CNR values of the DECT datasets consistently surpassed those of the SECT datasets regardless of the weighting factor. Except for MA3, most CNR values of the fused DECT datasets differed significantly from those of the SECT scans. The DECT combination *80 kV x 180 kV x 0.5* showed the highest mean and global CNR values for the MA2, MA3, and MA4.

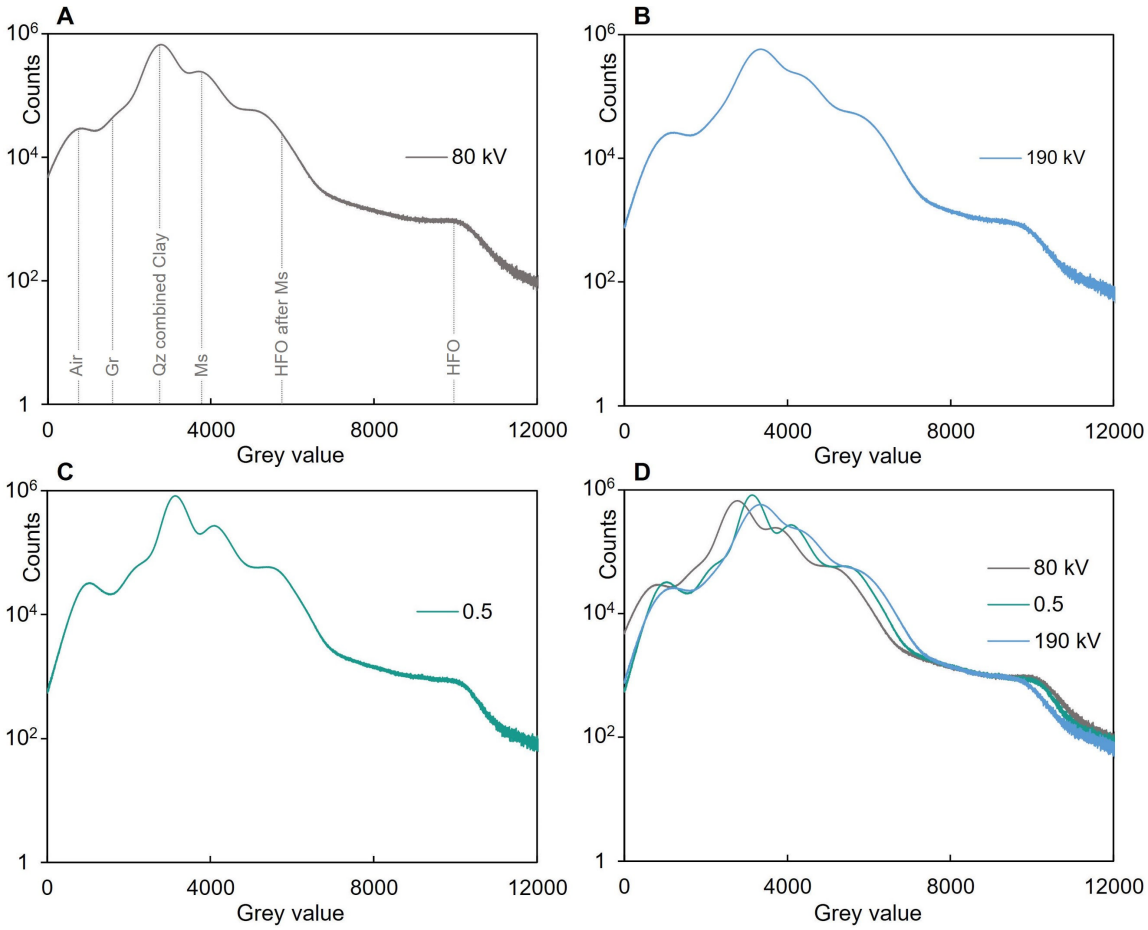

Figure 3.4: Histogram of grey value distribution (range from 0 to 12000) of SECT scans – **A**) *80 kV*, and **B**) *190 kV* – and **C**) the corresponding fused *80 kV x 190 kV x 0.5* dataset. A peak in the histogram indicated a phase contained in the scanned object. **A**) Histogram of the 80 kV scan showing the mean grey values of the phases comprising the samples apart from hematite which is out of the histogram range. Note that air refered to the air trapped within voids and cracks. **D**) Grey value distribution of *80 kV, 190 kV*, and the *80 kV x 190 kV x 0.5* DECT, note the evolved shoulder indicating graphite in the fused DECT dataset. Abbreviations: Gr = graphite, Qtz = quartz, Ms = muscovite, HFO = hydrated iron(III) oxide-hydroxides.

These combinations always belonged to group A. In MA1, the combination *80 kV x 190 kV x 0.5* exhibited the highest global and mean CNR value. In all ROIs, the mean CNR values of these two settings were significantly different compared to the vast majority of the DECT combinations. The *80 kV x 180 kV x 0.5* was in the same significance group (group A) as *80 kV x 190 kV x 0.5* (all MAs), *60 kV x 170 kV x 0.7* (MA1, MA2, and MA3), *80 kV x 190 kV x 0.3* (MA1, MA3, and MA4). The *80 kV x 190 kV x 0.5* was in the same significance group (group A) as *80 kV x 180 kV x 0.5* (all MAs), *60 kV x 170 kV x 0.7* (all MAs), *80 kV x 190 kV x 0.3* (MA1, MA3, and MA4). In contrast, the *80 kV x 170 kV* DECTs exhibit statistically lowest CNR values compared to the other DECT combinations.

The weighting factor 0.5 exhibited, in most cases, the highest absolute CNR values and was significantly better for some DECT combinations than other weighting factors on the MA1, MA2, and MA4. In contrast, apart from the *80 kV x 190 kV* DECT combination, factor 0.3 often showed

Table 3.2: Mean CNR values and results of Fisher LSD test for each material area and parameter combination from 10 ROIs for each phase and structure. Group A is the highest (marked dark green), and Group J is the lowest (marked dark orange) CNR group. Members of the same group have no significant differences. The mean CNR values which belong only to the best or only to the worst group of the considered material area, are marked in bold. The highest mean CNR value in each material area is marked bright green, and the lowest is bright orange. All mean CNR values belonging to the best group are highlighted in green, those belonging to the worst in orange.

Parameter combination	Material area							
	M1: Graphite - Quartz & Clay		M2: Graphite - Air		M3: Muscovite - HFO		M4: Muscovite - Quartz & Clay	
	mean CNR	*t-Test groups*	*mean CNR*	*t-Test groups*	*mean CNR*	*t-Test groups*	*mean CNR*	*t-Test groups*
60 kV	4.331	G H	**2.863**	J	**5.012**	G	3.800	H I
80 kV	4.518	F G	3.307	I J	5.726	D E F G	4.681	E F G
170 kV	**3.554**	I	3.985	H	5.745	D E F G	**3.488**	I
180 kV	3.658	H I	4.402	D E F G H	5.417	F G	**3.460**	I
190 kV	**3.548**	I	4.213	F G H	5.578	E F G	**3.329**	I
60 kV x 170 kV x 0.3	4.840	C D E F G	4.000	H	6.142	B C D E F	4.555	E F G
60 kV x 170 kV x 0.5	5.329	C D E	4.992	C D	6.812	A B C D	5.788	C D
60 kV x 170 kV x 0.7	6.167	A B	5.697	A B	6.924	A B C	6.334	B C
60 kV x 180 kV x 0.3	5.034	C D E F G	4.029	H	5.996	C D E F G	4.572	E F G
60 kV x 180 kV x 0.5	5.079	C D E F G	4.674	C D E F G	6.287	B C D E F	5.182	D E
60 kV x 180 kV x 0.7	4.610	E F G	4.800	C D E F	6.123	B C D E F	4.360	F G H
60 kV x 190 kV x 0.3	5.304	C D E F	4.103	G H	6.358	B C D E F	4.917	E F
60 kV x 190 kV x 0.5	5.505	B C	5.083	B C	6.973	A B C	4.930	E F
60 kV x 190 kV x 0.7	5.462	B C D	5.027	C D	6.687	A B C D	4.542	E F G
80 kV x 170 kV x 0.3	4.637	E F G	3.779	H I	6.315	B C D E F	4.337	F G H
80 kV x 170 kV x 0.5	4.707	D E F G	4.224	F G H	6.590	A B C D E	4.480	F G
80 kV x 170 kV x 0.7	4.426	G	4.318	E F G H	6.435	B C D E F	4.238	G H
80 kV x 180 kV x 0.3	4.655	E F G	4.124	G H	6.585	A B C D E	4.328	F G H
80 kV x 180 kV x 0.5	**6.401**	A	**6.062**	A	**7.646**	A	**7.056**	A
80 kV x 180 kV x 0.7	4.734	D E F G	5.006	C D	6.615	A B C D E	4.461	F G H
80 kV x 190 kV x 0.3	**6.417**	A	4.906	C D E	7.131	A B	6.595	A B
80 kV x 190 kV x 0.5	**6.594**	A	**5.711**	A	7.216	A B	6.701	A B
80 kV x 190 kV x 0.7	4.640	E F G	4.873	C D E	6.590	A B C D E	4.275	F G H

significantly lower CNR values. Especially on MA2, datasets calculated with the weighting factor 0.3 are significantly worse compared to the factors 0.5 and 0.7 of all DECT combinations apart from *80 kV x 170 kV* (same significance among all weighting factors). In MA3, there was no statistical difference compared to the fused datasets of the same combination and different weighting factors.

Regarding the CNR values of the SECT datasets, *80 kV* showed the highest global and mean CNR values than *60 kV* SECT (Table 3.2). In MA4, this difference was statistically significant. Furthermore, the HV datasets exhibited the lowest CNR values in MA1 and MA4. In contrast, concerning MA2, the CNR calculations of the LV datasets showed significantly worse values than the HV datasets. Within MA3, no general trend could be determined.

3.4 Discussion

DECT has primarily been utilised in geoscientific research for material decomposition, extracting density, and Z_{eff}) information on the basis of the raw projection data to differentiate minerals in rocks and ores [99, 111, 167, 168]. However, the quantification of improved image quality using DECT has not been elaborately discussed. Addressing this research gap, a comprehensive evaluation of image quality enhancement using DECT on a polyphase graphite ore was conducted by analysing the contrast-to-noise ratio (CNR) and Q factors of SECT and fused DECT scans. SECT scans were acquired at different tube energies and combined with varying weighting factors, further allowing to explore the impact of different proportions of the fused energy spectra on image quality.

3.4.1 DECT data acquisition

The findings revealed that fused DECT datasets have a positive and statistically significant effect on image quality in terms of CNR and Q factors regardless of the weighting factor applied compared to the SECT scans. Two mechanisms account for the improved contrast.

First, mathematically, the improved CNR and Q factors exhibited by DECT compared to SECT is attributed to the determined standard deviations of the reconstructed DECT data (denominator in both formulas). During CT data acquisition, the detector captures the material dependent attenuation of X-ray radiation from the exposed sample, converting it into different photon intensity that are then converted into CT numbers and stored in the form of projection data. The linear combination of SECT datasets in DECT involves mathematically merging the pixel values of corresponding projection pictures from each dataset. Through fusion, the projection data is averaged based on the weighting factor, leading to higher information density. Consequently, outliers become less significant, resulting in a lower standard deviation in the DECT data. This reduction in standard deviation contributes to the enhanced CNR and Q factors observed in DECT compared to SECT. This is a purely statistical effect, however, and a similar degree of noise reduction might be expected from combining two SECT datasets acquired at the same energy.

Second, the specimens' materials constituents (e.g., graphite, quartz, hematite, HFO, air) exhibit a different attenuation behaviour at different X-ray energies. At lower X-ray energies, the photoelectric effect dominates, which is more sensitive to the material's atomic number (Z) (proportional to Z^{4-5}) [42, 173]. This effect is particularly effective for phases with higher Z values. On the other hand, at higher X-ray energies, Compton scattering becomes more prevalent, and the attenuation is more dependent on the material's electron density [173]. For low-absorbing phases and those comprising similar densities (e.g., graphite, quartz), lower X-ray energies are better to avoid underexposure, as the photoelectric effect provides better contrast in these cases. Conversely, higher X-ray energies should be applied for high-absorbing phases (e.g., hematite, HFO), typically with higher Z values, to ensure sufficient penetration of the material and avoid overexposure. With DECT, two X-ray spectra are acquired at different energy levels. These energy-specific datasets contain complementary information about the attenuation characteristics of the scanned materials. Combining these datasets through DECT leverages the advantages of both lower and higher X-ray energies, resulting in improved contrast and more accurate differentiation of materials with a broad range of attenuation behaviours. The varying contrasts observed in the SECT and DECT datasets directly result from the different absorption properties of the minerals present in the sample at different X-ray energies. When comparing the LV scans and DECT combinations with equal energy fractions (weighting factor 0.5), it was generally noted that datasets acquired at *60 kV* provide slightly worse CNR values compared to combinations at *80 kV*, although not always significantly. Considering the target material is tungsten, the efficiency of producing characteristic X-rays decreases notably at energies below *80 kV*. As a result, bremsstrahlung becomes a greater proportion of the X-ray spectrum and the average energy of the X-ray beam decreases [174]. This, in turn, results in a higher degree of attenuation of lower energy X-rays and introduces noise. These effects may be amplified through the polymineralic nature of the sample. An exception is the *80 kV x 170 kV* DECT combination, whose CNR (and Q factor) values belong to the same significance group as the *60 kV* SECT combinations. However, this combination is the one with the most negligible difference in the fused energy spectra. According to [112], an appropriate distance between the energy of the X-ray spectra of the two measurements is essential for obtaining proper DECT data. The results of the CNR (and Q factor) values of the

80 kV x 170 kV, independent from the weighting factor and ROI, indicate that this difference was too small, thus underlining this finding.

DECT combinations utilising higher *LV x HV* energies consistently demonstrate significantly higher CNR (and Q factor) values with a weighting factor of 0.5 compared to the other DECT reconstructions. This observation is likely influenced by the specific mineralogy and microstructure of the sample, which tends to require higher X-ray energy levels from both spectra. This may also explain why the *60 kV x 170 kV* combination, with a weighting factor of 0.7, exhibits significantly higher CNR values than the same combination of 0.3 and 0.5. Otherwise, 21/24 of the fused reconstructed datasets exhibit the highest CNR values compared to weighting factors 0.3 and 0.7.

Grey value distribution in the evaluated material areas

Notably, all HV SECT settings exhibited statistically higher CNR values for MA2 compared to those obtained with the LV spectra. The underlying reason for this disparity lies again in the energy-dependent components of Compton scattering and photoelectric absorption of X-rays. Generally, scans at lower energies tend to provide better contrast due to the photoelectric effect, which is highly sensitive to Z and particularly effective for phases with high Z [43, 169]. However, graphite (Z = 6) and the main gases of air (nitrogen (Z = 7) and oxygen (Z = 8)) have very similar Z. On the other hand, there exists sufficient difference in their densities (graphite = 2.1 g/cm^3, air = 1.2e-3 g/cm^3 at 20°C). This density discrepancy becomes the dominant factor influencing X-ray attenuation at higher voltages, where the Compton effect prevails. As a result, scans with higher voltages demonstrate improved contrasts between graphite and air, as the Compton effect is more sensitive to the density of a material, compensating for the minor atomic number difference between graphite, and the major constituents of air. This is also reflected in the fused DECT datasets, where the weighting factor of 0.7 provided higher CNR values for three of the six combinations. Thus, the results show that the significant changes in the contrasts of the DECT datasets depend on both the combined voltages and the weighting factor.

A comparable trend is observed regarding the global CNR values of the various DECT combinations (Table 3.2). However, it is noteworthy that the CNR values within MA3 do not exhibit as significant differences as those observed in other material areas (e.g., MA2, MA1). Statistically, this can be attributed to the partly substantial variation in mean attenuation and standard deviation of the individual regions of interest (ROIs) within the HFO. From a mineralogical perspective, this could be influenced by varying Fe contents or different stadiums of pseudomorphism of HFO after muscovite at the locations where the ROIs were placed. This interpretation is supported by the varying brightness levels observed in the grey-scale images (Fig. 3.3), which suggest heterogeneity in the mineral composition within MA3. These compositional variations in the HFO may account for the observed similarity in CNR (and Q factor) values across different DECT combinations within this specific material area.

3.4.2 Limitations and future studies

The recommendations regarding the energy spectra and the weighting factor for the DECT fusion to be applied are based on one specific sample. Although the sample was extensively evaluated with 18 parameter combinations that were based on the establishment of 1840 grey value analysis, more empirical data on these types of geomaterials needs to be collected to further validate the findings. Additionally, like SECT, DECT also faces limitations in distinguishing between phases

with rather similar or identical attenuation properties such as quartz and clay. This constraint is inherent to all CT techniques and impacts on DECT as well [166]. Also, mineralogical data is necessary prior to any DECT analysis so that CT scans can be interpreted correctly [46, 54, 105]. Time is a further limiting factor when it comes to DECT, as it requires acquiring two SECT scans to generate the DECT datasets. This process at least doubles time and costs compared to obtaining SECT data alone. The contrast variations observed in the DECT datasets indicate that the combination of different X-ray energies significantly affects the image superior image quality, future studies should compare DECT scans with SECT scans having double the acquisition time. Regarding the preferential choice of the image quality metrics used, it was observed that CNRs are more responsive to noise in the background material. At the same time, Q factors are less susceptible to the same noise within a material area (Table C.2). This behaviour could be attributed to the denominator in the Q factor calculation, which considers the noise of both ROIs in the material area. Regardless, as the scope of this study did not encompass an in-depth comparison of these metrics, further research is needed to validate this observation. Lastly, future studies could consider the effect of other scanning parameters (e.g., exposure time and current) on the image quality of the fused DECT data.

The variation in contrast values observed in this study emphasise the critical role of selecting the appropriate X-ray energy level to optimise image quality and contrast, particularly in the context of heterogeneous geomaterials like the ones studied here. One of the central challenges in CT scanning, however, is finding the optimal scan settings for a given material due to the polychromatic nature of the X-ray beam. A common approach is calculating the linear attenuation coefficient for each phase in the sample [26, 118]. However, a polychromatic X-ray source is used in most CT applications, and the linear attenuation coefficient's energy dependency must be considered. Simulation software can be an effective tool for determining these optimal settings, especially in cases where the material's composition and internal structure are known in advance (e.g., workpieces) [158, 175]. However, the situation becomes more complex when dealing with geological materials. Buyse et al. successfully calculated reconstructed attenuation coefficients to differentiate between minerals in a heterogeneous geological sample for a given CT setup using simulation software [105]. The simulations assumed a monomineralic sample while considering factors such as sample geometry, chemical composition, and size. In practice, the ability to identify the appropriate scanning conditions for geological samples through simulation remains challenging due to the uncertainty surrounding the spatial arrangement and grain size distribution of the phases within the sample. Regardless, DECT proves to be significantly superior to SECT in terms of achieving high-quality data, making it particularly valuable for less experienced operators seeking to enhance image quality and data accuracy.

3.4.3 Implications for mineral characterisation

The accurate extraction of quantitative mineralogical data from ores and their constituents, such as volume, shape, grain size, and distribution, relies on the segmentation of CT datasets after volume reconstruction to isolate and classify the phases of interest. CT images are commonly segmented based on their greyscale intensities [169]. More advanced machine learning segmentation techniques also utilize object shape and pixel texture for feature classification [58, 60]. High image-quality CT datasets are essential for precise quantitative analysis, particularly for heterogeneous ores with a broad range of X-ray attenuation among their constituents, which may also exhibit similar grayscale intensities. To enhance image quality, datasets are often processed after reconstruction using various filtering methods. However, filtering techniques usually present a

trade-off: filters that decrease noise also blur the image (e.g. median filter, gaussian filter, and averaging filter), while those that increase image sharpness introduce noise into the image, leading to a potential data loss [176, 177]. In contrast, DECT effectively improves the image quality without compromising data quality. This advantage makes DECT particularly beneficial for more accurate segmentation, resulting in more precise and reliable identification of mineral phases and features. The enhanced image quality achieved for the investigated ore with the DECT-based approach provides a robust foundation for subsequent segmentation processes, ultimately enhancing the accuracy and reliability of quantitative mineralogical analysis.

The object studied in this research is a graphite ore. Previous studies have demonstrated the added value of CT for characterising graphite ores and enhancing resource efficiency [28, 33]. Building upon these findings, the present study offers additional insights into acquiring high-quality data on graphite ores. DECT, capable of addressing varying attenuation demands, shows great potential for the characterisation of such ores, which typically consist of high-absorbing materials like pyrite and hematite, along with air, while graphite exhibits low attenuation. By effectively managing these different attenuation properties, DECT enables the acquisition of appropriate contrasts for each phase, thereby enhancing the analysis of graphite ores and contributing to more accurate and detailed assessments of graphite ores.

3.5 Conclusion

This study explored the use of DECT for enhancing grayscale contrast of a heterogenous polyphase graphitic ore. A sequential fusion approach was applied to combine data obtained from different X-ray energy scans at high spatial resolution. Various X-ray energy spectra were combined with varying weighting factors to determine the favourable contribution of each energy level applied, thereby aiming to provide the best possible attenuation of each phase.

The results reveal that DECT provides complementary information on the material's attenuation characteristics that significantly improves the image grayscale contrast between individual phases comprising the investigated specimen compared to SECT. Considering the specimen investigated, higher energy DECT combinations and the weighting factor of 0.5 tend to provide the best image contrast regarding CNR and Q factor.

Given the complex microstructure and mineralogical composition of ores and the fact that the results are based on one particular sample, more research is needed to validate the findings of this study on a wider range of ore samples. Nevertheless, the findings suggest that DECT can be a valuable tool for improving 3D characterisation of polyphase graphitic ores. The additional greyscale contrast and image sharpness provided by DECT may allow for more accurate segmentation and thus quantitative mineralogical analysis. This could help to improve the understanding of graphite deposits and the development of more efficient extraction processes.

- this page is intentionally left blank -

Chapter 4

CT of tungsten ore: case study on morphological characterisation and modal mineralogy

Key objective:	To examine the mineral texture, modal mineralogy, and WO_3 grade of scheelite ore from Kara Fe-W deposit using CT
Focus:	Application
Study material:	Two scheelite ore samples

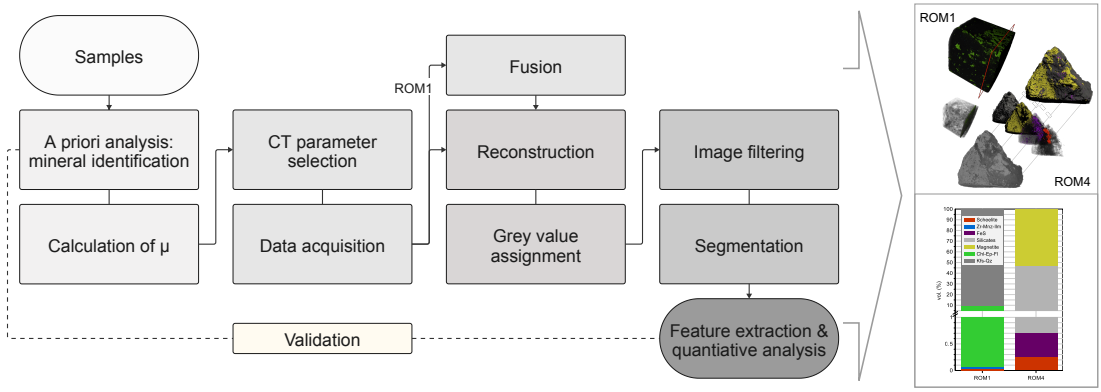

Authors: *Leonard T. Krebbers, Julie A. Hunt, Bernd G. Lottermoser*
Journal: *Minerals*
Accepted: *25 March 2024*
Citation: *L.T. Krebbers, J.A. Hunt, B.G. Lottermoser, Computed tomography of scheelite ore, Kara, Australia: morphological characterisation and modal mineralogy, Minerals 14 (4) (2024) 345. doi:10.3390/min13020247.*

4.1 Introduction

Tungsten, a brittle steel-grey metal, is primarily found in nature in wolframite and scheelite, with the latter contributing over 65% to known tungsten deposits [64]. Widely used in various technological applications, such as X-ray tubes, nuclear reactors, and high-performance magnets, tungsten is deemed a CRM by many advanced economies, exhibiting the highest economic importance according to the EU's CRM evaluation [5]. China is responsible for 85% of the global supply, holding 47% of the world's tungsten resources. Australia ranks second at 11%, with significant deposits found in various regions scattered across the country, such as Queensland, New South Wales, the Northern Territory, and Tasmania [178, 179]. Despite this, Australia contributes to only 1% of the global tungsten supply with three operating mines: Kara mine, King Island (both Tasmania), and Mount Carbine (Queensland) [180]. In fact, until late 2023, the Kara mine was the sole production site [180].

To efficiently extract mineral resources, ores must be accurately characterised in order to assess ore deposit quality and to maximising recovery [181]. Methods for analysing tungsten ores encompass a range of conventional techniques including X-ray powder diffraction (XRD), ultraviolet light, electron probe micro-analysis (EPMA), scanning electron microscopy with energy dispersive spectroscopy (SEM-EDS), cathodoluminescence (CL), inductively coupled plasma mass spectrometry (ICP-MS), laser ablation inductively coupled plasma mass spectrometry (LA-ICP-MS), and optical microscopy (OM) [e.g., 15, 182, 183]. These methods yield essential insights into the mineralogy, mineral chemistry, and geochemistry of tungsten ores. However, some techniques, like XRD, may not provide dimensional geometries of the analysed samples. Contrastingly, OM, SEM-EDS, and EPMA offer 2D visualisation of tungsten ores. Yet, these methods are timeconsuming, involve destructive sample preparation, and necessitate careful sectioning of original samples to select representative sample material. Furthermore, translating results from these methods into the third dimension can introduce stereological bias, which can be particularly challenging for low-grade ores with complex mineralogy and microstructure.

X-ray computed tomography (CT) enables the analysis of both bulk and spatially resolved microstructures of scanned objects based on the X-ray attenuation information of its components [44]. It allows for the non-destructive 3D visualisation and quantitative analysis of microstructural features in situ [44]. Over the past two decades, the technique has been successfully employed in numerous geological investigations [21, 28, 84, 184, 185]. CT has also proven its added value to the study of various ore types, particularly those comprising target minerals that exhibit significant attenuation contrast between ore and gangue minerals [26, 87, 93, 94]. To date, CT has been applied for measuring the tungsten content of a scheelite ore [35, 115] and its concentrate [36].

This study presents the first 3D reconstruction and quantitative analysis of scheelite ores from the Kara Fe-W deposit, Australia, using high-resolution CT. To date, there have been few studies, including technical reports on this deposit, that focussed on mapping, resource and reserve estimation, and formation history [186–190]. This research provides original insights into the volumetric and microstructural features of its tungsten ore minerals. Furthermore, it also introduces the application of a deep learning-based segmentation workflow for scheelite ore analysis that may be adapted to tungsten ores of similar composition. The ore grades (WO_3) calculated using CT were validated using inductively coupled plasma optical emission spectrometer (ICP-OES) analysis. Consequently, results of this study extend our existing knowledge of scheelite deposits and contribute to the development of advanced analytical protocols for the characterisation of metals ores.

4.2 Geological background

4.2.1 Regional geology

The Kara area's regional geology is characterised by Late Precambrian to recent volcano-sedimentary sequences and Devonian granitoids [191]. Precambrian rocks, forming the basement, consist of quartzose lithic wacke, phyllite, and minor dolomite. Cambrian to Lower Devonian units unconformably overlie the Precambrian rock and include the Success Creek Group (siliceous sandstone, mudstone, dolomite, and breccia) and the Criemson Creek Formation (mafic volcanic and volcano-sedimentary rocks) [189]. Overlying Ordovician to Lower Devonian rocks comprise the Mathinna Beds and the Wurawina Supergroup, further divided into the Denison, Gordon, and Tiger Groups [192]. The Denison Group features conglomerate, sandstone, siltstone, and argillite; the Gordon Group consists of carbonates; and the Tiger Group comprises quartzite with limestone fragments. Tertiary basalt and recent sand and gravel cover the area, concealing older units and mineralisation [192]. The Housetop Granite is an important Devonian granitoid located in northwestern Tasmania [189]. It intrudes volcano-sedimentary successions ranging from Precambrian to Lower Devonian. The granite is associated with many carbonate replacement deposits, including scheelite skarns and others. The deposits are located within 1 to 1.5 km from the intrusion [193], suggesting a spatial association with structurally weak zones [194].

4.2.2 Deposit geology

The Kara Fe-W deposit is located in northwestern Tasmina, Australia (41°18' S, 145°48' E) (Fig. 4.1). The Kara deposit area's geology features Cambrian rocks to the northwest, comprising laminated cherty mudstone with carbonates, locally transformed to hornfels or marble and, in places, to metamorphic skarn assemblages [189]. Ordovician units comprise massive and poorly bedded Owen Conglomerate and massive to weakly bedded and argillaceous Moina Sandstone, as well as impure limestone (Gordon Subgroup equivalent). Devonian granite is exposed in open cuts and often occurs in contact with skarns and showing alteration toward its margin. The granite consists of K-feldspar, quartz, and plagioclase, as well as accessory minerals like biotite, muscovite, epidote, hornblende, and magnetite. Amphibole appears to replace biotite. The granite generally shows an increasing intensity of alteration towards its margin, with feldspars altered to sericite or epidote. Calcite and fluorite are also present as veins in the altered zone. The Kara magnetite-scheelite deposit comprises several NNE-SSW trending skarn bodies (Fig. 4.1A), primarily developed within carbonates, sandstone, impure limestone, or transitional beds in the lower part of the Gordon Limestone. The skarns are in direct contact with the granite but may be separated from it by a thin layer of Owen Conglomerate or Moina Sandstone away from the contact (Fig. 4.1B). The Cambrian and Ordovician sequences were folded during Mid-Palaeozoic deformation, and these fold structures have been intruded by Devonian granite. Post-granite emplacement faulting includes dextral and thrust faults with small displacements [195].

Mining at Kara is by open cut and operated by Tasmania Mine Pty Ltd., with magnetite primarily mined and scheelite being extracted as a by-product (of magnetite processing operations). Mining has been focused on the Kara No. 1 orebody since extraction began in 1977. Estimates from a company report from 2016 show the total remaining mineable reserves of 9.9 Mt ore, averaging >30% of Fe, and averaging 378 ppm of WO_3 [187]. In 2018, the tungsten reserves were 3.66 kt WO_3 and a production of 0.025 kt WO_3 [179].

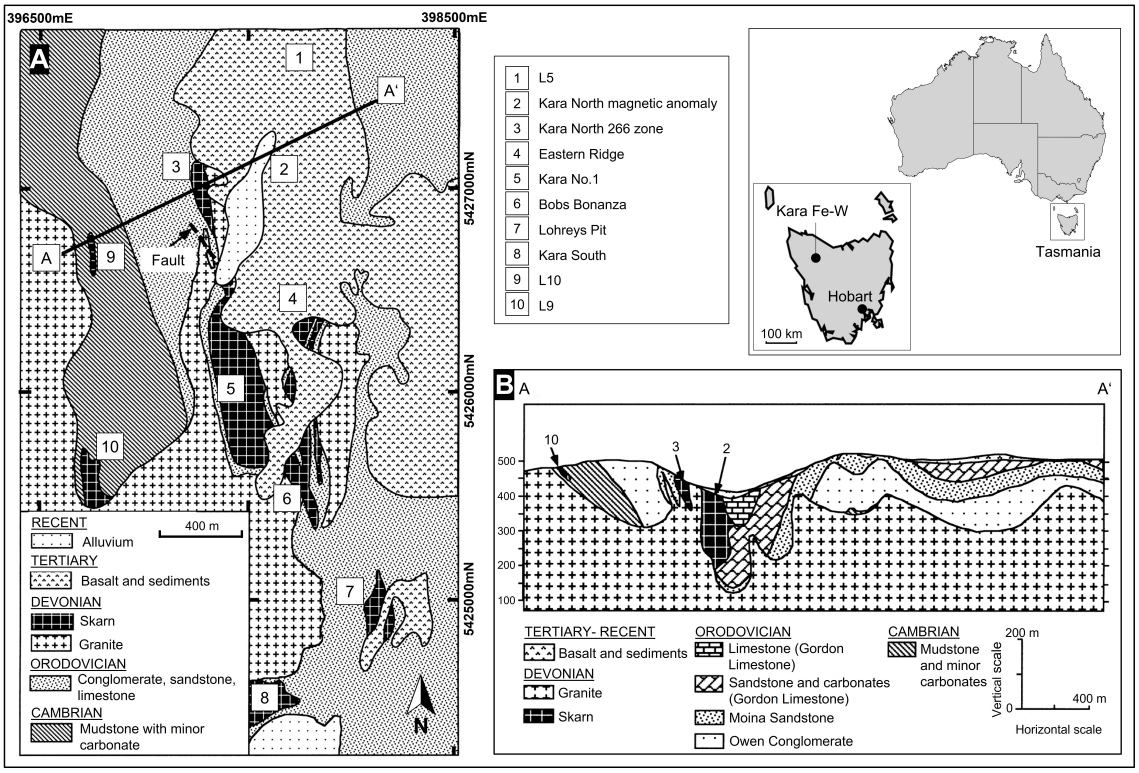

Figure 4.1: **A**) Geological map, and **B**) geological cross-section of the Kara Fe-W deposit area. Kara No. 1 is the sole orebody being mined. Modified after [189].

4.2.3 Deposit mineralogy

The primary skarn minerals at Kara include magnetite, garnet, vesuvianite, clinopyroxene, epidote, and amphibole, along with subordinate or accessory minerals such as fluorite, calcite, quartz, scheelite, hematite, chlorite, wollastonite, sphene, pyrite, chalcopyrite, and apatite [189, 190]. At least four stages of Skarn formation have been recognised at Kara (Table 4.1; [190]). Early skarn mineral facies, like garnet and pyroxene, underwent complete or partial replacement by later minerals, such as amphibole, epidote, and chlorite. According to [189], later minerals have developed by pervasive and diffusive replacement of earlier minerals, with a minor contribution from filling vugs, veins, and fissures. Early mineral facies are largely anhydrous, while later ones are predominantly hydrous. A detailed description of macroscopic and microscopic textural features of all mineral assemblages can be found in [187]. In the following, the major and minor occurring minerals of the stage III skarn formation are briefly summarised, as most of the scheelite deposition occurred during that stage [189]. In stage III, scheelite forms very coarse grains locally in excess of 5 cm and shows mutual grain boundaries with other stage III minerals. Magnetite is the most abundant mineral in stage III and shows grain sizes from fine (0.2 mm) to coarse (15 mm); occurs with amphibole; replaces earlier mineral assemblages; and forms as massive aggregates, fractures, or veins. Amphibole is primarily associated with scheelite and magnetite and occurs in hand specimens as fine to coarse grained (up to 5 mm) aggregates. Anhedral epidote shows mutual existence with other stage III minerals and exhibits variable grain sizes (0.2–10 mm). Fluorite is primarily associated with amphibole, epidote, and chlorite. Its grain size ranges from 0.1 to 5 mm.

Table 4.1: Mineral assemblages of the identified skarn formation stages after [190]. Note that minor chalcopyrite and bornite may also occur in the mineral paragenesis of skarn formation stage III.

Skarn formation stage	Paragenesis
Stage I	Clinopyroxene ± garnet ± vesuvianite ± wollastonite ± quartz ± scheelite
Stage II	Garnet-vesuvianite-magnetite ± scheelite ± apatite ± quartz
Stage III	Magnetite-amphibole-epidote-fluorite-quartz ± chlorite ± garnet ± vesuvianite± scheelite ±carbonate ± pyrite± clinopyroxene
Stage IV	Hematite ± fluorite ± calcite ± quartz

4.3 Materials and methods

4.3.1 Conventional analysis

Two ore samples from the Kara mine were collected on site from the run-of-mine (ROM) stockpile, reflecting two types of mineralisations: (1) a scheelite-bearing feldspar-rich host rock, and (2) scheelite-bearing magnetite ore. UV light was utilised during sample collection to confirm the presence of scheelite. Two polished mounts were prepared for automated mineralogy using the FEI MLA 650 scanning electron microscope (FEI Company, Hillsboro, OR, USA) equipped with two Bruker XFlash 5030 detectors operating at 20 kV and 7 nA. For quantitative mineralogical analysis, the Advanced Mineral Identification and Characterization System (AMICS) software (v3.1) package was used (Central Science Laboratory, University of Tasmania, Hobart, Australia). As the original sample mounts of the collected ROM material showed none to very minor scheelite on the polished surface (Fig. C.1), a third polished mount (ROM1) of the collected scheelite-bearing feldspar-rich host rock sample material was prepared as well as the selection of another sample of the collected magnetite ore material (ROM4) for CT analysis (Fig. 4.2). The ROM1 sample was subject to further petrographic analysis using a LEICA DM 2700P polarisation microscope (Institute of Mineral Resources Engineering, RWTH Aachen University, Aachen, Germany) as well as a FEI 650F scanning electron microscope equipped with two Bruker XFlash 5030 detectors operating at 15 kV and 25 kV and 10 nA (Institute of Mineralogy and Economic Geology, RWTH Aachen University, Germany). The final ROM4 sample was directly processed to CT analysis without additional preparation and petrographic analysis.

After the initial CT analysis, the samples were subject to XRD and ICP-OES analysis. For XRD analysis, 1.3 g of each sample was ground for 1 min using the TS 250 vibratory disk mill (Siebtechnik GmbH, Mülheim a.d.R., Germany). The micronised specimens underwent quantitative phase identification using the HighScore Plus software (v. 5.2, Malvern Panalytical, Almelo, The Netherlands) on a Malvern Panalytical Aeris benchtop powder X-ray diffractometer equipped with a Co source that operated at 40 kV and 8 mA (QXRD, Institute of Mineral Resources Engineering, RWTH Aachen University, Germany). XRD patterns were collected from 5 to 80° 2θ with an acquisition time of 60 min. Mineral phases were identified by referencing the ICDD PDF4 + database. For ICP-OES analysis, the same homogenised samples were subjected to microwave digestion using the MLS TurboWave (MLS Mikrowellen-Labor-Systeme GmbH, Leutkirch, Germany). The acid mixture consisted of 8 mL of inverted aqua regia (3 parts HNO3, 1 part HCl) and 2 mL of HBF4 (a hydrofluoric acid substituent). The W standards used had concentrations of

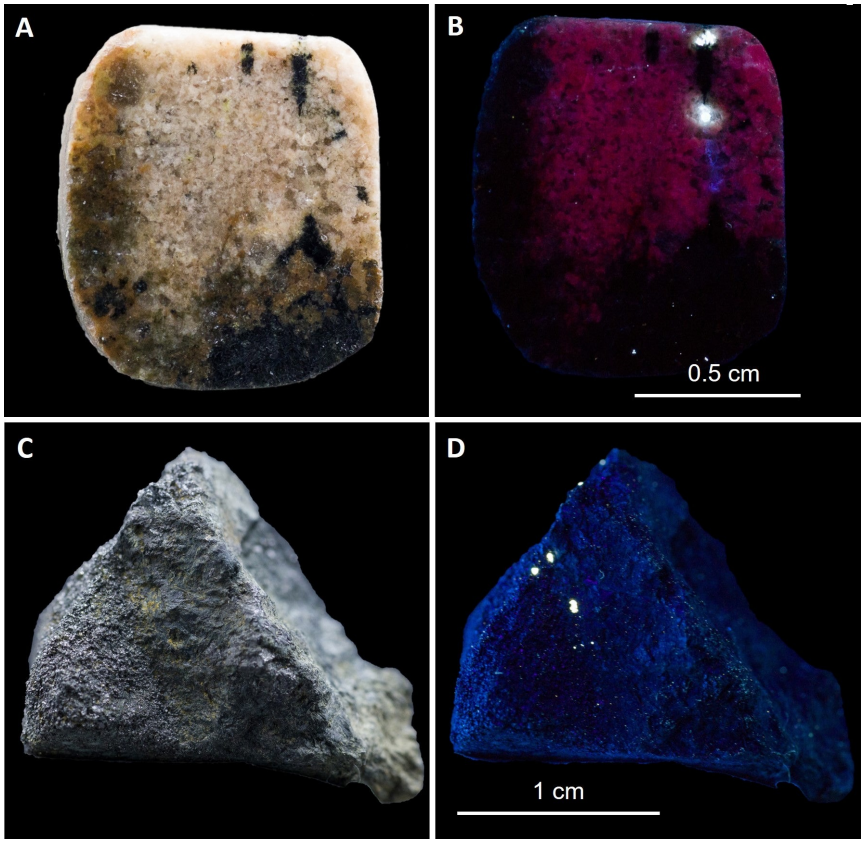

Figure 4.2: Samples used for CT analysis. **A**), and **B**) polished section of the ROM1 sample (scheelite bearing feldspar rich rock); **B**) under UV light. The purple and blue fluorescence colours can be attributed to K-feldspar and fluorite, respectively. **C**), and **D**) ROM4 sample (magnetite ore); **D**) under UV light. In both samples, scheelite is white under UV light, indicating a low concentration of Mo, as reported in [189].

1 g/L and 10 g/L, which were subsequently diluted according to the sample requirements. The calibrated range was 0.1 - 10 mg/L. The W content of both samples was then measured using the SEPCTRO ARCOS ICP-OES (SPECTRO Analytical Instruments GmbH, Kleve, Germany; Institute IME Process Metallurgy and Metal Recycling, RWTH Aachen University, Germany).

4.3.2 Computed tomography

A CT-ALPHA micro-CT system (ProCon X-ray GmbH, Sarstedt, Germany) was utilised, comprising a five-axes-manipulation system between an XWT-240-TCHE plus X-ray tube with a maximum voltage of 240 kV and an XRD 1611 AP3 detector system with 4064 × 4064 pixels (100 mm^2) (Institute of Mineral Resources Engineering, RWTH Aachen University, Germany). A specimen is placed between the X-ray source and the detector on the rotating table. During the measurement, 2D projections are collected as the specimen rotates 360° around the vertical axis. The detector collects the intensity of transmitted X-ray photons of each projection, providing X-ray attenuation information. From this information, an X-ray attenuation coefficient is calculated for each pixel of the sample projection. This coefficient is displayed as a distinct greyscale value in the projection image [21]. The acquired radiographs are then processed using a reconstruction algorithm to produce a 3D volume represented by a cubic matrix of greyscale voxels (3D pixels).

Table 4.2: CT scanning acquisition settings applied in this study. CT acquisition of ROM1 involved the fusion of two test measurements acquired at 150 kV due to acquisition issues.

Parameter	**ROM1**		**ROM4**
Voltage (kV)	150	150	180
Power (W)	8	8	8
Bining (#×#)	2x2	2x2	2x2
Exposure time (s)	1.6	0.8	1.9
Number of projections (x)	1600	1600	1600
Resolution (µm×µm×µm)	7.8	7.8	8.4
Prefilter (-)	Cu0.4	-	Cu0.4
Averaging (#)	4	4	12

Data acquisition

The successful application of CT relies on the X-ray beam's ability to penetrate the sample. X-ray attenuation is primarily governed by photoelectric absorption and Compton scattering, and it is influenced by material density, Z_{eff}, and applied X-ray energy [169]. The photoelectric effect prevails in low energies (approximately 50–100 keV), whereas Compton scattering dominates in energies > 5 MeV [42]. The likelihood of photoelectric absorption is highly dependent on the atomic number (Z), with absorption being proportional to Z^{4-5} [42]. In Compton scattering, the probability of X-ray absorption is proportional to Z, as the incoming X-ray photon interacts with a free or outer electron, ejecting it. Thus, the likelihood of this effect is more reliant on the electron density of the material [42]. Therefore, higher X-ray energies increase the penetration capacity of the X-ray and reduce beam hardening but may reduce image contrast of less dense and lower Z phases. Given that scheelite, the target mineral, possesses both high Z_{eff} and high density, high X-ray energies were applied to both samples (Table 4.2) to reduce beam hardening caused by the mineral.

Due to acquisition issues for ROM1, an image fusion approach of two test measurements was applied. Image fusion can be used to acquire dual-energy CT (DECT) data by the means of combining attenuation information from single-energy CT scans performed at different energy levels to enhance image contrast [39]. The datasets available in the present study were acquired at the same X-ray energy. However, the linear combination of SECT datasets also involves mathematically merging the pixel values of corresponding projection pictures from each dataset, resulting in higher information density. This reduces the significance of outliers, which in turn reduces the standard deviation and noise in the fused dataset. The scans were fused before reconstruction using

$$f_{FI,\alpha} = \alpha \cdot f_{VA} + ((1-\alpha) \cdot f_{VB}), \tag{4.1}$$

where $f_{FI,\alpha}$ represents the fused projection image obtained through a weighted linear combination of the respective scan A (f_{VA}) and scan B projection (f_{VB}). The weighting factor, α, was set to 0.5 to maximise the information density [51]. All raw data collected were reconstructed using Volume Graphics VGStudio Max 3.5.1 [49] applying a beam hardening correction.

Image processing

To enhance image quality, digital image filters were applied prior to segmentation using ORS Dragonfly (Version 2022.1, [61]). For ROM1, a median filter with a kernel size of 3 was applied to denoise the image. For ROM4, a three-filter combination was used. First, a median filter was applied, followed by the unsharp filter, using an unsharp factor of 3 to increase the edge contrast of grains. Since the unsharp filter produces noise, the median filter was applied again to denoise the image. Segmentation was carried out using ORS Dragonfly.

The software possesses deep learning algorithms that can be used for segmenting different phases simultaneously. Deep learning, a subset of machine learning, employs interconnected processors (neurons) predominantly built on a convolutional neural network (CNN) architecture (Glossary p. 107ff), known for its efficiency in image processing [145]. For accurate segmentation results, the network must be sufficiently trained to identify structures and learn how to make predictions (inference stage). Multiple regions of interest on various 2D image slices were manually selected to create ground truth data for training and validating the algorithm through supervised classification. Consequently, the network allows for automatic segmentation of the entire dataset. To accelerate the operating time of the segmentation procedure, the size of the volumes was reduced by excluding as much air as possible. For both datasets, a sensor3D model architecture [60] was chosen and trained. The accuracy of a model and thus the segmentation result depends on the network parameters, which need to be selected properly in accordance with the properties of the data information to be segmented. For each dataset, five classes were determined based on visual differentiating ability and paragenesis. Linear attenuation coefficients (μ) of the phases identified, using AMICS, OM, and SEM-EDS, were calculated (Table 4.3) to assist the manual labelling process. Initially, each class was labelled using an Otsu-threshold on a representative selected area (frame) of a 2D slice, followed by manual refinement. The model was then tested on a new slice, and any wrongly classified voxels were corrected and attributed to the training data until no further improvement was achieved.

4.4 Results

Results for scheelite-bearing feldspar-rich (ROM1) and magnetite-rich (ROM4) ores are presented below. First, a petrographic description using CT is given; note that the grey value assignment to the corresponding phases was guided by AMICS data (Fig. C.1), μ (Table 4.3), as well as OM and SEM-EDS (ROM1, (Fig. C.2). Second, the modal mineralogy and quantitative microstructural information of scheelite (volume, grain size distribution) are presented. Finally, the tungsten content from each sample is compared with ICP-OES analysis.

4.4.1 Petrographic description and modal mineralogy

The ROM1 sample comprises a quartz and K-feldspar dominated matrix, together with epidote, chlorite, minor fluorite, and biotite, as well as accessories of titanite, scheelite, ilmenite, zircon, and monazite. The applied acquisition parameters allowed for the visual differentiation between five minerals or mineral groups: (1) quartz; (2) K-feldspar; (3) combined chlorite, epidote, fluorite, biotite, and titanite; (4) combined zircon, monazite, and ilmenite; and (5) scheelite (Fig. 4.3A). In the process of segmentation, a background class (necessary for extracting the volume of the sample) and four mineral or mineral group classes were defined based on attenuation properties and genetic association, including class (1) = combined quartz and K-feldspar (hereafter referred

Table 4.3: Linear attenuation coefficients (μ) as a function of X-ray energy of all minerals identified by AMICS, XRD, UV light, OM, and SEM-EDS. The coefficients were calculated using the XCOM Photon Cross-Sections Database NIST [104].

Mineral	150 kV	180 kV
K-feldspar	0.36	0.34
Albite	0.36	0.34
Kaolinite	0.37	0.35
Quartz	0.37	0.35
Muscovite	0.40	0.37
Fluorite	0.47	0.43
Apatite	0.48	0.44
Actinolite	0.48	0.43
Ferro-edenite	0.48	0.43
Biotite	0.48	0.44
Diopside	0.49	0.45
Epidote	0.51	0.46
Chamosite	0.51	0.45
Ferro-kaersutite	0.52	0.46
Titanite	0.52	0.48
Andradrite	0.61	0.54
Chalcopyrite	0.79	0.66
Ilmenite	0.80	0.69
Pyrite	0.86	0.74
Magnetite	0.93	0.79
Bornite	1.02	0.83
Zircon	1.54	1.09
Monazite	2.96	2.00
Scheelite	6.48	4.23

to as kfs-qz); class (2) = combined epidote, chlorite, fluorite, biotite and titanite (hereafter referred to as ep-chl); class (3) = scheelite; and class (4) = combined zircon, monazite, and ilmenite (hereafter referred to as zr-mnz-ilm). Although the latter exhibits sufficient attenuation contrast (Table 4.3) to reflect a range of grey values, it was not always possible to clearly distinguish between these phases due to the fact the grey value intensity was influenced by the size of the grains, thus resulting in overlapping grey values.

Class (1) shows varying grain sizes (100 μm–2 mm) and exhibits minerals with anhedral to subhedral shapes. In some areas, K-feldspar is overprinted by chlorite (Fig. C.1). SEM-EDS data indicated that class (2) predominately consists of epidote and chlorite with minor fluorite and trace amounts of titanite. Although chlorite was not identified using XRD, potentially due to its detection limit and the fact that XRD struggles to identify sheet silicates, SEM-EDS data suggest that subhedral epidote (≤400 μm) and mostly anhedral chlorite (≤700 μm) occur in similar proportions with epidote, partially overprinting chlorite (Fig. C.2). In the CT data, a pervasive texture was observed with fuzzy grain boundaries (Fig. 4.3A-C). CT further showed that class (2) is spatially heterogeneously distributed (Fig. 4.4A) as well as in a up to 2 mm thick vein. Euhedral shaped zircon (≤50 μm) and anhedral monazite (≤40 μm) occur randomly in the ore matrix (Fig. 4.4B),

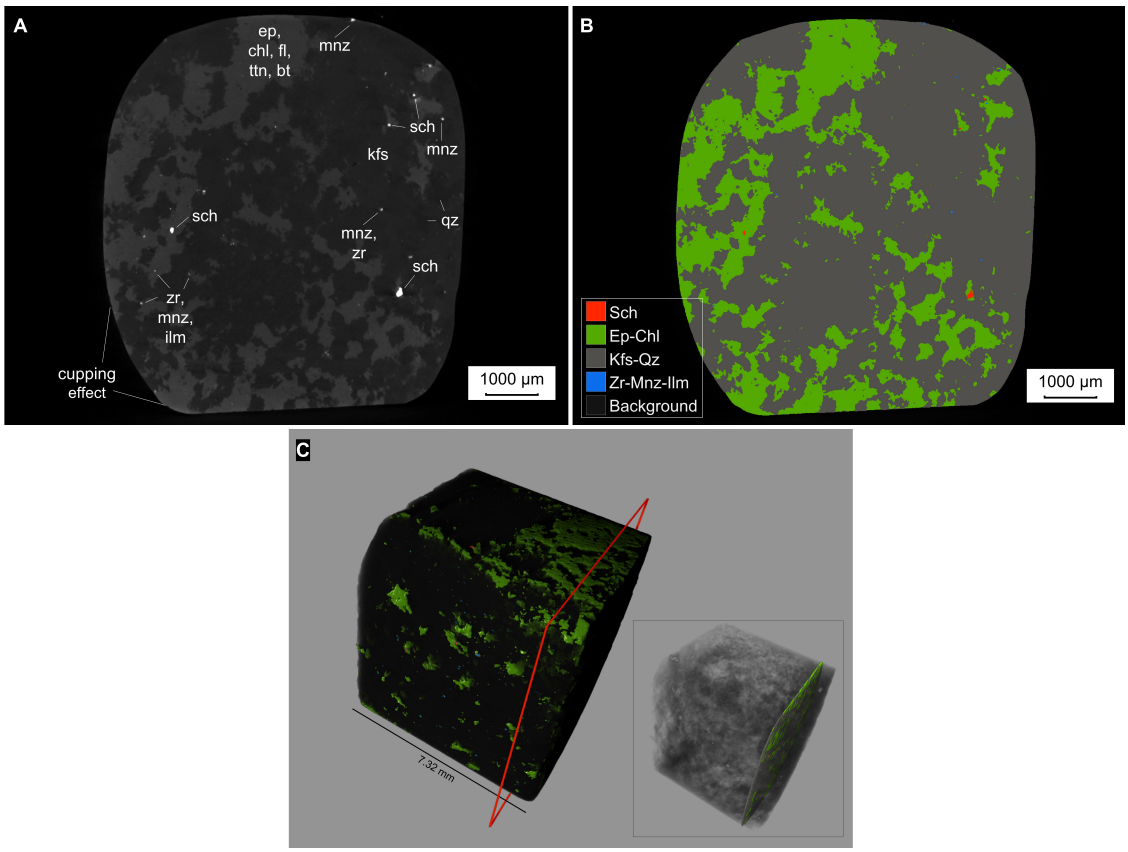

Figure 4.3: CT volume slice of ROM1 **A**) before and **B**) after segmentation. **C**) The rendered volume of ROM1 sample with the position of the CT volume slice, as indicated by the red square and the insert image. The thickness of the volume slice in the insert image is 10 µm. Abbreviations: bt = biotite, chl = chlorite, ep = epidote, fl = fluorite, ilm = ilmenite, kfs = K-feldspar, mnz = monazite, qz = quartz, sch = scheelite, ttn = titanite, zr = zircon.

showing mutual grain boundaries with the other minerals (Fig. 4.3A-B). Anhedral ilmenite is pseudomorphically replacing titanite.

Scheelite occurs disseminated in the silicate matrix (Fig. 4.4C), with grain size ranging from 10.48 to 360.88 µm in ESD (Eq. (2.1)), Table 4.4). Notably, most of the grains are spatially associated with ep-chl, with the majority of the volume embedded in the vein comprising ep-chl (Fig. 4.4A, (Fig. 4.4D). Apart from its association with chlorite and epidote, some scheelite grains show mutual grain boundaries with quartz and K-feldspar. The scheelite grains are orientated with their length axis parallel with the vein indicating a structurally controlled mineralisation (Fig. 4.4E). Larger scheelite grains show a subhedral to euhedral shape. The shape and the orientation of the smaller particles are not clearly identifiable due to the scanning resolution.

For the quantitative analysis of the CT data, the volume and voxel count were calculated from the segmented classes. The segmented volume of the ROM1 sample is 458.38 mm^3, with silicates making up the largest amount (411.77 mm^3) of the whole volume followed by ep-chl (46.34 mm^3). Scheelite and zr-mnz-ilm occur as accessories with 0.15 mm^3 and 0.12 mm^3, respectively. The volumetric proportion of the classes defined of ROM1 is summarised in Fig. 4.5A. Scheelite ranges in grain size from 10.48 to 360.88 µm ESD (Fig. 4.5B, Table 4.4) with an average size of 57.51 µm and a median of 48.71 µm ESD. The smallest particle has a volume smaller than 0.00001 mm^3.

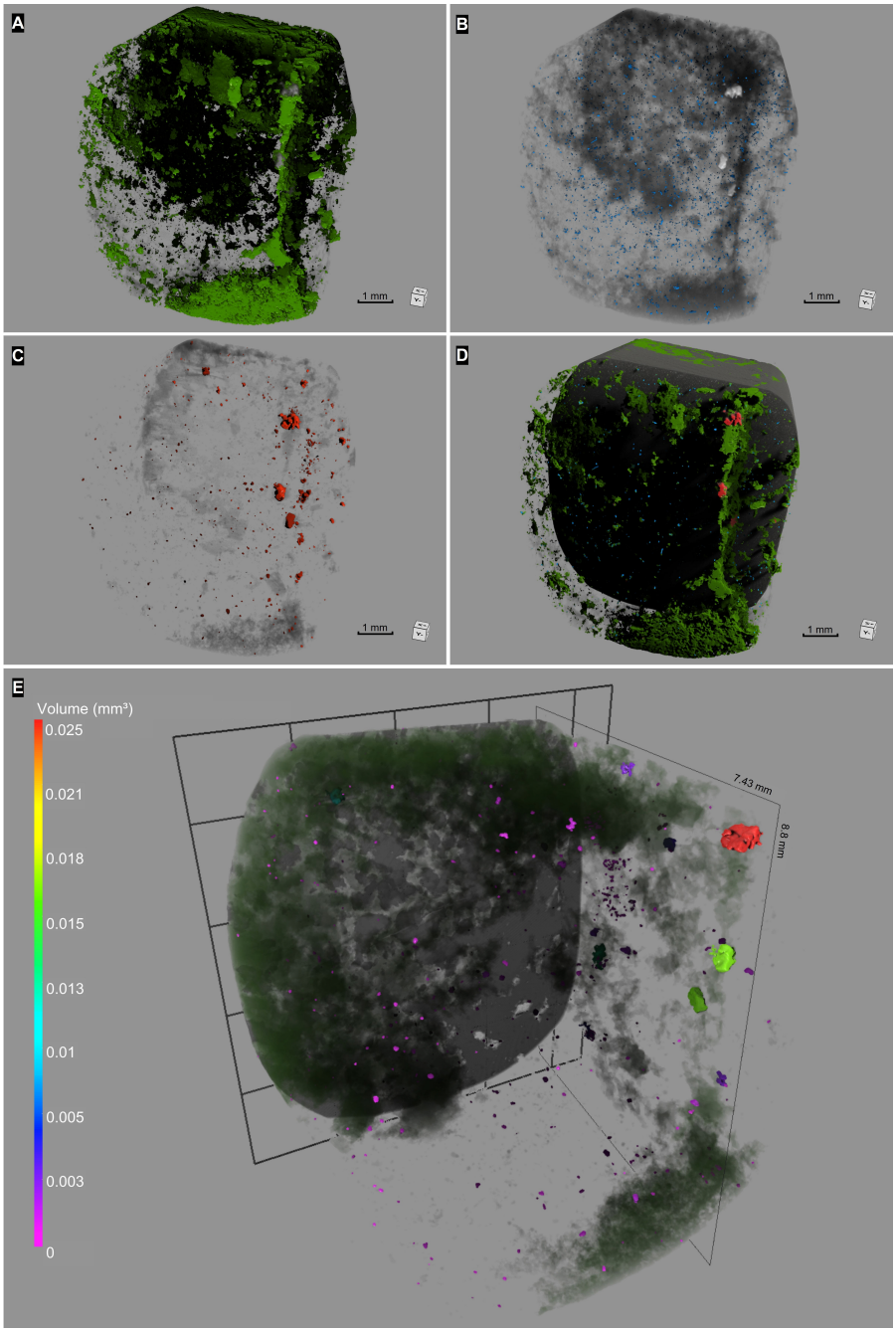

Figure 4.4: Spatial occurrence of the classes defined for ROM1: **A**) Epidote and chlorite with minor fluorite and titanite mainly exhibiting a fuzzy texture. **B**) Distribution of accessories comprising combined zircon monazite and ilmenite occurring randomly in the matrix. **C**) Disseminated scheelite particles. **D**) All classes combined including grey-coloured class consisting of quartz and K-feldspar with minor biotite that is partially clipped. Note that the majority of the scheelite particles are spatially associated with a vein comprising epidote, chlorite with minor fluorite and titanite. All other classes are set semi-transparent (**A**-**C**). **E**) Volumetric distribution of scheelite particles. Note the spatial association with the ep-chl class (coloured green and set semi-transparent), with most of the scheelite being embedded in a vein, as indicated by the black square.

Table 4.4: Textural properties of scheelite (P (n) = particle number, P (%) = percentage of particles, ESD = equivalent sphere diameter, vol. = volume). The particle volume was manually scaled using the volume classes defined.

Vol. (mm³)	ESD (µm)	P (n)	P (%)	Vol. (mm³)	Vol. (%)
ROM1					
>0.00001	10.13-26.56	36	8.28	0.0002	0.12
<0.00001-0.0001	27.51-57.64	251	57.7	0.01	7.25
<0.0001-0.001	57.75-122.41	134	30.8	0.04	26.16
<0.001-0.01	129.66-265.96	10	2.3	0.03	20.64
<0.01-0.1	282.74-360.88	4	0.92	0.07	45.82
Total		435	100	0.15	100
ROM4					
>0.00001	10.48-26.42	238	26.65	0.001	0.04
<0.00001-0.0001	26.96-57.5	388	43.45	0.01	0.59
<0.0001-0.001	57.62-126.38	212	23.74	0.06	2.64
<0.001-0.01	126.31-265.69	46	5.15	0.15	6.68
<0.01-0.1	278.67.473.35	5	0.56	0.14	6.08
<0.1-1	698.62-1238.93	4	0.45	1.94	83.96
Total		893	100	2.31	100

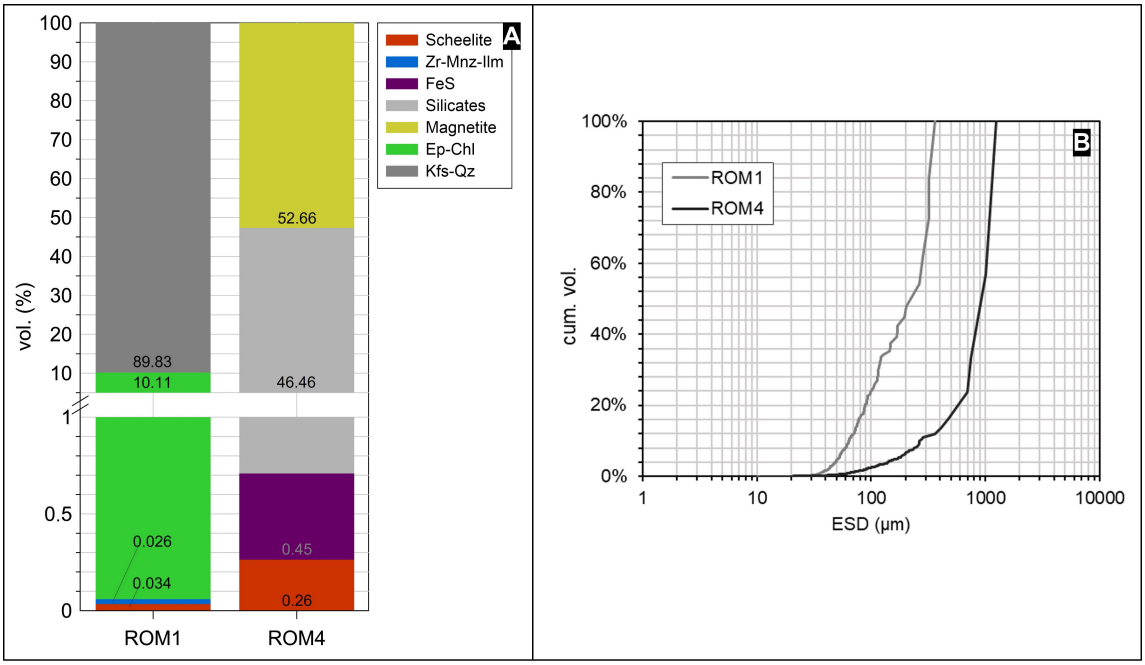

Figure 4.5: **A**) Modal mineralogy, and **B**) scheelite particle size distribution of the samples investigated as determined by CT. Abbreviations: chl = chlorite, ep = epidote, ilm = ilmenite, kfs = K-feldspar, mnz = monazite, qz = quartz, zr = zircon.

The majority of particles (57.7%) exhibit a volume ranging from <0.00001 to 0.0001 mm^3 (Table 4.4). However, the largest four particles constitute 46% of the total scheelite volume, with the largest particle exhibiting a volume of 0.025 mm^3.

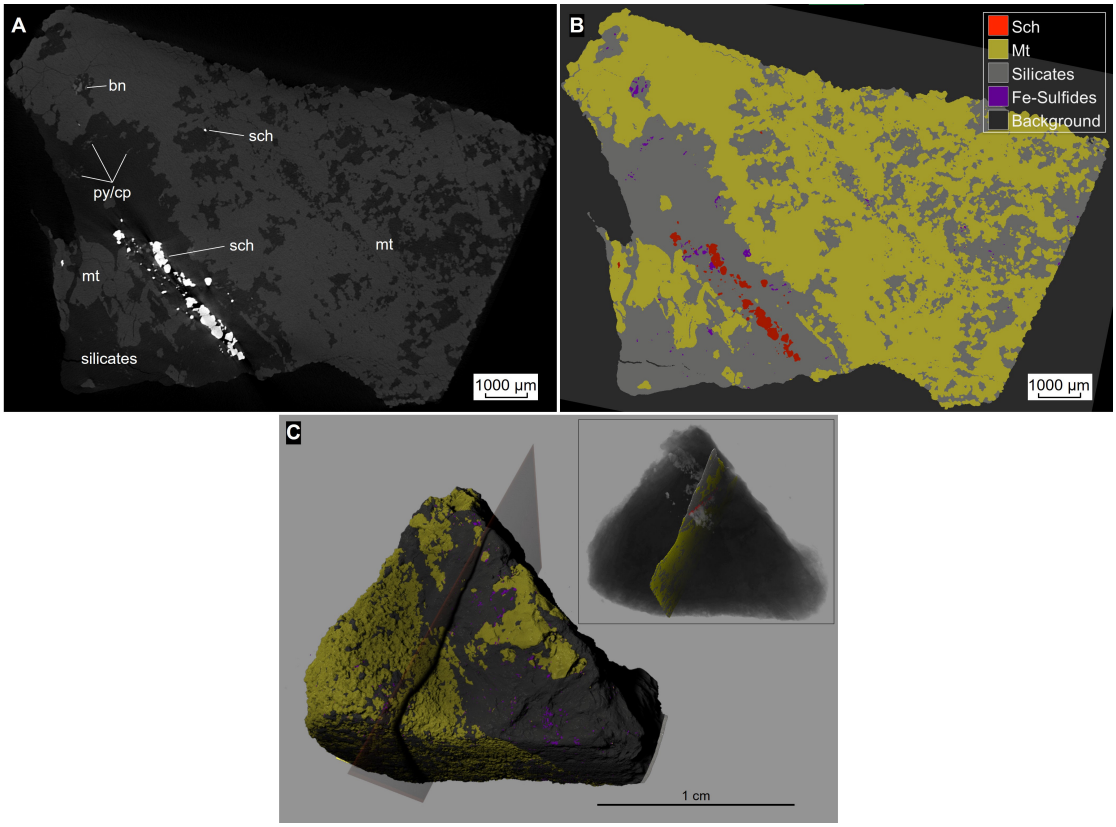

Figure 4.6: **A**) CT volume slice of ROM4 before, and **B**) after segmentation. **C**) The rendered volume of the ROM4 sample with the position of the CT volume slice as indicated by the semi-transparent square and the insert image. The thickness of the volume slice is 10 µm. Abbreviations: Bn = bornite, cpy = chalcopyrite, mt = magnetite, py = pyrite, sch = scheelite.

The ROM4 sample comprises magnetite together with silicates and minor scheelite. According to AMICS and QXRD data (Fig. C.1, Fig. C.3), the silicates mainly comprise amphibole with minor chlorite, andradite, quartz, and epidote, while some quantities of pyrite, chalcopyrite and bornite are also present. In the CT data, five visually distinguishable minerals or mineral groups were identified: magnetite, scheelite, pyrite/chalcopyrite, bornite, and silicates (Fig. 4.6A). The latter was unable to be further distinguished due to the X-ray setting applied. In the process of segmentation, five classes were able to be defined: background, scheelite, magnetite, silicates, and Fe-sulfides (pyrite, chalcopyrite, and bornite) (Fig. 4.6B). The Fe-sulfides were grouped as a single class due to challenges in clear discrimination by the naked eye, particularly with grains exhibiting replacement textures and smaller sizes (pyrite and chalcopyrite).

Magnetite exhibits two texture types. It occurs as massive agglomerates with euhedral grains (50 µm - 2 mm in length) showing triple-junction grain boundaries and as subhedral elongated, and partially aligned crystals embedded in a silicate matrix (up two 5 mm in length) (Fig. 4.6C). Between the agglomerates of magnetite, silicates are present with minor Fe-sulfides that are separated by a NW-SE trending vein (relative to the top surface of the sample) comprising silicates, Fe-sulfides, and scheelite 4.7A-D). In the vein, scheelite exhibits euhedral to subhedral grains that are elongated parallel to the vein (Fig. 4.7D-E). Within the vein structure, scheelite particles are often attached to each other thereby forming massive aggregates. The segmented 3D image of scheelite revealed that the majority of the scheelite volume is made of a few agglomerates

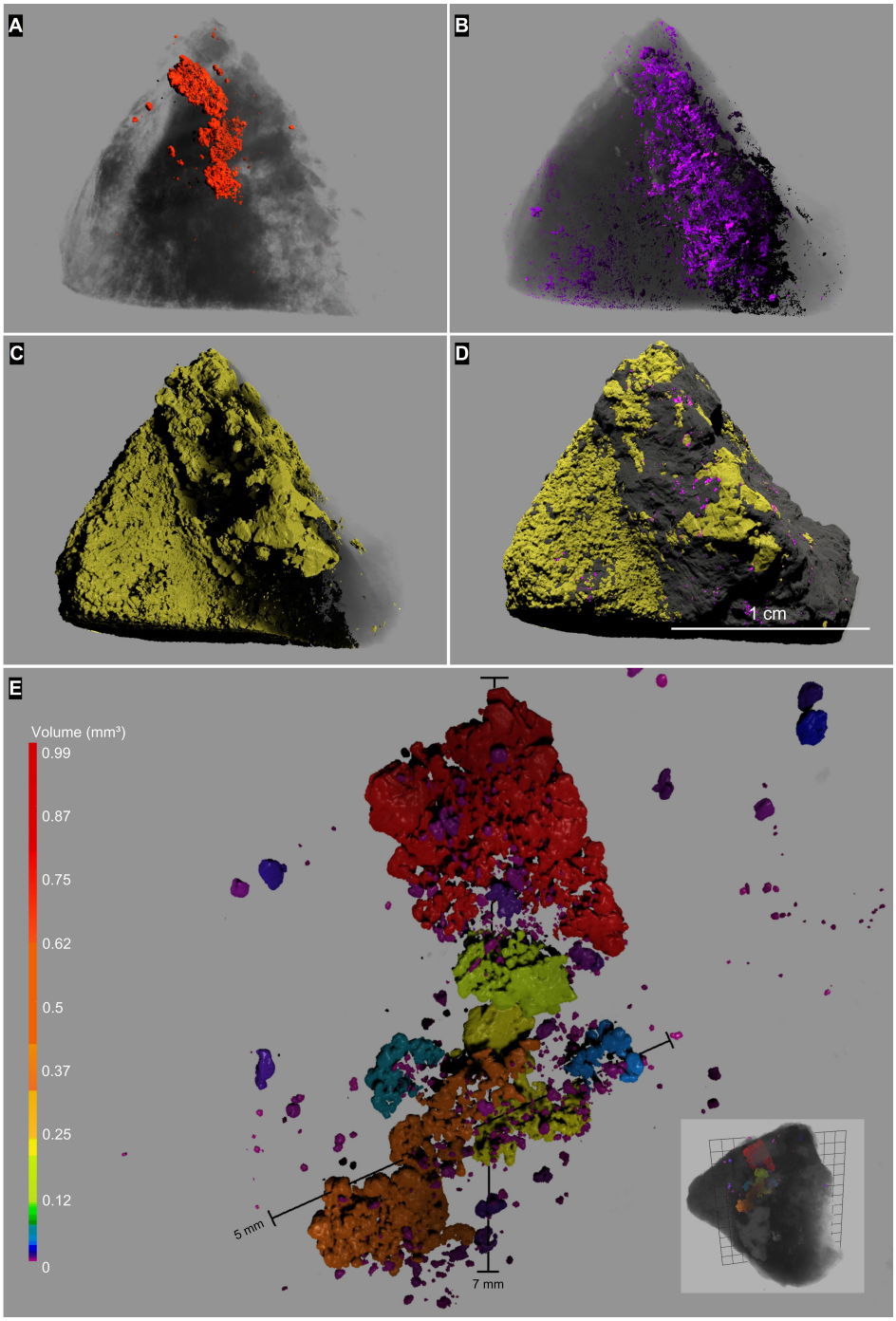

Figure 4.7: Spatial 3D distribution of the classes defined for the sample ROM4. **A**) Heterogenous scheelite mineralisation mainly occurring as vein-fill and a few disseminated particles in the vicinity of the vein. **B**) Fe-sulfides are mostly present in the silicate matrix. **C**) Magnetite comprising massive aggregates (left) and elongated grains parallel oriented to the dipping direction of the vein. **D**) Rendered volume of ROM4 with all segmented classes. Note that scheelite is not visible because it does not occur on the surface in this view. **E**) Volumetric distribution of scheelite mineralisation with fractured and subhedral-euhedral grains. The majority of the scheelite volume forms part of the vein. The ore matrix is set to transparent.

of scheelite grains attached to each other (Fig. 4.7E). A few medium to smaller grains, which are present in different areas than the vein, occur disseminated and predominately associated with silicates that is most likely actinolite and kaersutite according to XRD and AMICS data (Fig. C.1 and Fig. C.3). Some particles also share grain boundaries with Fe-sulfides and magnetite. However, it is important to note that most of these particles is in the vicinity of the scheelite vein (Fig. 4.7A).

Pyrite/chalcopyrite could be recognised by their texture (Fig. 4.6A-B) and lower X-attenuation compared to magnetite (Table 4.3). They occur as small anhedral fissures, occasionally displaying replacement textures with silicates. Bornite was able to be distinguished by its higher X-ray attenuation compared to magnetite as well as pyrite and chalcopyrite (4.3). It is present as small anhedral grains ($\leq$150 µm) in the silicate matrix that are occasionally attached to magnetite. The ROM4 sample volume is 879.1 mm^3. The sample volume is primarily composed of magnetite (462.92 mm3) and silicates (409.93 mm^3) (Fig. 4.5A). The volume of Fe-sulfides is 3.92 mm^3 and the volume of scheelite is 2.31 mm^3. Scheelite ranges in grain size from 10.13 - 1238.38 µm ESD (Fig. 4.5B, Table 4.4) with an average size of 55.77 µm and a median of 38.36 µm ESD. The sample contains 893 particles. Notably, 84% of the scheelite volume is made of four particles of which two of them contribute to 66.31% of the total scheelite volume. These are agglomerates attached to each other and or intergrown particles of scheelite grains attached to each other that form the majority of the scheelite vein-fill (Fig. 4.7E).

4.4.2 Validation

The ICP analyses resulted in WO_3 contents of 0.059 wt% (ROM1) and 0.32 wt% (ROM4) (Table 4.5). The magnetite content is 60.3% according to CT analysis. This is a difference of 4.3% compared to QXRD (Fig. C.3). Since the other classes comprise multiple minerals, a comparison was not possible.

Table 4.5: WO_3 content of the samples investigated as determined using CT and ICP-OES (sch = scheelite)

Sample	weight (g)	CT			ICP-OES	Δ WO_3 grade (%)
		sch vol. (mm^3)	sch wt. (g)	WO_3 grade (wt.%)	WO_3 grade (wt.%)	
ROM1	1.367	0.154	0.000939	0.055	0.059	6.85
ROM4	3.941	2.311	0.0141	0.29	0.32	9.12

4.5 Discussion

To date, there have been few mineralogical studies of the Kara Fe-W skarn deposit, with one primarily focusing on mineral identification [186], while others explored the development of skarn formation [189, 190], in general using predominantly geochemical methods and petrographic data obtained from optical microscopy. This study contributes additional mineralogical insights and introduces CT as a novel approach for investigating ore textures and modal mineralogy in selected samples of the Kara Fe-W deposit with a primary focus on scheelite. Key findings include: (1) scheelite is predominately spatially associated with hydrous silicates; (2) scheelite occurs as massive and fractured or disseminated, with vein-fill mineralisation controlling the

majority of the scheelite volume; (3) CT can be successfully applied to study scheelite ore textures in 2D and 3D; (4) CT of scheelite ore allows quantification of its modal mineralogy; and (5) CT analyses permit the quantification of the W grade (WO_3) of ore samples.

4.5.1 CT data acquisition

Previous studies utilising CT for the analysis of scheelite ores relied on conventional segmentation methods. For instance, Le Roux et al. [35] employed a local thresholding method, successfully differentiating scheelite from gangue and allowing for the quantification of ore grade. Warlo et al. [115], on the other hand, (qualitatively) determined modal mineralogy using watershed segmentation. While effective for phases with large attenuation differences, these methods yielded unsatisfactory results for phases with similar grey values, exacerbated by acquisition issues such as image noise, beam hardening, and the cupping effect (Fig. 4.3A) [115]. In this study, a deep-learning-based segmentation method was applied, representing the first documented use of application in the context of scheelite ore analysis. Unlike histogram-based segmentation, deep learning algorithms used and trained for segmentation consider additional feature information, such as grain shape and grain boundaries [60]. This consideration minimises the impact of scanning artefacts (Fig. 4.3), sample geometry (ROM4), and overlapping grey values, resulting in a more accurate quantitative analysis, particularly of similar attenuating phases.

The segmentation method employed in this study quantified the entire sample, with the resolution capacity being constrained by the sample size or the system's field of view. The chosen acquisition parameters resulted in voxel sizes of 7.8 µm (ROM1) and 8.4 µm (ROM4) (close to resolution limit of the scanner). Despite this relatively high scanning resolution, certain challenges arise, particularly for the smallest segmented particles which are affected by the partial volume effect (PVE). Considering that a voxel represents the average value of the attenuation coefficients over its volume, the PVE occurs where multiple particles contribute to a single voxel, resulting in blurring intensities of phases and structures. This phenomenon compromises the accuracy of the calculated grain sizes, as well as the representation of real shapes and grain boundaries, and can lead to over- or underestimation of the labelled volume [32]. Even with modern DL-based segmentation models, the PVE cannot be eliminated, as it is inherent to the voxelised data. In the case of ROM1, scheelite is disseminated in the ore and exhibits small grain sizes. At the same time, other dense phases, such as zircon and monazite, are present. As a result, small scheelite grains inevitably suffer from the partial volume effect, showing mixed attenuation coefficients and lower grey values that may overlap with larger zircon and monazite grains. Mixed attenuation coefficients also complicate manual segmentation for establishing training data for the deep learning model, introducing the potential for labelling errors by the operator.

The image noise in the CT data from ROM1 was improved through the fusion of two single CT scans at the same X-ray energy. When aiming to differentiate between as many phases as possible, DECT can also be considered, as it may improve the grayscale contrast between individual phases [39]. This, for example, could potentially reveal if scheelite is preferably attached to a specific hydrous phase as the high-voltage setting applied does decrease image contrast of lower X-ray absorbing phases. Furthermore, to enhance the representation of smaller grains, higher scanning resolution and longer acquisition time should be considered.

Additionally, nano-focused CT sources with resolutions down to hundreds of nanometers can be utilised, but this comes at the cost of scanning smaller sample sizes due to a reduced field of view and thus sample representativity (smaller sample volume). However, in the present study, the

proportion of small grains contributing to the total scheelite volume is negligible. The accuracy of the segmentation results was validated by comparing the calculated WO_3 grades of the two samples to conventional ICP-OES analysis (Table 4.5), showing a strong correlation between CT and ICP data. Furthermore, the magnetite content in ROM4 calculated using CT closely matched the results obtained from QXRD measurements (see Fig. 4.5 and Fig. C.3). This validation underscores the reliability of CT in scheelite ore characterisation.

4.5.2 Implications of CT analysis

Scheelite ore genesis

The mineral assemblages and the textures observed in the samples studied indicate that they are likely part of stage III skarn formation (as defined by Zaw and Singoyi [189]). In addition to scheelite, both samples contain hydrous minerals such as amphibole, epidote, and chlorite, while ROM4 also features massive magnetite, Fe-sulfides (e.g., pyrite, chalcopyrite and bornite). The pervasive texture of hydrous minerals in ROM1 suggests the replacement of earlier phases, indicative of retrograde hydrous skarn conditions. Previous studies further reported that earlier minerals were replaced through pervasive and diffusive replacement, with a minor contribution from filling veins and fissures [189, 190]. However, the rendered and segmented volume of ROM1 shows both an ep-chl vein exhibiting a pervasive texture with fuzzy grain boundaries (Fig. 4.4). Similarly, the 3D texture of ROM4 reveals a vein predominately composed of silicates and scheelite (Fig. 4.6). In addition, in both samples, scheelite is distributed within a vein where most of it is aligned parallel to the vein's dipping direction (Fig. 4.4 and Fig. 4.6). This suggests that a larger proportion of mineralisation occurred as vein fills, particularly scheelite mineralisation, than previously reported [189, 190]. It is noteworthy that the recognition of coexisting textures was more easily achieved with 3D information than with 2D. Regardless, it is important to consider that the observations were based on two specimens, and further data are needed to confirm this.

Although both samples show similarities (e.g., presence of hydrous minerals and spatial association), they differ significantly in terms of scheelite content. In ROM1, scheelite is present as a trace mineral (550 ppm WO_3). Therefore, although scheelite mineralisation mainly occurred during stage III, it does not necessarily mean mineral assemblages reflecting this stage contain high scheelite concentrations. Given the high amount of magnetite in ROM4, compared to 378 ppm WO_3, the average WO_3 content of the Kara Fe-W deposit, the results indicate that more scheelite is present when associated with magnetite. This observation aligns with previous observations of Zaw and Singoyi [189], who state that the majority of scheelite deposition occurred cogenetically with magnetite mineralisation during the late stages of skarn formation. Considering the distribution of scheelite in ROM4, the higher concentration of W could additionally be attributed to a structural controlled vein fill of W-rich fluids. Regardless, additional data are needed to further discuss on the formation model of the Kara Fe-W deposit.

Even though a high scanning resolution was applied, it falls short of offering detailed insights into mineral reactions and grain boundaries, especially notable in the case of ROM1 with fine grained scheelite particles (mixed attenuation coefficients). As a result, a comprehensive examination and discussion of mineral textures, reflecting mineral reactions and intricate replacement processes, is only achievable through additional 2D petrographic methods. On the other hand, however, CT clearly allows the recognition of grain shapes and major mineral textures (e.g., chlorite-epidote). Moreover, the capability for 3D visualisation distinctly highlights the presence of veins containing chlorite, epidote, scheelite, and fluorite, elucidating their spatial association. In fact, the 3D visu-

alisation offers a real benefit to petrographic studies of this type of ore with a preferred textural occurrence (e.g., vein). Additionally, CT can be used to guide subsequent sectioning, when aiming for a higher resolution and obtaining complex petrographic information, e.g., to study the specific chlorite or epidote texture (ROM1), or to study the mineral chemistry of scheelite that may occur as a trace mineral. Consequently, CT enables a more accurate interpretation of mineralogy, enhancing the understanding of scheelite ore genesis.

Mineral processing

Pre-concentration of tungsten ores typically involves the use of X-ray sorting, gravitational sorting, optical sorting, or hand-picking methods [196]. At Kara, scheelite is currently extracted as a by-product of magnetite, with scheelite being screened using handheld UV light devices. These conventional (mainly 2D) processing techniques rely on exposing scheelite to the ore surfaces for proper pre-concentration, potentially overlooking scheelite grains buried within the rock mass hindering complete recovery. In the CT data, scheelite exhibits the highest X-ray attenuation compared to other minerals in the ore. The application of CT for qualitative analysis to determine scheelite occurrence enables rapid data acquisition without the need for subsequent segmentation. In particular, CT could be employed for scheelite screening during comminution for process control and monitoring. Consequently, CT may contribute to a more efficient screening of ore and waste material at the Kara Fe-W mine.

Understanding the spatial distribution of ore and gangue minerals is also useful to achieve more efficient mineral processing of the mined ores. By obtaining information on particle size distribution, morphology, and occurrence before and after comminution using CT, the yield of the process could be quantified based on these properties analysed in situ. As scheelite is a brittle mineral, and particles smaller 20 μm (very fine as defined by Sivamohan et al. [197]) are difficult to recover [65], the spatial arrangement of scheelite should be considered in the choice of the comminution steps to preserve grain size and thus maximise recovery. Understanding the natural grain size of scheelite is crucial for anticipating potential losses during processing. For instance, if scheelite naturally occurs in sizes all under 20 μm, recovery becomes exceedingly difficult. Grain size information obtained with CT allows for the estimation of the proportion of scheelite of natural size likely to be lost to very fines. If scheelite is predominantly large in size, its size reduction during comminution (crushing and grinding steps) can be optimised to minimise losses in the processing circuit. This comprehensive understanding of recovery potential aids in optimising mineral recovery and achieving resource efficiency.

4.6 Conclusion

This study has provided novel mineralogical insights of the Kara Fe-W ore, Tasmania, Australia. The results indicate that scheelite is predominately spatially associated with hydrous silicates and occurs massive or disseminated with vein-fill mineralisation controlling a significant portion of its volume. CT proves effective in analysing the texture of scheelite ore in both 2D and 3D, further allowing for the examination of major, minor, and trace mineral phases with given grey value contrasts and particle sizes. CT falls short of offering detailed insights into mineral reactions and grain boundaries, especially of fine-grained particles and the quantification of similar X-ray attenuating phases (e.g., chlorite and epidote). A comparison with ICP-OES and XRD showed that CT is reliable for quantifying modal mineralogy and assessing WO_3 grade in individual ore samples. Integrating CT with conventional 2D techniques holds promise for enhancing our

understanding of the formation and mineralisation processes of Fe-W deposits. Furthermore, the insights provided by CT may inform the optimisation of scheelite extraction and separation techniques, thereby fostering more efficient resource recovery practices at the Kara mine.

- this page is intentionally left blank -

Chapter 5

General discussion

This discussion chapter begins by briefly outlining the rationale for optimising CT analysis for graphite and tungsten ore analysis. Subsequently, the thesis findings are reviewed and synthesised to address the main research question and evaluate the achievement of the main research aim. This is followed by a critical assessment of the advancements achieved in CT analysis of graphite and tungsten ores. Building upon these insights, implications for using CT in the raw materials sector and recommendations for future work are provided. A SWOT analysis of CT in ore characterisation is then presented. Finally, concluding remarks are presented.

5.1 Rationale for optimising CT analysis of graphite and tungsten ores

Over the past decades, extensive research has demonstrated the use of CT for ore characterisation, enabling non-destructive 3D analysis of mineral distributions and textures [e.g., 21, 30, 93]. However, CT's effectiveness is limited by several challenges, such as the dependence on grey value contrast for phase recognition [44], which is problematic for complex ores with varying X-ray attenuation properties [54]. Much research has been put into the process of CT data generation, aiming to optimise data acquisition and segmentation [26, 32, 35, 58, 95, 100, 106, 107]. Significant progress has been made for applying CT particularly to ores with very high-density target minerals such as gold and PGEs; in these ores, high X-ray attenuation contrast between target minerals and gangue allows for clear mineral differentiation and accurate quantitative analysis [26, 31, 32, 85, 89–91, 93]. This progress has established CT as an effective tool for such applications.

Despite these advances, the use of CT for CRM ores such as graphite and tungsten ores is still limited. To date, no research has been dedicated to a comprehensive CT-based mineralogical characterisation applied to these ores. Therefore, the full potential of CT analyses for graphite and tungsten ores has yet to be realised. Addressing these gaps requires optimising CT for tungsten and graphite ores. This optimisation involves the development of tailored acquisition and image processing protocols, demanding methods to enhance image quality and enable segmentation between minerals with similar X-ray attenuation properties. Such protocols could provide accurate qualitative and quantitative 3D data on these ores, ultimately expanding CT's capabilities and applications in ore analysis.

5.2 Review of research conducted

The main research question of this thesis was: *'How can CT be optimised for the characterisation of the critical raw materials graphite and tungsten in ores to obtain reliable qualitative and quantitative mineralogical information?'* The main research aim was: *'To investigate the potential of CT for the mineralogical characterisation of graphite and tungsten ores.'* This section first reflects on the main findings of the experimental work and evaluates the achievement of the key objective for each study. Subsequently, the study findings are synthesised to answer the main research question and to evaluate the achievement of the main research aim.

5.2.1 Article 1 - CT of graphite ore: developing an analysis protocol for mineralogical analysis

The key objective of Article 1 was to develop a CT analysis protocol for the mineralogical characterisation of graphite ore, representing a CRM ore with a low X-ray absorbting target mineral. The protocol developed included acquisition and image processing strategies, structured into ten iterative steps: 1) performing an a priori analysis (cf. Glossary, p. 107ff) for mineral identification and 2) calculating the theoretical attenuation coefficients (μ) of each mineral to facilitate 3) the selection of scan parameters. Following 4) the acquisition of projection data and 5) reconstruction, 6) grey value assignment was conducted using the information from steps one and two. The CT data then underwent 7) digital image filtering as a preparation for 8) segmentation, where a deep-learning algorithm provided by the image software was applied and further refined. Finally, 9) feature extraction was performed to establish quantitative information on flake size, flake size distribution, graphite content, and impurities, followed by 10) the validation of the generated data using OM.

Considering scanning parameter selection, it was found that a trade-off in kV settings (100 kV) was necessary to mitigate the varying X-ray attenuation properties of the phases present in the sample and maximising the contrast of graphite compared to the gangue minerals. While high spatial resolution was generally achieved, it was reduced at the sample's surface and bottom image slices due to the parallel alignment of the sample surfaces in relation to the X-ray beam, resulting in image blur. As expected, graphite showed partial grey value overlaps with adjacent silicates in the reconstructed CT data, rendering segmentation complex. However, it was found that the DL-based segmentation strategy applied successfully overcame this limitation, providing reliable quantitative data on flake size distribution, flake thickness and volume, along with the volumetric proportions of graphite, silicates and Fe-sulfides. Cross-validation using OM confirmed the accuracy of the quantitative data, demonstrating CT's added value. It is therefore concluded that the key objective has been achieved.

5.2.2 Article 2 - DECT of graphite ore: enhancing image contrast

In Article 2, the limited grey value contrast between graphite and adjacent silicate phases identified in Article 1 was addressed, together with the necessary trade-off in the choice of X-ray energy. Aiming to optimise the acquisition process, the key objective of the study was to investigate the effectiveness of high-resolution DECT for enhancing image contrast. By acquiring various low- and high-energy single energy CT (SECT) scans at high spatial resolution and fusing them with varying weighting factors using a python script, the optimum contribution of each energy level and spectrum were examined. This examination was achieved by collecting grey value

information from pre-defined material areas, identical in size and 3D coordinations on each reconstructed dataset. This grey value information was then used to quantify the image contrast in each MA using the CNR and Q-factor. Finally, the significance of the results was assessed performing a Least Significance Difference (LSD) Fisher test.

The results demonstrated that DECT significantly enhanced image contrast on graphite ore, suggesting that a proper distance between low and high kV settings as well as a certain X-ray energy level in the low energy range and must be applied to obtain the best results. However, similar to SECT, DECT relies on polychromatic X-ray radiation, meaning phases with almost identical attenuation properties (e.g., quartz and clay) remained impossible to distinguish as they shared the same grey values. Nevertheless, when a certain differences in grey values was available, DECT showed significantly enhanced contrast for each MA examined. While more data is needed for further validation, the outcome suggests that using DECT eliminates the need to select a trade-off in kV when analysing graphite ores further proving its effectiveness. It is therefore concluded that the key objective has been achieved.

5.2.3 Article 3 - CT of tungsten ore: case study on morphological characterisation and modal mineralogy

The key objective of this study was to use CT to examine the mineral texture, modal mineralogy, and WO_3 grade of scheelite ore from the Kara Fe-W deposit, representing a CRM ore with a highly X-ray attenuating target mineral and providing the first 3D characterisation of the scheelite ore from this deposit. The analytical protocol was based on the workflow developed in Article 1, with modifications made to account for the sample specific a priori analysis and scanning configuration. To mitigate scanning issues caused during data acquisition of sample ROM1, the image fusion method established in Article 2 was applied to reduce image noise. Additionally, to eliminate image blur on the CT slices at the top and bottom slices the sample surfaces as encountered in Article 1, the cylindrical shaped sample (ROM1) was mounted at a slight angle.

The results showed a significant improvement in spatial resolution on the sample surfaces of ROM1. In terms of image contrast, while the application of high kV successfully mitigated scanning artefacts caused by scheelite, the overall image contrast was limited, making it difficult to clearly discriminate between similarly attenuating minerals. This issue was particularly pronounced in phases with small grain sizes or lacking distinct shapes (e.g., pyrite and chalcopyrite, ROM4). While some of these minerals could be visually differentiated in the reconstructed CT dataset (e.g., bornite, pyrite and chalcopyrite, ROM4), segmentation of minerals within a specific paragenesis (anhydrous silicates, hydrous silicates, and sulfides) was not possible due to limited grey value contrast. This is an important finding, indicating that for successful DL-based segmentation a certain level of contrast is necessary to properly identify and ensure accurate manual labelling during ground-truth data generation. Regardless, the contrast obtained and DL-based segmentation still allowed for labelling minerals (scheelite, magnetite) and mineral groups (anhydrous silicates, hydrous silicates, and sulfides), even in the presence of grey value overlaps and the presence of artefacts introduced by beam hardening and irregular sample geometries (ROM4). Addressing these limitations proved significant, enabling the extraction of quantitative mineralogical information (e.g., modal mineralogy, scheelite grain size distribution, and WO_3 content) for the segmented phases, down to the ppm range. Furthermore, the analysis revealed critical textural relationships (e.g., structural features, spatial distribution of minerals and mineral associations). While some minerals could not be differentiated as well as the spatial resolution obtained did

not allow for detailed textural analysis (e.g., revealing replacement structures), the information obtained yielded new mineralogical insights on scheelite ore (3D textures, compositions and WO_3 grade) from the Kara Fe-W deposit, thereby informing ore formation processes and mineral processing aspects. Thus, it is concluded that the key objective has been achieved.

5.2.4 Answering the main research question and evaluating the achievement of the main research aim

Answering the main research question

Synthesising the research findings reviewed finally allows answering the main research question. The CT analysis protocol developed in Article 1 successfully generated high-quality CT data on graphite ore. A critical aspect this protocol involved identifying the phases comprising the sample and their individual X-ray attenuation properties. This step highlighted the need for conducting proper a priori analysis as CT cannot be used effectively without prior knowledge of the sample's properties. By calculating μ of the phases present in the samples, parameter selection and mineral identification in the CT datasets were facilitated. In terms of image processing, the DL-based segmentation strategies applied effectively managed image quality constraints related to artefacts and grey value overlaps between graphite and silicates, enabling the generation of accurate quantitative 3D mineralogical data.

The SECT data fusion method developed in Article 2 successfully addressed the image contrast limitations identified in Article 1, significantly improving the contrast in a graphite ore sample and thereby optimising the overall image quality of the data. This approach did not require any specialised hardware, suggesting ready integration into established protocols. In Article 3, the CT analysis protocol (Article 1) and the fusion method (Article 2) were used in a case study to characterise scheelite ore, demonstrating their applicability to another ore type. By considering the specific attenuation properties and necessary a priori analysis for scheelite ore, the protocol was successfully adapted. Furthermore, the image quality was optimised by (1) tilting the sample on the sample stage enhancing spatial resolution at the sample surfaces as well as by (2) applying the fusion method for the ROM1 sample, decreasing image noise.

The accurate mineralogical information obtained for both ores studied confirmed the validity of the strategies applied for tungsten and graphite ores. This validity further indicates that the iterative analysis protocol developed provides a robust foundation for reliable CT data generation across varying sample properties, with its individual steps being flexibly adjustable to the specific mineralogical properties of samples studied.

In summary, the synthesis findings demonstrate that optimisation of CT data successfully covered all key aspects necessary for effective CT analysis of graphite and tungsten ores. This encompassed the development of a dedicated CT analysis protocol (Article 1), the enhancement of grey value contrast of CT datasets (Article 2), and the use of advanced segmentation strategies (Article 1 and Article 3). These specific optimisation strategies improved image quality and successfully addressed segmentation challenges, leading to valid, high-quality qualitative and quantitative mineralogical information of graphite and tungsten ores. Although a limited number of samples was used, it was successfully demonstrated how CT can be optimised for these ores. Therefore, it can be concluded that the main research question has been successfully answered.

Evaluating the achievement of the main research aim

Optimising CT for graphite and tungsten enabled its appropriate use for the mineralogical characterisation of these ores. The studies demonstrated that CT is an effective tool for extracting a variety of mineralogical properties. For graphite ore, CT enabled flake size analysis, determination of flake size distribution, identification of impurities, and calculation of graphite volume. For tungsten ore, CT enabled the determination of tungsten grade, modal mineralogy, scheelite distribution and size. Furthermore, it revealed structural features such as veins, facilitating their identification. However, while the scope of Article 1 was on method development, with the specific aim to extract information on graphite properties, the study provided little information on the gangue mineralogy, as was examined in Article 3. Additionally, this work was restricted to a limited amount of graphite and tungsten ore types. Given the variability in mineralogical composition and texture across these ores, further targeted analysis of different graphite and tungsten ore varieties is necessary to capture CT's full potential for these ores.

In summary, while this research demonstrated the added value of CT for the mineralogical characterisation of graphite and tungsten ore, revealing significant potential, the full extent of this potential remains to be explored. Therefore, it is concluded that the main research aim has been partially achieved.

5.3 Critical assessment on the advancements in CT analysis of graphite and tungsten ores

Building upon the key factors that have contributed to the optimisation of CT data for graphite and tungsten ores, it is essential to contextualise these achievements within the broader landscape of CT-based ore analysis, assessing the research contributions to the field. Accordingly, the following subsections critically evaluate the acquisition and segmentation strategies employed and the results obtained, offering a deeper understanding of their strengths, limitations, and overall impact. In addition, practical aspects are discussed and the main contributions together with remaining challenges are highlighted at the end of the section.

5.3.1 Effectiveness of data acquisition

The primary contributors to image quality are image contrast and spatial resolution, determining the final image quality. Thus, the strategies used to optimise image contrast and spatial resolution for graphite and tungsten ores and their outcomes are evaluated and discussed below.

Image contrast

Following the experimental work, it has been shown that, while the set-up of most scanning parameters is primarily independent of the ores mineralogy, voltage is a crucial exception. The optimal kV setting is ore-type specific and must consider the sample's mineralogical composition. As kV directly controls X-ray energy, thereby influencing the X-ray attenuation, it significantly influences image contrast, essential for accurate mineral analysis. Therefore, in the following, the energy setup for graphite and tungsten ores is discussed. Best practices for optimising data acquisition for graphite and tungsten ore is provided in Appendix D.

Graphite ore In articles 1 and 2, the CT datasets showed that graphite generally exhibited low grey values owing to its X-ray attenuation properties. In the grey value histogram, graphite was positioned between air (lower grey values) and silicates (higher grey values, e.g., quartz, feldspar) without showing a distinct peak, indicating overlap in grey values with these phases. To enhance image contrast in CT, low kV settings are generally recommended [47], because of the energy dependence of X-ray attenuation [43]. Studies specifically addressing kV optimisation for graphite ores are limited. However, considering materials with similar attenuating target minerals, Wang and Miller [27] suggested the application of 60 kV for gypsum-bearing rocks. Regarding CT analysis of ores, Reyes et al. [118] showed for copper bearing ores that pyrite and chalcopyrite could visually differentiated at 50 kV and 80 kV, whereas Warlo et al. [115] found that at 160 kV, proper differentiation between these minerals was not possible despite their density differences (chalcopyrite = 4.19 g/cm^3, pyrite = 5.01 g/cm^3). These studies align with Godel et al. [85], who noted that phases are more challenging to distinguish at high beam energy.

In Article 1, the calculated μ values for graphite suggested that low kV settings would be beneficial for maximising image contrast, as the difference in μ values to the silicates is greatest. However, as the beam energy is limited by the intensity sufficiency of the transmitted X-rays [47], this means that in practice not all sample compositions allow the use of low X-ray energies, especially in the case of complex ores such as graphite ore. As observed during test measurements, low X-ray energies did not adequately penetrate high X-ray attenuating minerals (e.g., pyrite), resulting in artefacts that would have compromised subsequent quantitative analysis. Therefore, the presence of high X-ray absorbing minerals in graphite ore required a trade-off in the applied voltage (100 kV) to balance contrast with artefact reduction.

In addition to considering the attenuation properties for X-ray high absorbing phases, Article 2 emphasised that the attenuation properties of sample features such as pores, cracks, and voids (trapped air) must also be taken into account. These structures generally exhibited lower grey values compared to graphite, yet they were non-uniform causing partial grey value overlap with graphite despite their significantly lower X-ray attenuation than graphite. This non-uniformity in grey values of trapped air was likely a result of bright streak and scatter artefacts introduced by adjacent denser phases (e.g., HFO and hematite) (cf. Fig. 3.3). This phenomenon of beam hardening (streak artefacts and scattering artefacts) has been previously documented where bright and/or dark streaks emanated from high-attenuating phases into the surrounding X-ray absorbing material [26, 198, 199]. Bam et al. [100] reported that these artefacts intensify with increasing differences in attenuation contrast between the corresponding phases. Considering the high difference in attenuation properties between trapped air compared to HFO and hematite, this difference indicates that trapped air is highly affected by beam hardening with some grey values rendered brighter. Consequently this artefact induced grey value modification resulted in reduced local contrast between graphite and trapped air.

Unexpectedly, Article 2 revealed that the highest contrast between graphite and trapped air was achieved with high kV settings rather than low kV, suggesting a reduction in artefacts. However, while this artefact reduction was not clearly visible in the data, the enhanced contrast at high kV may further be explained by the chemical composition of graphite and air. Graphite and the main gases of air (nitrogen (Z=7) and oxygen (Z=8)) have very similar Z. At lower kV, the photoelectric effect, sensitive to Z, dominates X-ray attenuation. In contrast, at higher kV, Compton scattering, which is more sensitive to material density (graphite = 2.1 g/cm^3, air = 1.2 x 10^{-3} g/cm^3 at 20°C). This density difference thus becomes the dominant factor influencing X-ray attenuation, leading

to higher contrast at elevated kV settings. Regardless, further analysis is needed to clarify the relative contributions of these mechanisms.

The findings of Article 1 and Article 2 are significant demonstrating that while low kV settings are generally recommended between two phases to increase contrast [85], this may not always be true for graphite ores and likely other complex ores with similar X-ray absorption properties. As a result, selecting the most suitable X-ray energy for graphite ores must involve considering the overall mineralogical composition and structural features of the samples, rather than focusing on the target mineral only. This consideration further includes accounting for both Z_{eff} and the density of all constituents to determine the optimal kV settings (cf. Article 2). In this context, it is noteworthy that most studies have emphasised the role of density in assessing X-ray attenuation mechanisms and selecting appropriate X-ray energy, especially since CT has traditionally been used for metal ores [e.g., 21, 26, 29]. In contrast, the data obtained suggests different acquisition approaches for complex ores with low X-ray absorbing target minerals compared to metal ores.

Tungsten ore With graphite ore, the main challenge was to differentiate graphite from the silicate rich gangue and trapped air while reducing artefacts from high-density phases. The main issue with scheelite was to reduce beam hardening introduced by the mineral itself which is a very high X-ray absorbing mineral owing to its density and Z_{eff}. The general approach to reduce beam hardening in such ores is to increase the X-ray beam energy (kV), as higher kV settings reduce the differential absorption of X-rays within the sample [21]. However, while high kV settings reduce beam hardening, these simultaneously decrease image contrast as previously discussed.

Addressing this challenge, several strategies have been proposed to mitigate beam hardening without solely relying on kV adjustments. For instance, using beam hardening correction methods during image reconstruction [200, 201]. However, such methods are computational demanding and increase image noise in the reconstructed dataset [202]. Another common approach is using pre-filters to minimise low-energy X-rays from the polychromatic X-ray beam. However, while pre-filters reduce beam hardening [83] they require longer scan time [203] and reduce overall image contrast [203, 204], rendering them impractical for multi-mineral analysis.

Therefore, considering the analysis scope in Article 3, the most effective option to increase the number of identifiable minerals while addressing beam hardening was to further decrease the sample size, as suggested by Bam et al. [100]. Reducing sample thickness shortens the length of the X-ray path penetrating the sample, enhancing its penetration capacity [205]. This adjustment enabled a lower voltage setting of 150 kV for sample ROM1, compared to 180 kV for ROM4. However, even with reduced voltage, the X-ray intensity remained too high to clearly distinguish minerals with similar attenuation properties, particularly those within the same mineral group (e.g., oxides, sulfides, silicates). Thus, the reliance on high kV settings to counteract beam hardening caused by scheelite ultimately constrains the contrast achievable in scheelite ores, limiting the differentiation of similarly X-ray absorbing phases.

DECT Recognising the aforementioned ore properties related challenges in achieving suffient contrast in CT, numerous researchers have emphasised the need to enhance mineral differentiation by optimising image acquisition [e.g., 105, 106]. Studies using synchrotron CT equipped with X-ray sources that emit a monochromatic X-ray beam showed that it offered improved resolution by reducing artefacts and producing more uniform grey values [34, 108]. Despite these advantages, however, the high cost and limited accessibility of synchrotron facilities restrict its

wider application [206]. Moreover, the degree of contrast enhancement achieved with synchrotron CT has not been fully quantified, limiting a comprehensive evaluation of its potential for broader geological applications. Notably, many authors suggested DECT for enhancing image contrast in ore analysis [58, 115, 185]; however, dedicated research evaluating its effectiveness has remained sparse. As previously noted, the DECT method applied in this study offered a practical solution for enhancing contrast in graphite ore, facilitating clearer mineral differentiation without specialised hardware.

Beyond enhancing contrast, combining low and high energy datasets using DECT has offered another benefit: it simplifies parameter selection for graphite ore. In SECT, predicting ideal X-ray energy settings prior to measurement is challenging due to the variety of attenuation properties in graphite ores. Calculating μ of the phases within the ore as employed in this work provided a good starting point, but achieving optimal contrast ultimately required a series of trial scans, also due to the lack of existing protocols for graphite ore. While advanced methods exist to predict ideal kV settings before scanning [105, 207], determining optimal X-ray settings remains complex because of the polychromatic X-ray beam and the constantly changing X-ray spectrum in heterogeneous materials [21]. DECT, providing superior contrast for graphite ore regardless of the energy combination, eliminates both the need for finding a proper trade-off in kV settings and trial scans. Consequently, DECT supports usability and efficiency of data acquisition in graphite ores and those with low attenuating target minerals.

Another notable feature of DECT is its ability to improve image quality without compromising data fidelity, compared to frequently used digital filtering techniques that can potentially alter original image data and lead to information loss [176, 177]. Despite the need for extended acquisition time, approximately twice as long as SECT, DECT's capability to enhance contrast without the use of post-processing filters ensures that the integrity of the original data is preserved. This, in turn, results in more precise and reliable identification of minerals and structures, improving the accuracy of quantitative analysis.

Lastly, the method developed for determining image quality (cf. Article 2) introduces a valuable tool for CT image quality evaluation, as standard metrics are largely designed for homogeneous materials [170, 171]. By providing quantitative evidence of image quality of heterogenous ores, this approach increases the reliability of analysis results, supporting the improved use of CT applied to such materials.

Spatial resolution

Spatial resolution determines the size of the smallest feature that can be distinctly resolved in the CT image data [47]. While the use of a small focal spot size is a prerequisite, optimising spatial resolution in this work required adjusting sample size, as smaller samples do not only enable enhanced penetration capacity as mentioned before but also allow for higher scanning resolutions. As a result samples were prepared with dimensions of 10 - 15 mm in height and a maximum diameter of 15 mm. This setup enabled scanning resolutions between 5 µm and 8.4 µm voxel size, balancing sample representativity with analysis objectives. However, features close to voxel size were affected by the partial volume effect (PVE) (Glossary p. 107ff), resulting in blurred and unrealistic shapes. For example, Article 1 showed that even at a voxel size of 5 µm, only shapes of graphite flakes larger than ~25 µm could be clearly recognised, though phase boundaries remained blurred. This blurred image data (mixed grey value information) shows that minerals range in grey values and overlap with others. Such overlap can impact the accuracy of

the quantitative analysis, potentially leading to over- or underestimations, especially of features close to voxel size [83]. This limitation further demonstrates that a voxel size must be used which is significantly smaller than the feature of interest to capture its actual morphology, as also noted by Withers et al. [44], and underscores the importance of careful sample preparation to achieve analysis goals.

Attempts to mitigate the impact of the PVE have included using larger detectors to improve spatial resolution; however, these adjustments significantly increase acquisition times, introduce image noise and result in larger data volumes [208], which in turn significantly increase data processing time. Similarly, scanning regions of interest within samples [209] introduces additional artefacts [50], particularly in heterogeneous materials [200]. Regardless, as the PVE cannot be fully eliminated, this inherent limitation demonstrates that CT cannot provide detailed textural information as established techniques using OM and SEM-EDS, emphasising the reliance on complementary techniques for comprehensive mineralogical analysis.

While adjusting sample size allowed for achieving spatial resolution close to the resolution limits of CT, it was found that sample orientation during scanning is also crucial to address the spatial resolution limitations introduced by artefacts. In Article 1, the cylindrical sample (polished section) was positioned horizontally, with the sample surface on top, which is standard practise [210], to leverage the benefits of its geometry (uniform X-ray path lengths at all projection angles). This orientation, however, resulted in blurred image data at the topmost and bottommost image slices. This compromised data quality can be attributed to the fact that surfaces that are oriented parallel to the X-ray beam are not properly penetrated [211], producing blurred image data and non-uniform greyscale gradient of the slices near the sample surface.

To address this issue, Warlo et al. [115] have attached two cylindrical-shaped polished sections and scanned them jointly with the polished surfaces in contact with one another. They found, while this approach effectively reduced the pronounced artefacts, the presence of dense minerals on the sample surfaces caused new artefacts in adjacent areas. Furthermore, this approach inevitably increase the field of view (FOV) considering an increased sample size, which in turn lowers the scanning resolution.

In Article 2 and Article 3 the samples were slightly tilted to minimise parallel surfaces to the X-ray beam. The results showed that orientation-related artefacts were significantly minimised Fig. D.1, aligning with Villarraga et al. [212], who found that tilting improved edge sharpness for rectangular workpieces in dimensional metrology. Notably, the impact of sample tilt on the cone-beam artefact was minimal. Consequently, this optimised orientation enhanced spatial resolution on the topmost slice, facilitating phase identification and validation through OM and SEM-EDS. This is significant as enhanced resolution on the topmost slice offers a more representative analysis of the entire volume, supporting the calibration of CT data with conventional 2D methods and could potentially serve as a ground truth for deep learning algorithms, enhancing quantitative analysis.

5.3.2 Effectiveness of deep learning-based segmentation

While CT data acquisition required careful optimisation of parameter selection to enhance mineral specific attenuation differences and recognition textures, segmentation primarily focuses on processing the acquired image data. However, the inherent attenuation properties of minerals, represented by their respective grey values, affect the success and accuracy on the chosen segmentation method [27]. Thus, selecting the appropriate method is key to obtaining accurate

quantitative mineral information.

Conventional methods, such as thresholding and watershed segmentation, have been effective for minerals with significant grey value contrasts [35, 58, 93]. These methods produce results fast and straightforward to apply. However, conventional segmentation depend on clear grey value differences to separate phases [35] and this dependency introduces a high potential for human error, especially in complex ores containing minerals with similar grey values, overlaps, or gradual transitions between phases [27]. This limitation also poses challenges for multi-mineral analysis [54, 115, 118]. For example, Warlo et al. [115] found that watershed segmentation yielded inaccurate results when phases had similar or overlapping grey values and noted that beam hardening introduced by high X-ray absorbing minerals further compromised accuracy of the segmentation outcomes. Similarly, Reyes et al. [118] reported that threshold-based segmentation struggled to differentiate phases with similar X-ray absorbing phases in copper-bearing ores. While several machine learning (ML)-based methods (e.g., random forest, *K*-means clustering) have generally shown improved performance over conventional methods (e.g., in delineating grain boundaries [116, 119]), the presence of scanning artefacts and overlaps in grey values still limit the segmentation result [116, 119]. These limitations restrict the effectiveness of conventional and the stated ML-based segmentation methods for complex ores and multi-mineral analysis, in which grey value overlaps and artefacts are common.

However, the experimental work of this thesis demonstrated that DL-based segmentation successfully addressed these challenges. For graphite ore, the applied DL-based approach accurately distinguished between graphite and silicate minerals, despite their similar attenuation properties, resulting in similar grey values overlap and the presence of artefacts introduced by highly X-ray absorbing Fe-phases (cf. Article 1). This advancement is significant because graphite ores typically contain silicate minerals [213], along with cracks and voids from alteration processes [214], all of which exhibit similar, partially overlapping grey values to graphite, complicating grey value-based segmentation. Instead, DL-based segmentation has overcome these limitations, enabling accurate quantitative analysis and offering a reliable method for segmenting and analysing graphite ores. This approach also shows promise for performing quantiative analysis to other complex ores with similar compositions and low grey value contrasts. Similarly, for tungsten ore, where conventional segmentation showed inaccurate results due to beam hardening and limited phase contrast [115], DL-based segmentation applied in Article 3 proved effective. Despite the heterogenous mineralogy comprising phases exhibiting similar X-ray attenuation properties and those leading to beam hardening (e.g., scheelite), the findings demonstrated accurate segmentation of multiple classes allowing for a comprehensive mineralogical and textural characterisation in 3D. Enabling multi-mineral segmentation by DL-based segmenation is significant as this advancement broadens the applications of CT in ore analysis.

The results from Article 3 suggest an additional benefit of DL-based segmentation which is the ability to mitigate geometry-related artefacts (e.g., cone beam artefact, cupping effect), thereby handling irregular sample geometries without impacting the final analysis outcome. According to the existing literature, the ideal sample geometry is cylindrical [26] as this shape provides uniform X-ray penetration due to the consistent path length at every angle. This uniformity results in a more even grey value distribution from the sample rim to the center (e.g., cupping effect) and reduces the cone beam artefact. Accordingly, cylindrical samples have been widely adopted for their effectiveness in reducing geometry related artefacts, enhancing segmentation accuracy [83]; traditional grey value-based segmentation depends on cylindrical sample shapes

or subvolume creation to mitigate these artefacts [115]. However, the results obtained in Article 3 suggest that DL-based segmentation eliminates the need for these specific sample geometries and creating subvolume, thus saving time in sample preparation and maximising the examinable sample volume. This is significant as maximising the examinable sample volume, thereby enhancing representativeness, is a critical factor in high-resolution scans that typically require smaller sample sizes.

Despite these advances, this study also revealed limitations of DL-based segmentation. The findings are based on a limited number of graphite and scheelite ore samples. Further analysis of diverse types of these ores is necessary to validate the generalisability of these results. Moreover, the training process is time-consuming and computationally demanding (cf. Section 5.3.3). Manual labelling is required to provide ground truth data, introducing potential human error [215], especially when segmenting visually ambiguous phases. However, given combination of inference stage (cf. Glossary, p. 107ff) and training stage DL-based segmentation significantly reduces human bias compared to conventional segmentation, which in turn improves the reliability of the outcome [216].

In addition, DL-based segmentation struggles to label phases with almost identical X-ray attenuation properties (e.g., quartz (μ = 0.37), and K-feldspar (μ = 0.36) in ROM1, Article 3). While these phases could be visually distinguished, accurate segmentation was not possible, showing the need for a minimum level of contrast and spatial resolution necessary. This requirement emphasises that the effectiveness of DL-based segmentation is inherently tied to the quality of the acquired CT data. As a result, sample heterogeneity and the specific mineralogical composition will continue to pose challenges in CT. Thus, despite the aforementioned advances, CT, even when combined with DL-based segmentation, cannot match the accuracy in modal mineralogy analysis achieved by conventional 2D tools such as AMICS.

Regardless, the results of this work demonstrated that DL-based segmentation currently offers the highest accuracy compared to traditional segmentation, especially in dealing with grey value overlaps in the CT image data and when performing multi-phase analysis. In this context, the limitations of traditional segmentation techniques could explain the predominant application of CT in quantitative analysis of gold and PGE ores, mostly been restricted to segmenting the high-contrast target mineral(s) from the low-contrast gangue material(s) only, rather than performing multi-phase analysis. In contrast, DL-based segmentation allows for multi-phase analysis, thereby expanding the capabilities of CT applications to more complex ore systems.

5.3.3 Practical aspects: time, cost and ease-of-use

While the previous subsections evaluated the strategies applied for data generation and their outcomes, it is important to discuss the strategies' impact on practical aspects. Accordingly, the following subsections elaborate on time, ease-of-use, and cost factors.

Time and cost

The time required for generating CT data varies significantly depending on the specific goals of the analysis as well as the ores properties. Simple visualisations of samples with highly contrasting μ materials can be obtained in less than two hours if image noise and segmentation are not critical concerns [217]. However, analysing complex ores, like the ones examined, necessitates optimal image quality, involving long acquisition times (up to 14 h in this work). While the CT-projection

recording process itself is automated, refining scanning parameters may require initial test runs.

The time investment for segmentation varies significantly depending on the chosen method [218]. Threshold and watershed segmentation can be completed within minutes [218–220]. In contrast, DL-based segmentation necessitates algorithm training, which can take hours depending on model selection, parameters, dataset complexity, and computing power as shown in this work. While the actual training process itself is unsupervised, DL-based segmentation demands significant operator involvement during inference stage, which can also span several hours. Thus, for complex ores, the entire segmentation and feature extraction process may be extended to days. Consequently, based on the findings, the whole CT processing chain, including a priori analysis, may take up to two working weeks for the experienced user.

Considering the potential long acquisition and processing time, quantitative CT data is expensive compared to traditional methods such as OM, SEM-EDS and AMICS, which has particularly consequences for industrial applications (cf. Section 5.4.1). For example, while AMICS is also expensive, the analysis proceeds automatically after following the generation of a sample specific database [18, 221].

Ease-of-use

As the previously shown, CT is not a standardised and automatised technique, requiring user experience. While standardised CT protocols are available in research areas with constant analysis goals and sample material, such as in petroleum geology using CT to determine size, distribution and connectivity of pores [222], standardising protocols for ore analysis is challenging due to the specific properties of ores, unique for each type. However, the protocols developed and the CT-specific information generated for graphite and tungsten ores in this work can assist in the effective application of CT to these ores, simplyfing its use. In addition, these protocols may be applicable to other ores with similar attenuation properties, thereby contributing to the broader application of CT in ore analysis. The main factors influencing ease of use, along with ways to facilitate analysis, are summarised below.

- *Acquistion:* The acquisition process, while theoretically unique for each ore, follows some basic rules that have been elaborated in Appendix D.
- *Segmentation:* The complexity of segmentation varies depending on the chosen technique. Simple methods such as thresholding require minimal user training, while DL-based segmentation demands some theoretical understanding of machine learning. However, the use of pre-trained CNNs in the software used makes DL-based segmentation accessible, requiring primarily proficiency with the software itself, which can be gained through free and open-source tutorials. This also applies to subsequent feature extraction. Recommendations for proper DL-based segmentation are compiled in Appendix D.
- *Mineralogical knowledge:* Accurate mineral identification in CT images necessitates a comprehensive understanding of mineralogy and proper knowledge conventional analysis methods such as OM to obtain a priori information. This expertise is imperative as it finally enables researchers to interpret CT data effectively and draw meaningful conclusions about ore composition and properties.

5.3.4 Highlighting main contributions and remaining challenges

This assessment has highlighted several contributions that broaden the knowledge base in CT-based ore analysis and support its continued development in this field:

- *Advancing understanding of X-ray energy settings and attenuation behaviour of graphite and tungsten ores:* This work advanced the understanding of parameter selection for both graphite and tungsten ores, providing critical insights into their attenuation behaviour. For tungsten ores, CT can differentiate between scheelite and other mineral groups (e.g., Fe-sulfides, Fe-oxides, silicates) but cannot distinguish between minerals with very similar X-ray absorption properties (e.g., epidote and chlorite) due to the necessity of using high kV settings. This observation aligns with other studies, highlighting a general limitation of CT when applied to complex ores with high X-ray absorbing target minerals, which limits detailed multi-mineral analysis. In contrast, for graphite ores, the target mineral, graphite, does not solely determine the X-ray energy setting, requiring a trade-off to mitigate the varying attenuation properties of the ores constituents. These insights gained fill a critical cap in CT applied to ores with low-attenuating target minerals.
- *Enhancing image quality through advanced acquisition strategies:* While DECT does not overcome CT's limitation in identifying minerals with nearly identical attenuation coefficients, it offers a practical tool for enhancing image contrast in complex ores with low X-ray attenuation minerals, such as graphite. Tilting the sample significantly enhanced spatial resolution at the sample surfaces, aiding in calibration of CT data with 2D imaging methods. Together, these strategies advance image quality, supporting subsequent segmentation capabilities and thus strengthening the analytical outcome.
- *Advancing quantitative analysis through DL-based segmentation:* Implementing DL-based segmentation significantly improved the effectiveness of quantitative analysis. While time-consuming and still dependent on proper image quality, restricting detailed compositional and textural analysis, this method proved effective in overcoming challenges related to grey value overlap and imaging artefacts. This advancement represents a significant step forward in CT, advancing CT's analytical capabilities to more complex ores.
- *Enhancing understanding of ore properties through the CT data:* Establishing 3D data of graphite and tungsten ores offers an additional layer of information, contributing to a better understanding of their mineralogical characteristics.
- *Broadening CT applications through developed analysis protocols:* While CT requires significant user expertise, the developed strategies not only aid in analysing graphite and tungsten ores but offer adoption to other complex CRM ores, broadening CT's applications.

5.4 Implications for the raw materials sector

The insights gained from the experimental work and this discussion chapter have several implications for the raw materials sector. In the following, implications of using CT in geometallurgical programs (industry) and ore deposit research (academia) are discussed.

5.4.1 Geometallurgy

The core concept of geometallurgy lies in maximising mining efficiency and profitability by understanding the complex interplay between ore characteristics, their spatial variability, and their impact on operational performance [223–225]. Achieving this understanding requires a robust foundation of cross-validated and calibrated analytical methods to ensure accurate characterisation and prediction of ore properties throughout the mining value chain [226]. In fact, mineralogical and textural information are much more decisive to the modelling of processing operations than bulk geochemical data [227]. Thus, integrating CT into geometallurgical programs holds immense potential for enhancing the understanding of ore characteristics and their impact on process performance.

Theoretical considerations

By leveraging 3D information provided by CT, researchers and engineers could develop more accurate prediction models, optimise processing parameters and ultimately achieve more efficient, sustainable, and profitable mining operations, for example:

Ore body modelling and resource estimation Proper ore body modelling requires detailed sample data on textural features such as shape, size and liberation rather than focusing solely on ore grade given that mineral textures determine the recovery potential [16]. In tungsten deposits, e.g., the accurate identification and quantification of scheelite grain sizes is crucial for determining economic viability, considering grains smaller than 20 μm cannot be recovered, regardless of the overall ore grade [65]. Traditional 2D analysis can suffer from limited sample representativity and stereological bias, potentially misrepresenting the true grain size distribution [54]. In contrast, CT enables precise measurement of grain sizes within intact ore samples, as shown by this research, offering a more accurate and representative assessment of the proportion of recoverable scheelite. This 3D approach eliminates stereological errors inherent in 2D methods [155, 156], providing a more reliable evaluation of ores' variability and the deposit's economic potential. Consequently, CT could enable targeted exploration and mining strategies that focus on areas with higher proportions of recoverable scheelite.

Mineral processing CT could enable tailored grinding strategies that maximise liberation while minimising energy consumption, a major factor in mining contributing 4% of the global energy share [228]. By comparing pre- and post-comminution scans, CT could enable quantification of grinding efficiency and identification of suboptimal liberation. For commodities like graphite, where flake size directly influences the market value [137], CT's ability to determine the true flake size distribution within the ore could enable quantification of the potential yield. Moreover, its capacity to measure flake thickness (cf. Article 1) could provide a key parameter for breakage modelling, further enhancing the optimisation of comminution circuits. Similarly, for tungsten ores, CT could help optimise comminution by liberating scheelite grains without excessive overgrinding, which leads to losses of fine-grained material. Additionally, an important challenge in mineral processing is accurately characterising particle shape, as mineral particles are often irregular and difficult to define from 2D cross-sections obtained by OM or SEM-EDS [20, 229]. CT's ability to quantify textural features (cf. Articles 1 and 3), including particle shape [230], provides more accurate particle data than conventional methods. This information could support the optimisation of separation efficiency and grinding processes, improving recovery rates [231].

Practical considerations

The effectiveness and practicality of implementing CT in geometallurgical programs, however, are highly dependent on the specific characteristics of the ore deposits, as these factors ultimately control time, cost, quality of information, and ease of use of CT analysis, as evidenced by this work. In scenarios with homogeneous ore bodies and simple ore mineralogy (significant X-ray attenuation contrast between target minerals and gangue), and simple geological structures, CT can excel. While 2D techniques typically require multiple 2D sections to mitigate stereological bias, increasing overall sampling requirements, CT may provide robust 3D data for accurate characterisation, resource modelling and process performance monitoring with fewer samples, making it a viable option in geometallurgical programs.

Conversely, in more realistic scenarios, heterogeneous ore bodies comprising ores with varying mineralogical composition and textures pose a challenge. Accurate resource estimation and modelling necessitate the analysis of a larger number of samples to capture ore variability (e.g., spatial distribution of minerals and textural features) [227]. Furthermore, constant sampling may be required within an existing operation for assessing processing performance [181]. For complex ores such as graphite and tungsten ore, requiring extensive DL-based segmentation, analysis of a single sample can take several days. This extended analysis time, when multiplied across a large sample set, can lead to prohibitive costs and delays.

Instead, SEM-based automated image analysis is significantly faster and more cost-effective for large sample sets [18, 221]. Additionally, CT's resolution limitations for distinguishing phases with similar X-ray absorption characteristics may not always provide the desired level of detail, whereas SEM offers significantly higher resolutions [18, 221]. Therefore, as long as conventional methods remain more accurate and practical for ore characterisation, the widespread adoption of CT in large-scale geometallurgical programs and deposits consisting of multiple geometallurgical domains is limited. This practical limitation is further evidenced by recent CT research, which remains focused on method development, examining individual samples rather than applying large-scale case studies [101, 116, 117, 232–234].

Regardless, in its current state, CT can be used to guide sampling strategies for geometallurgical testing during exploration, such as with already available benchtop CTs combined with μXRF establishing borehole data within tens of minutes [235, 236]. Despite a limited spatial resolution (200 μm voxel size), these scanners can rapidly reveal mineral assemblages, alteration zones, and structural features (e.g., shear bands, fold hinges) within drill cores [33, 237, 238]. Given the challenge of traditional sampling, which depends on surface-level analysis, potentially missing key subsurface features [85], scanned drill cores can reduce the reliance on chance in sample selection, aiding in more targeted and representative sampling of the ore body for downstream analysis using established mineralogical methods. Additionally, the ability to generate continuous 3D borehole data is especially effective for identifying and interpreting local and regional geological structures [238]. This readily accessible 3D data can then be used to refine geological models, supporting informed and dynamic decision-making in mine planning. Notably, scanned drill cores and samples can be stored digitally for future reporting or re-analysis as needed, preventing potential alteration reactions caused by weathering.

5.4.2 Ore deposit research

In academia, time constraints are less critical than in industrial applications. Users often have the expertise to conduct complex and thorough analyses, allowing them to optimise CT for each specific application. These factors minimise the aforementioned operational constraints that hinder the use of CT in large-scale geometallurgical applications.

As demonstrated by previous studies and this research, CT can contribute to the understanding of ore-forming processes [26, 30, 239]. By examining 3D distributions of minerals and quantifying the textural properties of target minerals, CT can offer valuable insights into these processes. For example, Article 1 showed that CT was effective in determining the size and spatial distribution of graphite flakes within an intact sample. Knowledge on these properties is crucial as they provide evidence for graphite formation [14]. For example, for flake type graphite ore, flake size increases with the degree of metamorphism [240]. Similarly, both metamorphic grade and deformation play a significant role in influencing the resulting flake size distribution (e.g., clustered or disseminated) within the deposit [241, 242]. Analysing flake size in graphite ores is usually done by sieving which requires crushing the samples [14, 130]. Similarly, information on spatial flake size distribution is usually obtained using cross-sectional 2D imaging methods that may be subject to the stereological error. By analysing a 3D volume and determining the true flake size and its distribution within the ore matrix as demonstrated in this work, CT can help to reconstruct the depositional environment of graphite deposits more precisely [46].

While DL-based segmentation has now enabled compositional analysis (cf. Article 3) CT still lacks the ability to reveal detailed modal mineralogy due to inherent challenges such as insufficient attenuation contrast and limited spatial resolution. These limitations also restrict detailed assessments of mineral reactions and overprinting textures (cf. Article 3). Therefore, it is suggested that the most effective use of CT in ore deposit research is achieved by integrating qualitative and quantitative CT data with other mineralogical, and geochemical analyses. By using a synergistic approach that combines the strengths of each method, the analytical outcome can be enhanced. CT's 3D imaging capabilities reveal patterns and structures within the ore that might not be apparent in 2D thin section analysis, as seen in Article 3, where CT facilitated the identification of structurally controlled scheelite mineralisation. Combining 2D with 3D data can then provide resolution needed for revealing and interpreting fine-scale textural features on grain boundaries such as mineral reactions and overprinting textures. Consequently, a multi-dimensional, multi-scale approach, as also noted by [243], incorporating CT as an additional layer of information, provides a more holistic understanding of ore deposits.

Recent studies have successfully demonstrated the integration of this advanced approach [244–247]. Notably, these studies included CT as a standard technique in their methodological toolkit, rather than positioning it as the primary focus of investigation. This usage indicates the maturation of CT and its increasing value in scientific research. Since CT becomes more accessible and accepted within the scientific community, it is likely to evolve into a routinely used tool in future. This growing adoption could lead to new discoveries in ore deposit formation and refinement of exploration strategies.

5.5 Future work

Based on findings from the experimental work and previous discussion, several recommendations for future work can be made. In addition, considering the current technological advancements in

AI, a concise outlook on these developments in relation to CT is provided, along with suggestions for their potential adoption in the context of ore characterisation.

5.5.1 Recommendations for future work related to the experimental work

- *Assessing time-accuracy trade-offs:* This thesis prioritised high data accuracy, potentially leading to longer acquisition and processing times. Future research should investigate the trade-off between analysis time and result accuracy for both CT-data acquisition and image processing, aiming to identify parameters that balance data quality with practical constraints. This refinement would facilitate the development of more efficient and cost-effective CT workflows.
  - *Acquisition time vs. image contrast:* Researchers should explore the relationship between acquisition time and the resulting image contrast, determining the minimum acquisition time required to achieve sufficient contrast for visual phase discrimination and accurate segmentation. The image quality measure developed in this thesis could serve as a valuable tool for objectively comparing datasets obtained at different acquisition settings. This approach would enable optimising acquisition parameters to minimise time and cost while maintaining data quality.
  - *Image filtering vs acquisition time:* Image filtering can be a valuable tool for CT-image quality enhancement, as demonstrated in this work where it successfully decreased noise while increasing sharpness. On the other hand, if not used carefully, filters might compromise segmentation accuracy, as they can also introduce blur and diminish subtle details crucial for proper segmentation. Considering the image processing software used, future research should assess the efficacy of different filters in terms of further optimising noise and image sharpness. Given digital filters ability for noise reduction they may allow for shortening acquisition time. Therefore, research should investigate the extent to which digital filters can compensate for reduced photon data (from shorter scan times) without sacrificing the level of detail necessary for accurate visualisation and segmentation.
  - *Segmentation time vs. accuracy:* Future studies should focus on finding the optimal balance between the amount of ground-truth input data required for training deep learning models and the resulting segmentation accuracy considering analysis efficiency. Using established 2D-based analysis as a reference for accuracy, researchers can determine the minimum amount of training data needed to achieve comparable results. Furthermore, for ores with simpler mineralogy, the time-intensive deep learning approach may not always be necessary. Therefore, researchers should systematically evaluate the efficiency of different segmentation techniques across a variety of ore types and identify sample-specific criteria (e.g., attenuation contrast, mineral complexity) to guide the selection of the most appropriate technique for a given scenario.
- *Further validation of DECT:* The results of Article 2 demonstrated that DECT significantly enhanced image contrast, ultimately improving image contrast. To further evaluate the mechanisms contributing to the superior image quality (photon count and X-ray energy composition), future studies could, e.g., compare DECT scans with SECT datasets having

double acquisition time.

- *Analysis of further graphite and tungsten ore types:* Given the research presented based on a limited number of samples, further investigations concerning data acquisition and DL segmentation are required to validate the research findings. In addition, given the variability of graphite and tungsten deposits different types should be examined for gaining a deeper understanding on how to apply CT on these materials, ultimately leading to more robust characterisation protocols.
- *Analysis of further CRMs:* Similar to the aspect above, future research should focus on exploring the applicability of CT for the study of other CMRs. This will help to better understand both, the limitations and benefits of CT when applied to these types of ores.
- *Literature review:* Existing reviews on CT in the context of ore analysis lack in evaluating the method's potential in light of recent AI developments. Given the transformative impact of AI on various domains, it is essential to update these reviews to reflect the new possibilities for CT applications in the geosciences while acknowledging its limitations. Past reviews have often emphasised segmentation as a major limitation of CT with conventional segmentation methods constraining multi-phase analysis. However, this perspective is now outdated due to the advancements in DL-based segmentation which, for example, enables the multi-phase analysis of complex ores, as demonstrated in this research. Additionally, these reviews should also consider the broader potential of AI beyond segmentation. It is noteworthy that the principal factor for accurate and effective CT analysis is the image quality of the reconstructed CT data set. Thus, enhancing reconstruction will also play a crucial role in advancing CT based analysis. Consequently, a comprehensive review that incorporates these advancements is required to reassess the state-of-the-art CT and to guide future research and applications, while also allowing operators for evaluating a potential usage of CT.

5.5.2 Outlook on current and future developments of CT

In light of recent developments in AI, it can be posited that the next evolutionary step for CT lies in leveraging AI. The application of AI across the entire CT-data processing chain, from data acquisition to segmentation, offers significant potential to enhance resolution, analysis, and throughput while reducing analytical time. This advancement promises to increase cost-time efficiency and reduce reliance on specialised expertise, propelling CT beyond its current state-of-the-art. While a comprehensive exploration of AI's impact on CT is beyond the scope of this study, the following bullet points provide a brief overview on some recent developments of AI-based CT data acquisition and processing as well as recommendations for future work. Interested readers can find further details on current AI developments in CT [248, 249].

- *Image reconstruction:* Conventional FBP reconstruction algorithms are prone to image noise and other artefacts, thereby requiring longer acquisition times for achieving high-scan quality. Research on AI based reconstruction has just commenced with initial results already promising showing increasement in CNR and spatial resolution [250–253], yet they require high computational power. Future work can therefore be suggested to decrease computational complexity, e.g., via parallelisation paralellisation (cf. Glossary p. 107ff) and dedicated hardware acceleration.
- *Image filtering:* AI-based image filtering has already demonstrated to be more effective than traditional filtering; its applicability, however, is constrained to narrow inspection tasks and

materials other than rocks and ores [254–256]. Thus, future research should concentrate on rocks and ores with the objective of establishing more general algorithms that can be fine-tuned to the specific ore(s) to be analysed. Similar, to AI-based image reconstruction, AI-based filtering will further decrease acquisition time.

- *Segmentation:* Similar, DL-based segmentation has already significantly advanced multi-phase mineral characterisation as this research has demonstrated, emphasising its potential. However, current DL-based segmentation can be time intensive, and involve manual labelling, thus a potential operator bias. Future research should therefore focus on finding alterative solutions to manual labelling. This may be achieved through the mineral information obtained from other techniques such as μXRF or AMICS providing robust ground truth data, enhancing method robustness.

The ultimate goal following this AI integration is achieving automated analysis comparable to established 2D techniques like AMICS. This necessitates fully calibrated CT systems [257], achieved through mineral libraries with standardised minerals and known absorption properties [253]. These libraries would serve as references, enabling predictive models for X-ray absorption under various scanning and sample conditions. As a result, grey values in CT images could be directly linked to specific minerals, facilitating automated mineral identification and quantification. Data extraction could then occur directly after reconstruction, eliminating the need for segmentation, minimising user input error, and maximising the robustness and reliability of the method for standardised quantitative 3D analysis.

5.6 SWOT analysis of CT in ore characterisation

Based on the previous discussion, a SWOT analysis has been conducted to summarise the strengths, weaknesses, opportunities, and threats related to the application of CT in ore characterisation, as demonstrated by the ores studied (Table 5.1).

CT offers significant value in ore characterisation when used in conjunction with state-of-the-art 2D methods, given its ability to unique qualitative and quantitative 3D information as demonstrated by previous and this research. However, to extend CT's impact beyond scientific applications, it is imperative to address its current limitations (Table 5.1). With regard to geometallurgical programs, these limitations hinder cost-effective workflows necessary for economically viable throughput, recovery, and thus the effective management of capital expenditures (CAPEX) and operating expenses (OPEX). Therefore, considering potential users in the industry in the near future, CT in its current state does not offer adoption by operators, but rather by geological service providers seeking to enhance their analytical portfolio and capabilities. Streamlining workflows and developing tools for automatisation are key steps towards realising CT's widespread adoption in the mining industry.

Table 5.1: SWOT analysis illustrating the strengths, weaknesses, opportunities, and threats of current CT in ore characterisation, as identified in this work.

Strength	Weaknesses
• *Non-destructive 3D imaging:* Provides detailed 3D visualisation of external and internal ore characteristics without the need for physical sectioning. • *Eliminates stereological error:* Provides true 3D information, avoiding the biases inherent in 2D sections. • *Quantitative mineralogical and textural analysis:* Enables quantification of modal mineralogy, mineral abundances, grain size distributions, associations, etc. • *Increased sample representativeness:* Enables analyses of a larger sample volume compared to 2D sections • *Applicable to diverse ore types:* Suitable for various ores, including complex and heterogeneous samples. • *Digital preservation of samples:* Digitally stored samples are protected from weathering processes and do not require physical storage space.	• *Costs:* High initial investment and ongoing maintenance expenses; high analysis costs. • *Ease-of-use:* Proper data acquisition, processing, and interpretation require trained personnel, particularly for quantitative analysis. • *Time investment:* Depending on the analysis task(s) and ore(s) to be examined, generating CT data may require significant time. • *No spectral information:* Minerals with similar attenuation characteristics may be indistinguishable, limiting their differentiation ability • *Indirect mineral identification:* Mineral identification and corresponding grey-value assignment necessitates prior knowledge on the sample's mineralogy. • *Resolution and sample size limitations:* High-resolution CT analysis is constrained by limited sample-size and spatial resolution, affecting proper visualisation of features close to detection limit. • *High computational and storage requirements:* Generating CT data requires powerful workstations and substantial storage capacity due to large output sizes.
Opportunities	**Threats**
• *Ore deposit research:* 3D analysis can aid in interpretation of ore mineralogy and texture, ultimately contributing to a deeper understanding of ore deposits • *Geometallurgical programs:* Quantitative true 3D data on ore textures can provide valuable insights for optimising ore body modelling, comminution, separation, and extraction processes, enhancing recovery rates. • *Ore deposit modelling:* 3D characterisation can aid in resource estimation and mine planning. • *Multi-dimensional analysis:* Integrating 3D CT data with methods like XRF or SEM offers a more holistic understanding of ore properties, enhancing decision-making across the mining value chain. • *Technological advancements and efficiency:* Continued development of AI-based algorithms, automation, and streamlined workflows can greatly improve the speed, accuracy, and robustness of CT-based ore characterisation, making it more efficient and cost-effective for research and industry, ultimately reducing barrier to adoption.	• *Sample complexity impacts efficiency:* Ores comprising phases with similar X-ray attenuation properties may prolong analysis time and limit the information extracted, hindering efficient workflows. • *Limited automation and standardisation:* The current lack of calibrated CT systems and standardised workflows impedes achieving fully automated analysis, requiring significant operator input and expertise. • *Reproducibility concerns:* The accuracy of CT analysis can be influenced by operator decisions, potentially leading to inconsistencies in results. • *Dominance of established techniques:* 2D automated mineralogy tools are more robust, reliable and straightforward to apply. • *Cost-benefit considerations:* The high cost of CT analysis and time spent and may be a barrier to adoption for the industry, particularly for smaller companies.

5.7 Concluding remarks

The discussion chapter has demonstrated that CT is a promising analysis tool for characterising graphite and tungsten ore. Developing and implementing optimised acquisition and image processing protocols allowed for the generation of valid and accurate quantitative CT data. Thus, the results of the experimental work obtained underscore the utility of this technique for aiding in understanding the mineralogy and texture of these ores through the generation of true 3D information. Notably, applying DL-based segmentation strategies enabled the establishment of modal mineralogy, even in the presence of overlapping grey values and image artefacts in the CT data. These strategies represent a substantial advancement in the CT-based characterisation of ores, since conventional segmentation has largely relied on grey value information. In addition, the utilisation of DECT has been demonstrated to be an effective and readily applicable tool to improve contrast in complex ores, as evidenced by the examined graphite ore. The findings suggest that the protocols developed in this thesis can be adapted and applied to other CRMs, considering their respective mineralogy and X-ray attenuation properties.

While CT is already proving beneficial in academic settings with sufficient time available and trained personnel, its widespread adoption in the mining industry (e.g., geometallurgical programs) remains challenging, especially because of sample heterogeneity, low cost-efficiency, and inherent limitations of the current CT method. Nevertheless, recent developments in AI offer a promising avenue for future advancements in CT since AI has the potential to mitigate many of the current limitations of CT. Thus, future research focusing on integrating AI along the CT data processing chain, as well as on automatisation, could significantly contribute to enhance the speed, accuracy, and standardisation of CT analysis. This advancement would not only provide a deeper understanding of ore deposits, but also lead to a more efficient resource extraction. Realising this potential would mark a significant step forward in the responsible and sustainable exploitation of CRMs.

- this page is intentionally left blank -

Appendix A

MRE CT facility

The CT laboratory at the Institute of Mineral Resources Engineering, RWTH Aachen University (Fig. A.1), is equipped with a ProCon CT Alpha scanner equipped with a five-axes-manipulation system. See Table A.1 for further technical configurations.

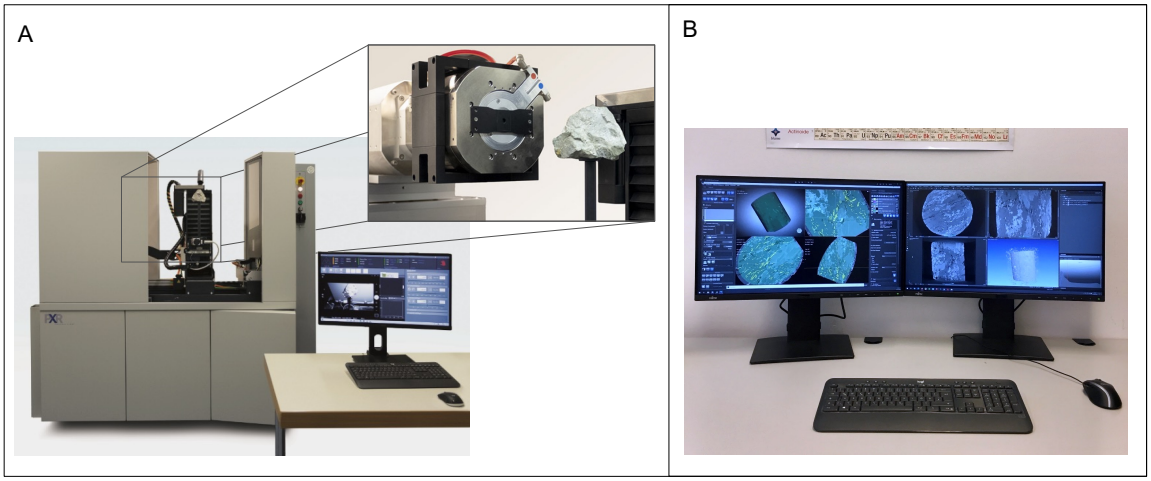

Figure A.1: CT lab at MRE, RWTH Aachen University. **A**) ProCon CT Alpha scanner with X-ray tube and specimen holder highlighted as well as acquisition PC for scanner configuration and storage of projection data. **B**) Workstation showing the interfaces of the image processing software ORS Dragonfly 2022.1 (left monitor) and reconstruction software VGStudio Max 3.5 (right monitor).

Table A.1: Fact sheet CT scanner.

X-ray tube: XWT-225-TCHE Plus	
Voltage range	20 - 225 kV
Current range	50 - 1000 μA
Target type	Transmission
Operation modi	Nanofocus (≤1.5 W), microfocus (≤10 W), high power (≤50 W)
Maximum resolution	1 μm*
Target material	Tungsten
Detector system: XRD 1611 AP3	
Type	Flat panel detector
Size	4064 x 4064 pixel (100 μm^2)
Material	Amorphous silica
Work station and software	
Chip	Intel(R) Xenon(R) CPU E5-2620 v4 @ 2.1 GHz
RAM	496 GB
Graphic card	NVIDIA GeForceRTX 2080 Ti
Image reconstruction	VGStudio MAX 3.5
Image processing and feature analysis	VGStudio MAX 3.5, ORS Dragonfly 2022.1

*According to manufacturer

Appendix B

Calculation of the effective atomic number of graphite and scheelite

General formula

The effective atomic number Z_{eff} for a compound such as a mineral is calculated using the power law eqation [258, 259] :

$$Z_{eff} = \sqrt[\beta]{\sum_{i}^{N} f_i \cdot Z_i^{\beta}}, \tag{B.1}$$

whereby Z_i represents the atomic number of the i-th element in the compound, and f_i denotes the fractional mass of this element in the compound. N refers to the total number of elements present in the compound. The exponent β captures how the photon's energy interacts with the electronic structure of the compound, reflecting changes in how the effective charge is perceived under different radiative conditions. It can vary between 2.94 and 3.8. [259–261]. For the exemplary calculation, β of 3.8 from Van Geet et al. [262] was used.

Graphite

1. Atomic number:

   Carbon (C): $Z_C = 6$

2. Calculation of Z_{eff}:

$$\begin{aligned} Z_{eff} &= \sqrt[3.8]{Z^{\beta}} \\ &= \sqrt[3.8]{6^{3.8}} \\ &\approx 6 \end{aligned}$$

Scheelite

1. Atomic numbers and fractions:

$$\text{Calcium (Ca): } Z_{\text{Ca}} = 20$$
$$\text{Tungsten (W): } Z_{\text{W}} = 74$$
$$\text{Oxygen (O): } Z_{\text{O}} = 8$$

2. Mass fractions of each element:

$$\text{Molar mass of } CaWO_4 = 287.92 \text{ g/mol}$$
$$\text{Mass fraction of Ca} = \frac{40.08}{287.92} \approx 0.139$$
$$\text{Mass fraction of W} = \frac{183.84}{287.92} \approx 0.638$$
$$\text{Mass fraction of O} = \frac{64.00}{287.92} \approx 0.222$$

3. Calculation of Z_{eff}:

$$\begin{aligned} Z_{eff} &= \sqrt[3.8]{\sum_i^N f_i \cdot Z_i^{3.8}} \\ &= \sqrt[3.8]{(0.139 \cdot 20^{3.8}) + (0.638 \cdot 74^{3.8}) + (0.222 \cdot 8^{3.8})} \\ &\approx 65.79 \end{aligned}$$

Appendix C

Article 2 and Article 3

C.1 Article 2

Table C.1: Mean Q factor values and results of Fisher LSD test for each material area and parameter combination from 10 ROIs for each phase and structure. Group A is the highest (marked dark green), and Group G is the lowest (marked dark orange) Q factor group. Members of the same group have no significant differences. The mean Q factor values, which belong only to the best or only to the worst group of the focused material area, are marked in bold. The highest mean Q factor value in each material areais marked bright green, and the lowest is bright orange. All mean Q factor value members of the best group drew green, of the worst – orange.

Parameter combination	Material area																			
	M1: Graphite - Quartz & Clay								M2: Graphite - Air								M3: Muscovite - HFO								M4: Muscovite - Quartz & Clay							
	mean Q	t-Test groups							mean Q	t-Test groups							mean Q	t-Test groups							mean Q	t-Test groups						
60 kV	2.990					F	G	H	**1.928**							H	**3.776**							H	2.709						F	G
80 kV	3.076				E	F	G		**2.237**							H	4.294				E	F	G	H	3.240				D	E		
170 kV	**2.404**							I	2.825				E	F	G		4.294				E	F	G	H	**2.450**							G
180 kV	2.508						H	I	2.951			D	E	F	G		4.068						G	H	**2.418**							G
190 kV	**2.359**							I	2.924				E	F	G		4.153					F	G	H	**2.305**							G
60 kV x 170 kV x 0.3	3.941	A	B	C					2.747					F	G		4.672			C	D	E	F	G	3.227				D	E		
60 kV x 170 kV x 0.5	3.968	A	B	C					3.447		B						5.182	A	B	C	D				4.056			C				
60 kV x 170 kV x 0.7	4.077	A	B						**3.915**	A							5.263	A	B	C	D				4.351		B	C				
60 kV x 180 kV x 0.3	3.437			C	D	E	F	G	2.717						G		4.547				D	E	F	G	3.251				D	E		
60 kV x 180 kV x 0.5	3.465			C	D	E	F	G	3.079			C	D	E	F		4.786		B	C	D	E	F	G	3.383				D	E		
60 kV x 180 kV x 0.7	3.176				D	E	F	G	3.159		B	C	D	E			4.623			C	D	E	F	G	3.058				D	E	F	
60 kV x 190 kV x 0.3	3.616		B	C	D	E			2.792					F	G		4.896	A	B	C	D	E	F		3.448				D			
60 kV x 190 kV x 0.5	3.649	A	B	C	D				3.377		B	C					5.304	A	B	C	D				3.448				D			
60 kV x 190 kV x 0.7	3.488			C	D	E	F		3.378		B	C					5.147	A	B	C	D				3.134				D	E	F	
80 kV x 170 kV x 0.3	3.078				E	F	G		2.630						G		4.798		B	C	D	E	F	G	3.061				D	E	F	
80 kV x 170 kV x 0.5	3.098			D	E	F	G		2.957				D	E	F	G	5.006	A	B	C	D	E			3.154				D	E	F	
80 kV x 170 kV x 0.7	2.910						G	H	I	3.070			C	D	E	F		4.849			B	C	D	E	F	2.982					E	F	
80 kV x 180 kV x 0.3	3.195				D	E	F	G	2.866					E	F	G	4.925	A	B	C	D	E			3.088				D	E	F	
80 kV x 180 kV x 0.5	**4.232**	A							**3.855**	A							**5.675**	A							**4.824**	A						
80 kV x 180 kV x 0.7	3.190				D	E	F	G	3.318		B	C					4.930	A	B	C	D	E	F		3.110				D	E	F	
80 kV x 190 kV x 0.3	4.087	A	B						3.308		B	C					5.356	A	B	C					4.526	A	B					
80 kV x 190 kV x 0.5	3.860	A	B	C					**3.874**	A							5.495	A	B						4.546	A	B					
80 kV x 190 kV x 0.7	3.067					E	F	G	3.294		B	C	D				4.973	A	B	C	D	E			2.950					E	F	

Table C.2: Global, mean, and standard deviation values of the CNR and Q-factor measurements of each material area.

Parameter combination	Material area																							
	M1: Graphite - Quartz & Clay						M2: Graphite - Air						M3: Muscovite - HFO						M4: Muscovite - Quartz & Clay					
	CNR			Q-factor			CNR			Q-factor			CNR			Q-factor			CNR			Q-factor		
	global	mean	std	global	mean	std	global	mean	std	global	mean	std	global	mean	std	global	mean	std	global	mean	std	global	mean	std
60 kV	4.24	4.33	0.53	2.93	2.99	0.31	2.8	2.86	0.52	1.9	1.93	0.28	5.01	5.01	0.96	3.77	3.78	0.76	3.67	3.8	0.45	2.64	2.71	0.29
80 kV	4.42	4.52	0.55	3	3.08	0.39	3.07	3.31	0.38	2.21	2.24	0.23	5.66	5.73	0.91	4.28	4.29	0.67	4.4	4.68	0.89	3.07	3.24	0.58
170 kV	3.52	3.55	0.41	2.39	2.4	0.25	3.93	3.99	0.57	2.81	2.82	0.28	5.63	5.75	1.21	4.25	4.29	0.85	3.46	3.49	0.26	2.44	2.45	0.14
180 kV	3.62	3.66	0.32	2.49	2.51	0.17	4.77	4.4	0.48	2.93	2.95	0.28	5.38	5.42	0.94	4.07	4.07	0.68	3.45	3.46	0.2	2.42	2.42	0.17
190 kV	3.46	3.55	0.54	2.34	2.36	0.23	4.17	4.21	0.41	2.92	2.92	0.23	5.54	5.58	0.89	4.14	4.15	0.66	3.3	3.33	0.25	2.29	2.31	0.17
60 kV x 170 kV x 0.3	4.81	4.84	0.58	3.35	3.94	1.76	3.88	4	0.68	2.7	2.75	0.34	6.08	6.14	1.17	4.66	4.67	0.89	4.42	4.56	0.51	3.15	3.23	0.32
60 kV x 170 kV x 0.5	5.76	5.33	0.66	3.82	3.97	0.5	4.79	4.99	0.88	3.37	3.45	0.46	6.69	6.81	1.31	5.15	5.18	0.93	5.53	5.79	0.9	3.9	4.06	0.59
60 kV x 170 kV x 0.7	6	6.17	0.83	3.95	4.08	0.66	5.43	5.7	1.19	3.8	3.92	0.63	6.78	6.92	1.3	5.23	5.26	0.88	5.97	6.33	1.18	4.15	4.35	0.73
60 kV x 180 kV x 0.3	4.93	5.03	0.57	3.38	3.44	0.32	3.9	4.03	0.95	2.67	2.72	0.56	5.91	6	1.23	4.52	4.55	0.93	4.46	4.57	0.47	3.19	3.25	0.29
60 kV x 180 kV x 0.5	5.01	5.08	0.48	3.4	3.47	0.33	4.58	4.67	0.83	3.05	3.08	0.47	6.17	6.29	1.35	4.76	4.79	0.98	5.13	5.18	1.53	3.64	3.38	1.09
60 kV x 180 kV x 0.7	4.57	4.61	0.37	3.15	3.18	0.25	4.76	4.8	0.6	3.14	3.16	0.37	6.01	6.12	1.29	4.6	4.62	0.89	4.33	4.36	0.39	3.04	3.06	0.26
60 kV x 190 kV x 0.3	5.22	5.3	0.48	3.56	3.62	0.3	4.03	4.1	0.58	2.77	2.79	0.34	6.31	6.36	1.27	4.88	4.9	0.96	4.83	4.92	0.43	3.4	3.45	0.25
60 kV x 190 kV x 0.5	5.44	5.51	0.52	3.6	3.65	0.33	5.05	5.08	0.43	3.36	3.38	0.28	6.83	6.97	1.22	5.28	5.3	0.8	4.88	4.93	0.37	3.42	3.45	0.23
60 kV x 190 kV x 0.7	5.2	5.46	1.36	3.45	3.49	0.34	4.95	5.03	0.55	3.35	3.38	0.25	6.57	6.69	1.39	5.11	5.15	0.93	4.52	4.54	0.23	3.12	3.13	0.19
80 kV x 170 kV x 0.3	4.59	4.64	0.32	3.01	3.08	0.33	3.73	3.78	0.42	2.62	2.63	0.19	6.19	6.32	1.13	4.76	4.8	0.82	4.24	4.34	0.48	3	3.06	0.32
80 kV x 170 kV x 0.5	4.67	4.71	0.34	3.04	3.1	0.31	4.15	4.22	0.66	2.94	2.96	0.24	6.44	6.59	1.24	4.96	5.01	0.88	4.4	4.48	0.44	3.11	3.15	0.27
80 kV x 170 kV x 0.7	4.39	4.43	0.38	2.87	2.91	0.27	4.23	4.32	0.69	3.06	3.07	0.27	6.29	6.44	1.27	4.8	4.85	0.87	4.18	4.24	0.35	2.96	2.98	0.2
80 kV x 180 kV x 0.3	4.59	4.66	0.48	3.11	3.2	0.43	4.09	4.12	0.42	2.84	2.87	0.29	6.37	6.59	1.38	4.88	4.93	0.86	4.26	4.33	0.32	3.05	3.09	0.18
80 kV x 180 kV x 0.5	6.21	6.4	1.01	4	4.23	0.78	5.73	6.06	1.43	3.68	3.86	0.79	7.44	7.65	1.67	5.64	5.68	0.99	6.61	7.06	1.33	4.62	4.82	0.76
80 kV x 180 kV x 0.7	4.7	4.73	0.31	3.17	3.19	0.24	4.93	5.01	0.58	3.26	3.32	0.4	6.54	6.62	1.28	4.93	4.93	0.85	4.43	4.46	0.26	3.1	3.11	0.2
80 kV x 190 kV x 0.3	5.95	6.42	2.12	3.84	4.09	1.16	4.79	4.91	0.79	3.24	3.31	0.43	6.89	7.13	1.47	5.32	5.36	0.96	6.07	6.6	1.45	4.23	4.53	0.9
80 kV x 190 kV x 0.5	6.29	6.59	1.2	4.1	3.86	1.5	5.6	5.71	0.78	3.8	3.87	0.52	6.99	7.22	1.45	5.44	5.5	0.89	6.26	6.7	1.31	4.3	4.55	0.8
80 kV x 190 kV x 0.7	4.58	4.64	0.56	3.05	3.07	0.22	4.84	4.87	0.4	3.28	3.29	0.15	6.44	6.59	1.2	4.94	4.97	0.77	4.23	4.27	0.28	2.93	2.95	0.17

C.2 Article 3

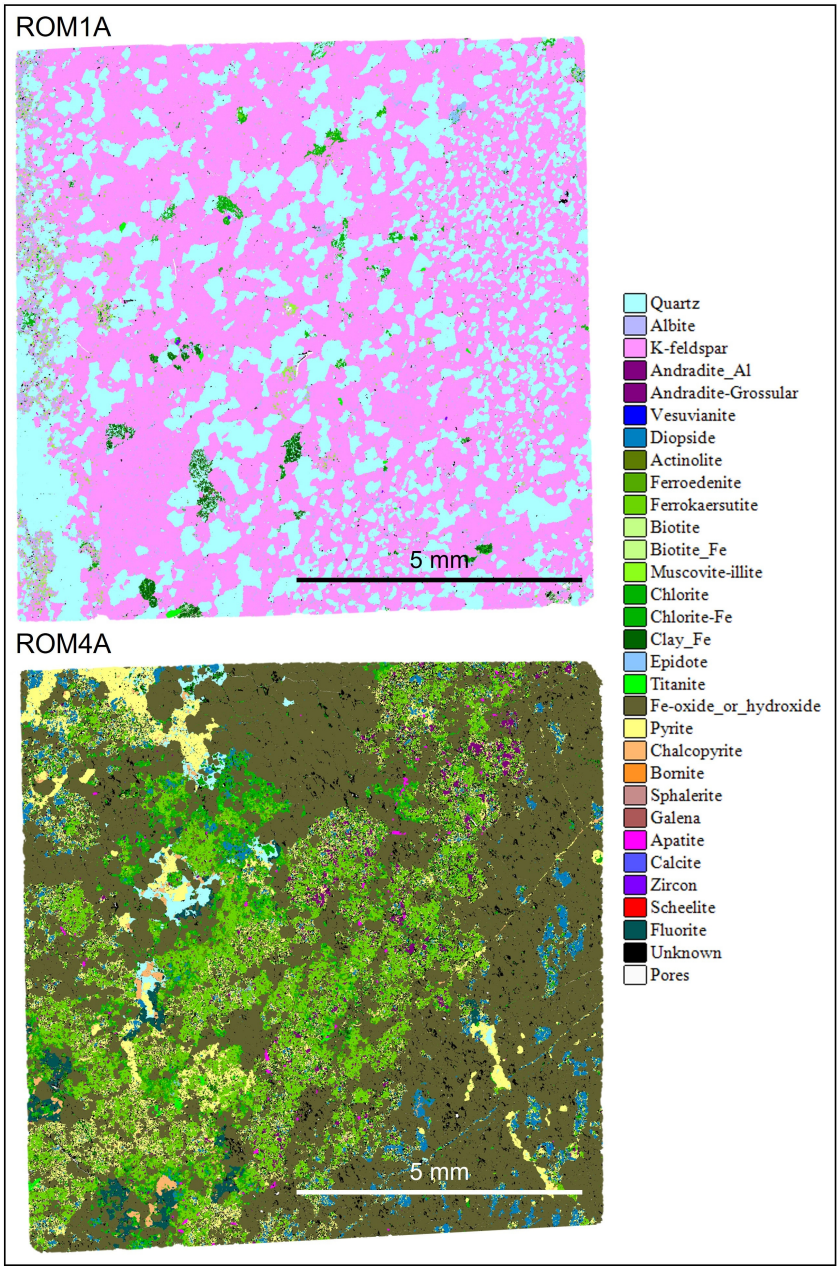

Figure C.1: AMICS data of the two ore samples (ROM1 and ROM4) studied. The colour-coding is for a better illustration, with minerals belonging to the same group marked with similar colours. The ROM1 sample consists mainly of K-feldspar (pink) and quartz (cyan). The ROM4 sample is composed primarily of magnetite (brown), amphibole (green), and pyrite (yellow). In both samples, the minerals show subhedral or anhedral shapes, occasionally featuring pervasive textures. Given the number of minerals, a few phases not belonging to the same group, inevitably have similar colours (e.g., titanite and muscovite); note that mica (biotite and muscovite) is absent in ROM4 and amphibole minerals (actinolite, ferroedenite, ferrokaersutite) absent ROM1. For more detailed visualisation (e.g., to distinguish between bornite and chalcopyrite), the figure has been included to the Supplementary materials at original resolution.

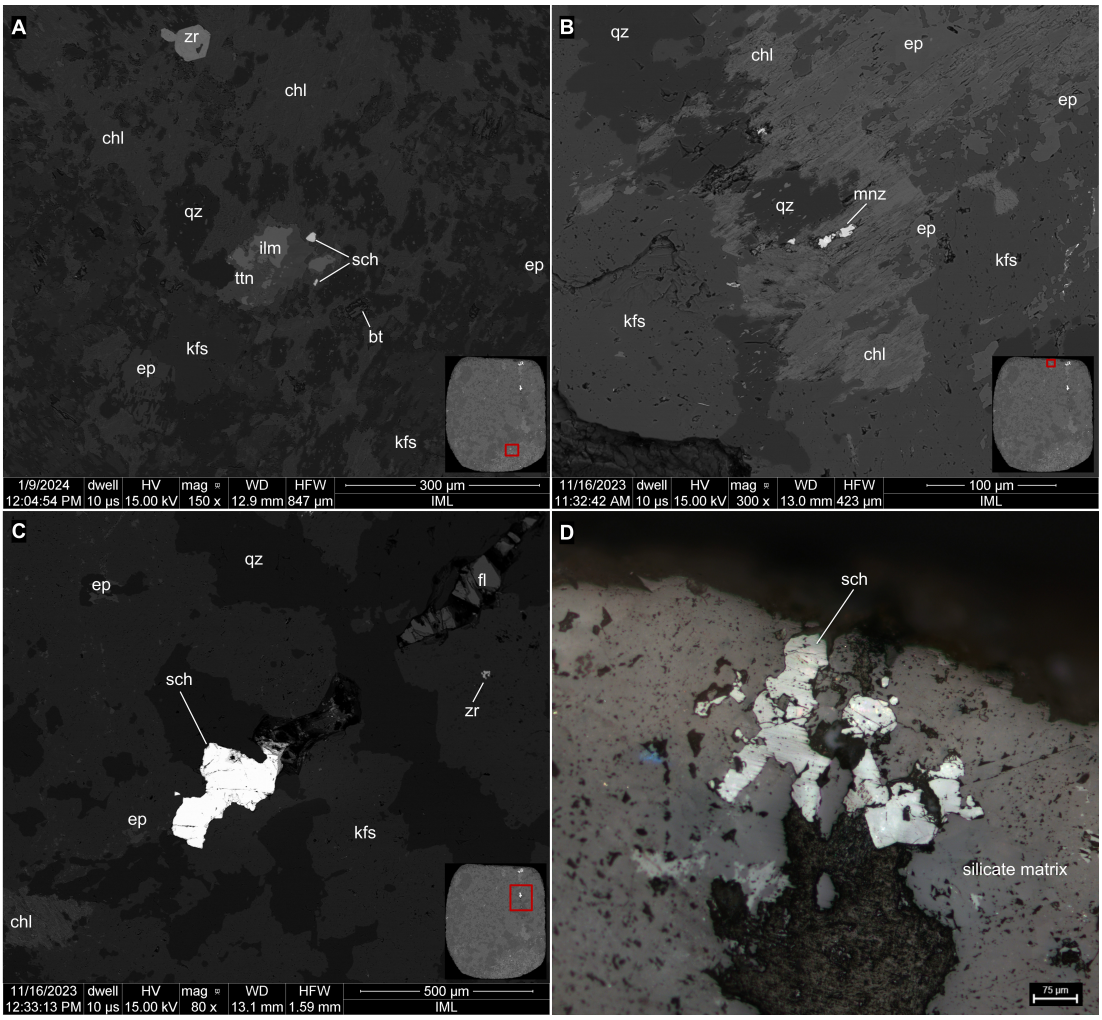

Figure C.2: A-C) SEM images, and **D**) OM microphotograph of the ROM1 sample. Note anhedral chlorite being partially overprinted by subhedral epidote (**A, B**). Abbreviations: Bt = biotite, chl = chlorite, ep = epidote, fl = fluorite, ilm = ilmenite, kfs = K-feldspar, mnz = monazite, qz = quartz, sch = scheelite, ttn = titanite, zr = zircon.

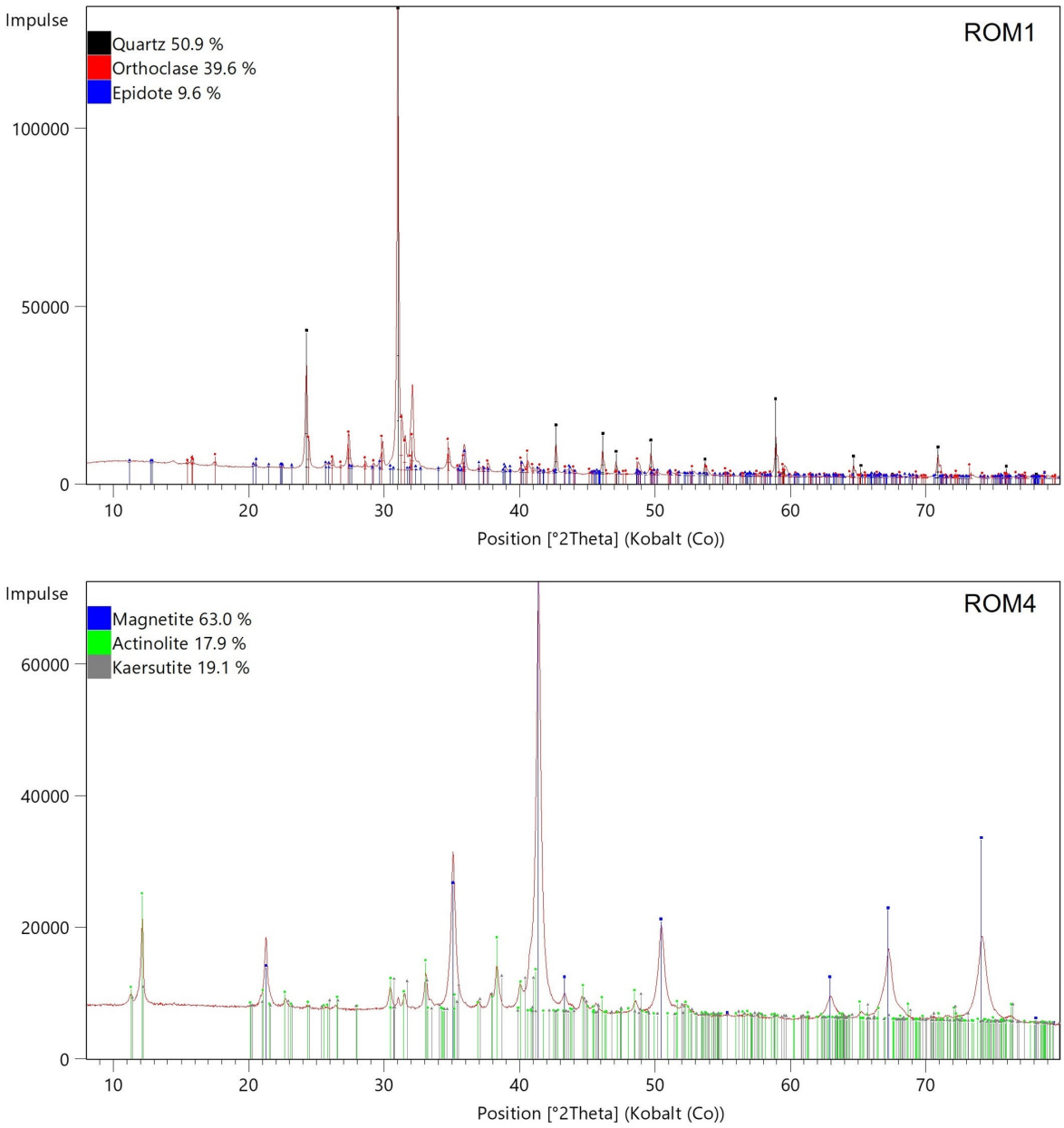

Figure C.3: XRD patterns of the samples investigated. The undefined peak at 14.4 2θ in the XRD pattern of ROM1 is chlorite. However, it was not identified by the Highscore software.

- this page is intentionally left blank -

Appendix D

Best practices and additional data from experimental work

Best practices for optimising CT acquisition

The research findings presented in this work suggest some basic rules for optimising CT acquisition concerning the ores examined:

1. *Sample mounting and orientation:* Since the CT system's sample stage is constructed from metal, it is crucial to mount the sample on a low-density specimen holder, such as hard foam, and to separate it from the metal components of the rotation stage. This separation prevents X-ray absorption or scattering from the metal, which would degrade scan quality. Additionally, the holder's material should have minimal X-ray attenuation to maintain optimal penetration of X-rays in areas of the sample in direct contact, preserving the greyscale integrity of the reconstructed CT dataset. The sample should also be mounted at a slight angle and securely fastened to both the specimen holder and rotational stage to prevent movement during acquisition. This configuration ensures sharp CT images across all slices, including the topmost and bottommost slice.
2. *Maximise beam efficacy:* Use a cylindrical sample for uniform X-ray path lenghts. Adjust sample dimensions to allow close positioning to the X-ray source, and ensure that the chosen thickness allows adequate X-ray penetration. Tilt the sample to maximise spatial resolution. Avoid pre-filters when possible as they demand longer exposure times and may decrease image contrast.
3. *Prioritise voltage:* Understanding the relationship between attenuation mechanisms and μ is crucial for effectively differentiating minerals in a CT scan. The selection of X-ray source parameters should always prioritise voltage due to its significant impact on image contrast. Ores with low-absorbing target minerals (e.g., graphite ores), containing both low and high absorbing phases, require a balanced voltage setting (e.g., 100 kV was found effective in this research). For ores with very high-absorbing target minerals (e.g., scheelite in tungsten ores), maximising kV is generally required to mitigate beam hardening, regardless of the overall mineralogy.
4. *Adjust remaining parameters:* Once the optimal kV is determined, the remaining parameters should be adjusted to optimise image noise, brightness and spatial resolution. Image noise can be reduced by increasing primarily frame averaging, while brightness is improved by

using higher exposure time, or beam current. Using a small focal spot (e.g., microfocus beam, used in articles 2 and 3 increases the spatial resolution and thus image quality as a smaller focal spot enhances image sharpness. Note that when adjusting these parameters, it is also important to consider the aspects below.

(a) The scanning parameters influence multiple aspects of image quality simultaneously. For example, while exposure time primarily affects brightness, it also has a secondary effect on noise due to the increased signal. Therefore, it is recommended to begin first selecting the parameter primarily responsible for the desired image quality factor.

(b) A balance between these parameters is essential to avoid overexposure of the detector. For example, when using a microfocus focal spot, the applied power must not exceed 10 W (Table A.1).

5. *Apply DECT:* When available and when examining complex ores with weakly X-ray attenuating ore minerals like graphite, utilise DECT to mitigate the large spectrum of X-ray attenuation properties of the minerals, ultimately facilitating parameter selection.

Recommendations for segmentation

On the basis of these results, DL-based segmentation is recommended for graphite and scheelite ore analysis, as it can effectively mitigate the impact of scanning artefacts, such as beam hardening and the cone-beam effect. Furthermore, it is less influenced by human error given sufficient ground truth data is provided during the inference stage. Therefore, it suggested to always apply DL-based segmentation quantitatively analysing ores other than graphite and scheelite ores, particularly when aiming for modal mineralogy analysis. Among the various deep-learning algorithms offered in Dragonfly, the 3D-sensor architecture [145] yielded the most accurate results for segmentation and is therefore recommended.

Effect of sample orientation on spatial resolution

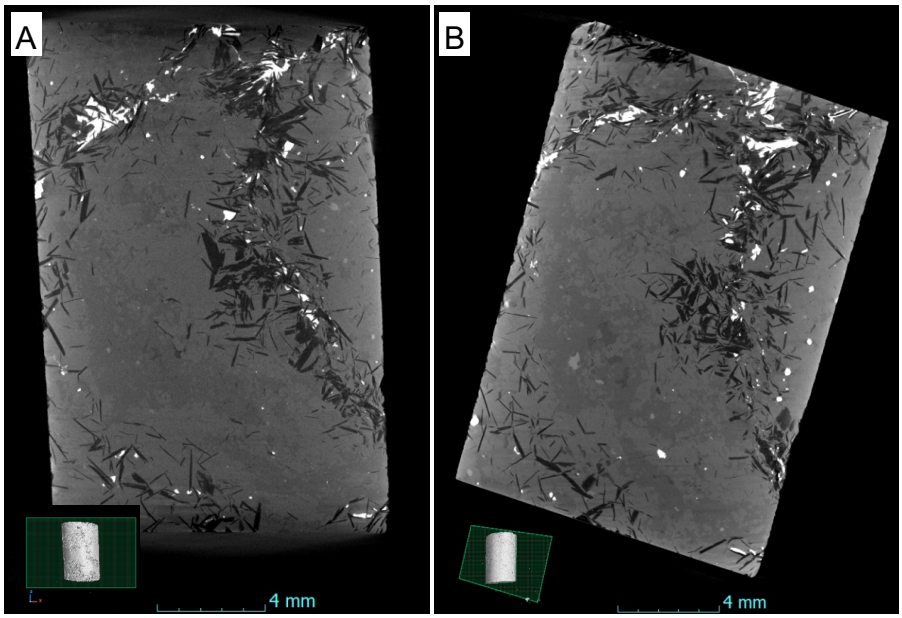

Figure D.1: A) Reconstructed dataset of a flake graphite ore sample positioned horizontally. **B**) Reconstructed dataset of the same sample, positioned at a tilted orientation.

- this page is intentionally left blank -

Glossary

A priori analysis refers to a set of conventional mineralogical analysis techniques performed in this work before CT data was collected. These techniques are essential for proper data aquisition, identifying the minerals present in a sample and providing context for interpreting the CT images [46].

Artificial intelligence is the design and creation of computer systems that can carry out tasks typically associated with human intelligence, including visual perception, speech recognition, making decisions, and translating languages [263].

Beam current refers to the flow of electric charge through the X-ray tube, typically measured in milliamperes (mA) [43]. It determines the number of X-ray photons produced per unit time [43].

Beam hardening refers to an artefact that occurs in CT imaging, when lower-energy X-rays in a polychromatic X-ray beam are absorbed more easily by the material, leaving higher-energy X-rays to penetrate the object [50]. This effect results in the X-ray beam becoming 'hardened', as it effectively contains a higher proportion of high-energy X-rays.

Complex ore is a polyphase ore containing multiple valuable metals or minerals, requiring advanced processing methods for efficient extraction and recovery of all components, e.g., due to challenges posed by their co-occurences or liberating valuable minerals from impurites [8, 264].

Deep learning is a subset of artificial intelligence that uses artificial neural networks with multiple layers to automatically learn patterns and representations from large amounts of data [60]. Unlike traditional models, it automatically extracts features and captures complex relationships in data through hierarchical layers [59]. This enables complex tasks like image segmentation by modeling non-linear patterns.

Dice score is a common metric used to evaluate the performance of segmentation algorithms [265]. It measures the overlap between the predicted segmentation mask and the ground truth mask by computing the similarity between the two sets. A higher dice score indicates better agreement between the predicted and ground truth segmentations, thereby providing a quantitative measure of segmentation accuracy.

Effective atomic number (Z_{eff}) is the net positive charge an electron perceives in an atom, accounting for both the atomic number (Z) and electron shielding [258, 259]. Z_{eff} varies with radiation energy, which influences electron shielding effects [261]. In single-phase materials, Z_{eff} approximates Z due to consistent bonding and minimal shielding. In polyphase

materials, Z_{eff} averages electron interactions across different phases, therefore differing from the average atomic number, which calculates the mean of atomic numbers based on component proportions without considering radiation effects.

Exposure time refers to the duration during which the X-ray tube emits radiation [47]. It directly impacts the number of X-ray photons interacting with the sample, affecting image quality. For example, longer exposure times increase photon flux, enhancing the signal-to-noise ratio by reducing statistical noise.

Filtered back projection is common technique used in computed tomography to reconstruct a two-dimensional (2D) image from a set of one-dimensional (1D) projections taken from different angles [48]. The process involves two main steps: first, each 1D projection is filtered to reduce blurring and enhance image quality. Then, the filtered projections are back-projected across the image plane in their respective directions, accumulating the contributions from all angles to reconstruct the original 2D image. FBP is valued for its computational simplicity and speed but can be prone to artefacts, particularly in low-dose or noisy data.

Focal spot size is the diameter of the area on the X-ray tube's anode where X-rays are emitted [47]. It influences image resolution, with a smaller focal spot size providing finer image detail and sharper resolution.

Frame averaging is the process of averaging multiple projections acquired sequentially over a short period of time at the same sample stage angle [44].

Ground truth data refers to manually labeled data used to train and evaluate models, serving as a benchmark for comparing model predictions to guide learning [266].

Inference is the process of using a trained deep learning model to make predictions or decisions on new, unseen data based on the learned patterns from the training phase [59].

Line integral represents the total attenuation of X-rays along a specific path through the scanned object, being the sum of the attenuation coefficients of all materials encountered along that path [47].

Linear attenuation coefficient (μ) is a constant, describing the fraction of attenuated incident photons in a monoenergetic beam per unit thickness of a material [44]. This value depends on the material's density, atomic composition (Z_{eff}), and the energy of the X-rays and is expressed numerically in units of cm^{-1}. The coefficient increases with higher atomic number and material density, but decreases with increasing photon energy.

Ore texture refers to the spatial arrangement and relationships between the minerals within an ore, including their size, shape, distribution, and the way they are intergrown or associated with each other [19].

Paralellisation refers to the process of dividing a computational task into smaller parts that can be executed simultaneously across multiple processors or cores, rather than sequentially on a single processor [267]. This approach can significantly reduce the time required to complete complex tasks by allowing multiple calculations to be performed at the same time.

Partial volume effect occurs in CT when a single voxel contains multiple phases, resulting in mixed attenuation coefficients, or grey values, respectively [83]. This blending effect causes particles close to or smaller than the voxel size to appear blurred, distorted, or unrealistic in shape, complicating accurate characterisation of small or finely detailed structures.

Projection is the collection of line integrals along all paths through the object at a specific angle, recorded during the rotation of the sample stage and digitally stored [68].

Scanning artefacts refer to distortions in the acquired image data, arising from hardware or processing limitations that may obscure or mimic real features of the sample [50].

Spatial resolution Refers to the smallest distinguishing feature in a CT image, indicating the level of detail that can be resolved [83].

Synchrotron CT is a specialised CT technique using high-energy X-rays from a synchrotron particle accelerator. It offers superior spatial and temporal resolution, enabling imaging of denser materials and rapid processes [206].

Target mineral refers to a mineral of interest wanted for valorisation [268].

Voltage is the electric potential applied across the X-ray tube that will accelerate electrons up to this maximum energy. It determines the energy of the X-rays produced [43].

- this page is intentionally left blank -

Bibliography

[1] L. Mancini, B. Vidal Legaz, M. Vizzarri, D. Wittmer, G. Grassi, D. Pennington, Mapping the role of raw materials in sustainable development goals (KJ-1A-29595-EN-N (online)) (2019). doi:10.2760/026725.

[2] T. E. Graedel, E. M. Harper, N. T. Nassar, B. K. Reck, On the materials basis of modern society, Proceedings of the National Academy of Sciences 112 (20) (2015) 6295–6300. doi:10.1073/pnas.1312752110.

[3] G. T. Nwaila, H. E. Frimmel, S. E. Zhang, J. E. Bourdeau, L. C. Tolmay, R. J. Durrheim, Y. Ghorbani, The minerals industry in the era of digital transition: An energy-efficient and environmentally conscious approach, Resources Policy 78 (1–4) (2022) 102851. doi:10.1016/j.resourpol.2022.102851.

[4] European Commission, The european green deal (2024).
URL https://commission.europa.eu/strategy-and-policy/priorities-2019-2024/european-green-deal_en

[5] E. Commission, E. Directorate-General for Internal Market, Industry, SMEs, G. Blengini, C. El Latunussa, U. Eynard, C. Torres De Matos, D. Wittmer, K. Georgitzikis, C. Pavel, S. Carrara, L. Mancini, M. Unguru, D. Blagoeva, F. Mathieux, D. Pennington, Study on the EU's list of critical raw materials (2020) – final report, Publications Office of the European Union, 2020. doi:doi/10.2873/11619.

[6] C. Baranzelli, D. Blagoeva, G. A. Blengini, C. Ciupagea, J. Dewulf, P. Dias, Y. Kayam, C. E. L. Latunussa, L. Mancini, S. Manfredi, A. Marmier, F. Mathieux, V. Nita, P. Nuss, C. Pavel, D. Pennington, L. Talens Peirò, C. Torres De Matos, E. Tzimas, B. Vidal-Legaz, Methodology for establishing the European Union list of critical raw materials: Guidelines, Publications Office of the European Union, Luxembourg, 2017.

[7] C. Bauer, R. Wagner, J. Leisner, Detection of foreign items in laundry industry—a dual energy XRT approach, Engineering Proceedings 21 (1) (2022) 14. doi:10.3390/engproc2022021014.

[8] B. Wills, J. Finch, Wills' mineral processing technology: an introduction to the practical aspects of ore treatment and mineral recovery, Elsevier Science, 2015.

[9] F. Wellmer, P. Buchholz, J. Gutzmer, C. Hagelüken, P. Herzig, R. Littke, R. Thauer, Raw materials for future energy supply, Springer International Publishing, 2018.

[10] World Economic Forum, Lessons on critical metals circularity for energy transition (27.5.2024).

URL https://www.weforum.org/agenda/2024/04/what-we-can-learn-on-critical-metals-circularity-from-the-platinum-metals-group-industry/

[11] International Energy Agency (IEA), The role of critical minerals in clean energy transitions (2020).
URL https://www.iea.org/reports/the-role-of-critical-minerals-in-clean-energy-transitions

[12] J. Asenbauer, T. Eisenmann, M. Kuenzel, A. Kazzazi, Z. Chen, D. Bresser, The success story of graphite as a lithium-ion anode material–fundamentals, remaining challenges, and recent developments including silicon (oxide) composites, Sustainable Energy & Fuels 4 (11) (2020) 5387–5416.

[13] E. Lassner, W. Schubert, Tungsten: properties, chemistry, technology of the element, alloys, and chemical compounds, Springer US, 2012.

[14] A. D. Jara, A. Betemariam, G. Woldetinsae, J. Y. Kim, Purification, application and current market trend of natural graphite: A review, International Journal of Mining Science and Technology 29 (5) (2019) 671–689. doi:10.1016/j.ijmst.2019.04.003.

[15] A. C. R. Miranda, G. Beaudoin, B. Rottier, Scheelite chemistry from skarn systems: Implications for ore-forming processes and mineral exploration, Mineralium Deposita 57 (8) (2022) 1469–1497. doi:10.1007/s00126-022-01118-y.

[16] M. Frenzel, R. Baumgartner, R. Tolosana-Delgado, J. Gutzmer, Geometallurgy: present and future, Elements 19 (6) (2023) 345–351.

[17] C. D. Gribble, Optical mineralogy: principles and practice, Springer Science & Business Media, 2012.

[18] B. Schulz, D. Sandmann, S. Gilbricht, SEM-based automated mineralogy and its application in geo- and material sciences, Minerals 10 (11) (2020) 1004. doi:10.3390/min10111004.

[19] J. R. Craig, D. J. Vaughan, R. D. Hagni, Ore microscopy and ore petrography, Vol. 406, Wiley New York, 1981.

[20] S. Spencer, D. Sutherland, Stereological correction of mineral liberation grade distributions estimated by single sectioning of particles, Image Anal. Stereol. 19 (3) (2000) 175–182. doi:10.5566/ias.v19.p175-182.

[21] V. Cnudde, M. N. Boone, High-resolution X-ray computed tomography in geosciences: a review of the current technology and applications, Earth-Science Reviews 123 (4) (2013) 1–17. doi:10.1016/j.earscirev.2013.04.003.

[22] G. D. Rubin, Computed tomography: Revolutionizing the practice of medicine for 40 years, Radiology 273 (2 Suppl) (2014) S45–74. doi:10.1148/radiol.14141356.

[23] H. Villarraga-Gómez, E. L. Herazo, S. T. Smith, X-ray computed tomography: from medical imaging to dimensional metrology, Precision Engineering 60 (2) (2019) 544–569. doi:10.1016/j.precisioneng.2019.06.007.

[24] L. de Chiffre, S. Carmignato, J.-P. Kruth, R. Schmitt, A. Weckenmann, Industrial applications of computed tomography, CIRP Annals 63 (2) (2014) 655–677. doi:10.1016/j.cirp.2014.05.011.

[25] R. Kramme, K.-P. Hoffmann, R. S. Pozos, Springer Handbook of Medical Technology, Springer Berlin Heidelberg, Berlin, Heidelberg, 2012.

[26] J. R. Kyle, R. A. Ketcham, Application of high resolution X-ray computed tomography to mineral deposit origin, evaluation, and processing, Ore Geology Reviews 65 (B2) (2015) 821–839. doi:10.1016/j.oregeorev.2014.09.034.

[27] Y. Wang, J. D. Miller, Current developments and applications of micro-CT for the 3D analysis of multiphase mineral systems in geometallurgy, Earth-Science Reviews 211 (18) (2020) 103406. doi:10.1016/j.earscirev.2020.103406.

[28] L. T. Krebbers, N. Grozmani, B. G. Lottermoser, R. H. Schmitt, Application of multispectral computed tomography for the characterisation of natural graphite, e-Journal of Nondestructive Testing 28 (3) (2023). doi:10.58286/27710.

[29] B. Godel, S.-J. Barnes, W. D. Maier, 3-D distribution of sulphide minerals in the Merensky Reef (Bushveld Complex, South Africa) and the J-M Reef (Stillwater Complex, USA) and their relationship to microstructures using X-ray computed tomography, Journal of Petrology 47 (9) (2006) 1853–1872. doi:10.1093/petrology/egl029.

[30] B. Godel, S. J. Barnes, S.-J. Barnes, W. D. Maier, Platinum ore in three dimensions: Insights from high-resolution X-ray computed tomography, Geology 38 (12) (2010) 1127–1130. doi:10.1130/G31265.1.

[31] J. R. Kyle, R. A. Ketcham, In situ distribution of gold in oes using high resolution X-ray computed tomography, Economic Geology 98 (8) (2003) 1697–1701. doi:10.2113/gsecongeo.98.8.1697.

[32] J. R. Kyle, A. S. Mote, R. A. Ketcham, High resolution X-ray computed tomography studies of grasberg porphyry cu-au ores, papua, indonesia, Mineralium Deposita 43 (5) (2008) 519–532. doi:10.1007/s00126-008-0180-8.

[33] Y. Ren, J. Li, X. Sun, Z. Li, Z. Sun, Genesis of metal sulfides and its significance on graphite mineralization in the Huangyangshan graphite deposit, East Junggar, Xinjiang Province, China, Minerals 12 (11) (2022) 1450. doi:10.3390/min12111450.

[34] A. Fatima, A. S. Venkatesh, R. Mukherjee, A. K. Agrawal, B. Singh, P. S. Sarkar, Y. Kashyap, T. Shripathi, 3D spatial distribution of ore mineral phases using high resolution synchrotron micro-computed tomography (mCT) combined with optical microscopy, Applied Radiation and Isotopes (148) (2019) 49–59. doi:10.1016/j.apradiso.2019.03.013.

[35] S. G. Le Roux, A. Du Plessis, A. Rozendaal, The quantitative analysis of tungsten ore using X-ray microCT: Case study, Computers & Geosciences 85 (1) (2015) 75–80. doi:10.1016/j.cageo.2015.09.009.

[36] A. Rozendaal, S. G. Le Roux, A. Du Plessis, Application of microCT scanning in the recovery of endo-skarn associated scheelite from the Riviera Deposit, South Africa, Minerals Engineering 116 (2018) 163–178.

[37] C. Leroy, P.-G. Rancoita, Principles of radiation interaction in matter and detection, 3rd Edition, World Scientific, New Jersey, NJ [u.a.], 2012.

[38] C. Denison, W. Carlson, R. Ketcham, Three-dimensional quantitative textural analysis of metamorphic rocks using high-resolution computed X-ray tomography: part I. methods and techniques, Journal of Metamorphic Geology 15 (1) (1997) 29–44.

[39] L. T. Krebbers, J. A. Hunt, B. G. Lottermoser, Computed tomography of scheelite ore, Kara, Australia: morphological characterisation and modal mineralogy, Minerals 14 (4) (2024). doi:10.3390/min14040345.

[40] B. Agarwal, X-ray spectroscopy: an introduction, Springer Series in Optical Sciences, Springer Berlin Heidelberg, 2013.

[41] P. Sprawls, Physical principles of medical imaging, An Aspen publication, Aspen Publishers, 1993.

[42] R. van Grieken, A. Markowicz, Handbook of X-ray spectrometry, CRC Press, 2001.

[43] J. Hsieh, Computed tomography: principles, design, artifacts, and recent advances, SPIE Press, 2003.

[44] P. J. Withers, C. Bouman, S. Carmignato, V. Cnudde, D. Grimaldi, C. K. Hagen, E. Maire, M. Manley, A. Du Plessis, S. R. Stock, X-ray computed tomography, Nature Reviews Methods Primers 1 (18) (2021). doi:10.1038/s43586-021-00015-4.

[45] E. Maire, P. J. Withers, Quantitative x-ray tomography, International Materials Reviews 59 (1) (2014) 1–43. doi:10.1179/1743280413Y.0000000023.

[46] L. T. Krebbers, B. G. Lottermoser, X. Liu, Computed tomography of flake graphite ore: data acquisition and image processing, Minerals 13 (2) (2023) 247. doi:10.3390/min13020247.

[47] S. Carmignato, W. Dewulf, R. Leach, Industrial X-ray computed tomography, Springer International Publishing, Cham, 2018. doi:10.1007/978-3-319-59573-3.

[48] L. A. Feldkamp, L. C. Davis, J. W. Kress, Practical cone-beam algorithm, Josa a 1 (6) (1984) 612–619.

[49] Volume Graphics GmbH, VGSTUDIO MAX 3.5.1, accessed: 2024-10-22 (2021).
URL https://www.volumegraphics.com/en/products/vgsm.html

[50] F. E. Boas, D. Fleischmann, CT artifacts: causes and reduction techniques, Imaging Med. 4 (2) (2012) 229–240.

[51] L. T. Krebbers, N. Grozmani, B. G. Lottermoser, R. H. Schmitt, Dual-energy computed tomography for improved contrast on a polyphase graphitic ore, Tomography of Materials and Structures 4 (100021) (2024). doi:10.1016/j.tmater.2023.100021.

[52] T. Lei, A. Nandi, Image segmentation: principles, techniques, and applications, John Wiley & Sons, Hoboken, 2022.

[53] H. Mittal, A. C. Pandey, M. Saraswat, S. Kumar, R. Pal, G. Modwel, A comprehensive survey of image segmentation: clustering methods, performance parameters, and benchmark datasets, Multimedia Tools and Applications (2022) 1–26.

[54] P. I. Guntoro, Y. Ghorbani, P.-H. Koch, J. Rosenkranz, X-ray microcomputed tomography (μCT) for mineral characterization: A review of data analysis methods, Minerals 9 (2019) 183. doi:10.3390/min9030183.

[55] R. Nilakant, H. P. Menon, K. Vikram, A survey on advanced segmentation techniques for brain MRI image segmentation, International Journal on Advanced Science, Engineering and Information Technology 7 (4) (2017) 1448–1456.

[56] X. Liu, L. Song, S. Liu, Y. Zhang, A review of deep-learning-based medical image segmentation methods, Sustainability 13 (3) (2021) 1224.

[57] V. A. Jaques, A. Du Plessis, M. Zemek, J. Šalplachta, Z. Stubianová, T. Zikmund, J. Kaiser, Review of porosity uncertainty estimation methods in computed tomography dataset, Measurement Science and Technology 32 (12) (2021) 122001.

[58] S. Chauhan, Phase Segmentation and Analysis of Tomographic Rock Images Using Machine Learning Techniques: Doctoral dissertation, Universitäts-und Landesbibliothek Darmstadt, 2019.

[59] S. Ghosh, N. Das, I. Das, U. Maulik, Understanding deep learning techniques for image segmentation, ACM computing surveys (CSUR) 52 (4) (2019) 1–35.

[60] X. Li, G. Zhang, K. Li, W. Zheng, Deep learning and its parallelization, in: R. Buyya, R. N. Calheiros, A. E. Dastjerdi (Eds.), Big Data: Principles and Paradigms, Elsevier/Morgan Kaufmann, Cambridge, MA, USA, 2016, pp. 95–118.

[61] Object Research Systems (ORS), Dragonfly, accessed: 2024-10-22 (2022).
URL https://dragonfly.comet.tech/

[62] A. O. Salau, S. Jain, Feature extraction: a survey of the types, techniques, applications, in: 2019 international conference on signal processing and communication (ICSC), IEEE, 2019, pp. 158–164.

[63] L. Zhao, B. Ding, X.-Y. Qin, Z. Wang, W. Lv, Y.-B. He, Q.-H. Yang, F. Kang, Revisiting the roles of natural graphite in ongoing lithium-ion batteries, Advanced Materials 34 (18) (2022) 2106704.

[64] P. Pitfield, T. Brown, D. Rayner, Tungsten profile, British Geological Survey (2011).

[65] N. Krishna Rao, Beneficiation of tungsten ores in india: A review, Bulletin of Materials Science 19 (2) (1996) 201–265. doi:10.1007/BF02744666.

[66] G. N. Hounsfield, A method of and apparatus for examination of a body by radiation such as X-or gamma-radiation, British Patent No. 1,283,915 (1972).

[67] G. N. Hounsfield, Computerized transverse axial scanning (tomography). 1. description of system., British Journal of Radiology 552 (46) (1973) 1016–1022.

[68] W. A. Kalender, Computed tomography: fundamentals, system technology, image quality, applications, John Wiley & Sons, Hoboken, 2011.

[69] A. M. Petrovic, J. E. Siebert, P. E. Rieke, Soil bulk density analysis in three dimensions by computed tomographic scanning, Soil Science Society of America Journal 46 (3) (1982) 445–450. doi:10.2136/sssaj1982.03615995004600030001x.

[70] J. M. Hainsworth, L. A. Aylmore, The use of computer assisted tomography to determine spatial distribution of soil water content, Soil Research 21 (4) (1983) 435. doi:10.1071/SR9830435.

[71] J. R. Arnold, J. P. Testa, P. J. Friedman, G. X. Kambic, Computed tomographic analysis of meteorite inclusions, Science (New York, N.Y.) 219 (4583) (1983) 383–384. doi:10.1126/science.219.4583.383.

[72] H. J. Vinegar, S. L. Wellington, Tomographic imaging of three-phase flow experiments, Review of Scientific Instruments 58 (1) (1987) 96–107.

[73] S. L. Wellington, H. J. Vinegar, X-ray computerized tomography, Journal of Petroleum Technology 39 (08) (1987) 885–898. doi:10.2118/16983-pa.

[74] B. Haubitz, M. Prokop, W. Döhring, J. H. Ostrom, P. Wellnhofer, Computed tomography of archaeopteryx, Paleobiology 14 (2) (1988) 206–213. doi:10.1017/S0094837300011921.

[75] J. Kenter, Applications of computerized tomography in sedimentology, Mar. Geotechnol. 8 (3) (1989) 201–211. doi:10.1080/10641198909379868.

[76] J. C. Elliott, S. D. Dover, X-ray microtomography, Journal of Microscopy 126 (Pt 2) (1982) 211–213. doi:10.1111/j.1365-2818.1982.tb00376.x.

[77] J. C. Elliott, S. D. Dover, X-ray microscopy using computerized axial tomography, Journal of Microscopy 138 (Pt 3) (1985) 329–331. doi:10.1111/j.1365-2818.1985.tb02627.x.

[78] T. Sato, O. Ikeda, Y. Yamakoshi, M. Tsubouchi, X-ray tomography for microstructural objects, Applied Optics 20 (22) (1981) 3880–3883. doi:10.1364/AO.20.003880.

[79] A. Du Plessis, S. G. Le Roux, A. Guelpa, Comparison of medical and industrial X-ray computed tomography for non-destructive testing, Case Studies in Nondestructive Testing and Evaluation 6 (2) (2016) 17–25. doi:10.1016/j.csndt.2016.07.001.

[80] V. Cnudde, B. Masschaele, M. Dierick, J. Vlassenbroeck, L. van Hoorebeke, P. Jacobs, Recent progress in X-ray CT as a geosciences tool, Applied Geochemistry 21 (5) (2006) 826–832. doi:10.1016/j.apgeochem.2006.02.010.

[81] E. Rosenberg, R. Ferreira de Paiva, P. Guéroult, J. Lynch, Microtomography applications in rock analysis and related fields, Proceedings of the Deutsche Gesellscjaft für Zerstörungsfreie Prüfung-DGZfP (1999) 9–18.

[82] R. A. Ketcham, W. D. Carlson, Acquisition, optimization and interpretation of X-ray computed tomographic imagery: applications to the geosciences, Computers & Geosciences 27 (4) (2001) 381–400. doi:10.1016/S0098-3004(00)00116-3.

[83] R. D. Hanna, R. A. Ketcham, X-ray computed tomography of planetary materials: A primer and review of recent studies, Geochemistry 77 (4) (2017) 547–572. doi:10.1016/j.chemer.2017.01.006.

[84] F. Mees, R. Swennen, M. van Geet, P. Jacobs, Applications of X-ray computed tomography in the geosciences, Vol. 215 of Geological Society special publication, Geological Society Publishing House, 2003.

[85] B. Godel, High-resolution X-ray computed tomography and its application to ore deposits: from data acquisition to quantitative three-dimensional measurements with case studies from Ni-Cu-PGE deposits, Economic Geology 108 (8) (2013) 2005–2019. doi:10.2113/econgeo.108.8.2005.

[86] J. L. Mauk, J. R. Kyle, M. P. Simpson, P. Atkinson, Ore mineralogy of the BM37 shoot of the Karangahake deposit, Australian Journal of Mining and Metallurgy (2006) 233–242.

[87] M. Ferraz da Costa, J. R. Kyle, L. M. Lobato, R. A. Ketcham, R. C. Figueiredo e Silva, R. C. Fernandes, Orogenic gold ores in three-dimensions: A case study of distinct mineralization styles at the world-class Cuiabá deposit, Brazil, using high-resolution X-ray computed tomography on gold particles, Ore Geology Reviews 140 (3-4) (2022) 104584. doi:10.1016/j.oregeorev.2021.104584.

[88] J. Sittner, V. Brovchenko, A. Siddique, F. Buyse, M. Boone, A. D. Renno, V. Cnudde, Three-dimensional distribution of platinum group minerals in natural MSS-ISS ores from the Norilsk One deposit, Russia, Frontiers in Earth Science (2022). doi:10.3389/feart.2022.860751.

[89] L. E. Howard, P. Elangovan, S. C. Dominy, R. Armstrong, D. Hezel, R. L. Abel, Characterisation of gold ores by X-ray computed tomography – part 1: Software for calibration and quantification of mineralogical phases, in: Proceedings of the 1st AusIMM International Geometallurgy Conference, Brisbane 5 - 7 September 2011, 2011, pp. 321–330.

[90] S. C. Dominy, I. M. Platten, L. E. Howard, P. Elangovan, R. Armstrong, R. C.A. Minnitt, R. L. Abel, Characterisation of gold ores by X-ray computed tomography - part 2: applications to the determination of gold particle size and distribution, in: Proceedings of the 1st AusIMM International Geometallurgy Conference, Brisbane 5 - 7 September 2011, 2011, pp. 293–309.

[91] S. C. Dominy, I M Platten, R C A Minnitt, Determination of the sampling liberation diameter in a high-grade coarse gold ore by high-resolution X-ray computed tomography, Proceedings of the AusIMM Sampling Conference, Perth (Australia), 21-22 August 2012 (2012).

[92] S. C. Dominy, I. M. Platten, H. J. Glass, S. Purevgerel, B. W. Cuffley, Determination of gold particle characteristics for sampling protocol optimisation, Minerals 11 (10) (2021). doi:10.3390/min11101109.

[93] J. Chisambi, B. P. von der Heyden, M. Tshibalanganda, S. G. Le Roux, Gold exploration in two and three dimensions: Improved and correlative insights from microscopy and X-ray computed tomography, Minerals 10 (5) (2020). doi:10.3390/min10050476.

[94] S. Lohmeier, R. R. Gainov, A. Hodgkin, Morphological characterization of lode gold in the auriferous quartz veins at M'Popo mine, Angola, by computed tomography and optical microscopy, Applied Earth Science 132 (2) (2023) 65–89. doi:10.1080/25726838.2023.2219116.

[95] A. S. Mote, J. R. Kyle, R. A. Ketcham, M. D. Melker, M. J. Jahraus, T. R. Brown, T. F. Wawrzyniec, High resolution X-ray computed tomography investigations of high grade gold ore zones in the Cripple Creek District, Colorado, Proceedings of the Geological Society of Nevada Symposium: Window to the World, Reno, N.V. (2005) 1169–1175.

[96] D. Chetty, W. Clark, C. Bushell, T. P. Sebola, J. Hoffman, R. Nshimirimana, F. de Beer, The use of 3D X-ray computed tomography for gold location in exploration drill cores, in: M. A. Broekmans (Ed.), Proceedings of the 10th International Congress for Applied Mineralogy (ICAM), Springer Berlin Heidelberg, Berlin, Heidelberg, 2012, pp. 129–136. doi:10.1007/978-3-642-27682-817.

[97] L. Thormann, B. Buchspies, C. Mbohwa, M. Kaltschmitt, PGE production in southern Africa, part I: production and market trends, Minerals 7 (11) (2017). doi:10.3390/min7110224.

[98] D. I. Groves, R. J. Goldfarb, F. Robert, C. J. Hart, Gold deposits in metamorphic belts: overview of current understanding, outstanding problems, future research, and exploration significance, Economic Geology 98 (1) (2003) 1–29.

[99] Y. Ghorbani, M. Becker, J. Petersen, S. H. Morar, A. Mainza, J.-P. Franzidis, Use of X-ray computed tomography to investigate crack distribution and mineral dissemination in sphalerite ore particles, Minerals Engineering 24 (12) (2011) 1249–1257. doi:10.1016/j.mineng.2011.04.008.

[100] L. C. Bam, J. A. Miller, M. Becker, I. J. Basson, X-ray computed tomography: Practical evaluation of beam hardening in iron ore samples, Minerals Engineering 131 (2019) 206–215. doi:10.1016/j.mineng.2018.11.010.

[101] J. Ricardo Assuncao Godinho, S. Gupta, C. Guimaraes da Silva Tochtrop, R. Demanou Tekeng, M. Hicks, D. Ebert, J. Ihanus, A. Roine, J. Liipo, A. D. Renno, Quantitative 3D characterization of chromite ore particles, Minerals Engineering 204 (2023) 108403. doi:https://doi.org/10.1016/j.mineng.2023.108403.
URL https://www.sciencedirect.com/science/article/pii/S089268752300417X

[102] O. Popov, I. Talovina, H. Lieberwirth, A. Duryagina, Quantitative microstructural analysis and X-ray computed tomography of ores and rocks—comparison of results, Minerals 10 (2) (2020).

[103] L. Y. Le Bras, R. Bolhar, L. Bam, B. M. Guy, G. M. Bybee, P. A. Nex, Three-dimensional textural investigation of sulfide mineralisation from the loolekop carbonatite–phoscorite polyphase intrusion in the Phalaborwa Igneous Complex (South Africa), with implications

for ore-forming processes, Mineralogical Magazine 85 (4) (2021) 514–531. doi:10.1180/mgm.2021.32.

[104] M. J. Berger, J. H. Hubbell, S. M. Seltzer, J. Chang, J. S. Coursey, R. Sukumar, D. S. Zucker, K. Olsen, X-COM: Photon cross sections database (2010).

[105] F. Buyse, S. Dewaele, M. N. Boone, V. Cnudde, Combining automated mineralogy with X-ray computed tomography for internal characterization of ore samples at the microscopic scale, Natural Resources Research 32 (2) (2023) 461–478. doi:10.1007/s11053-023-10161-z.

[106] L. C. Bam, J. A. Miller, M. Becker, A mineral X-ray linear attenuation coefficient tool (MXLAC) to assess mineralogical differentiation for X-ray computed tomography scanning, Minerals 10 (5) (2020). doi:10.3390/min10050441.

[107] M. Voigt, J. A. Miller, A. N. Mainza, L. C. Bam, M. Becker, The robustness of the gray level co-occurrence matrices and X-ray computed tomography method for the quantification of 3D mineral texture, Minerals 334 (10) (2020). doi:10.3390/min10040334.

[108] R. L. Moore, A. Patera, A. Bonnin, B. Ménez, Grating-based X-ray computed tomography for improved contrast on a heterogeneous geomaterial, Frontiers in Earth Science 10 (2022) 69. doi:10.3389/feart.2022.878738.

[109] J. R. A. Godinho, G. Westaway-Heaven, M. A. Boone, A. D. Renno, Spectral tomography for 3D element detection and mineral analysis, Minerals 11 (6) (2021). doi:10.3390/min11060598.

[110] J. Sittner, J. R. A. Godinho, A. D. Renno, V. Cnudde, M. Boone, T. de Schryver, D. van Loo, M. Merkulova, A. Roine, J. Liipo, Spectral X–ray computed micro tomography: 3–dimensional chemical imaging, X-Ray Spectrometry 50 (2) (2021) 92–105. doi:10.1002/xrs.3200.

[111] M. Martini, P. Francus, L. Di Schiavi Trotta, P. Després, Identification of common minerals using stoichiometric calibration method for dual–energy CT, Geochemistry, Geophysics, Geosystems 22 (11) (2021) 225. doi:10.1029/2021GC009885.

[112] B. Schmidt, T. Flohr, Principles and applications of dual source CT, Physica Medica 79 (2020) 36–46. doi:10.1016/j.ejmp.2020.10.014.

[113] A. Rozendaal, S. G. Le Roux, A. Du Plessis, C. Philander, Grade and product quality control by microCT scanning of the world class namakwa sands Ti-Zr placer deposit West Coast, South Africa: An orientation study, Minerals Engineering 116 (2018) 152–162. doi:10.1016/j.mineng.2017.09.001.

[114] Q. Lin, D. J. Barker, K. J. Dobson, P. D. Lee, S. J. Neethling, Modelling particle scale leach kinetics based on X-ray computed micro-tomography images, Hydrometallurgy 162 (2) (2016) 25–36. doi:10.1016/j.hydromet.2016.02.008.

[115] M. Warlo, G. Bark, C. Wanhainen, A. R. Butcher, F. Forsberg, H. Lycksam, J. Kuva, Multi-scale X-ray computed tomography analysis to aid automated mineralogy in ore geology research, Frontiers in Earth Sciences 9 (2021) 789372.

[116] Y. Wang, C. Lin, J. Miller, 3D image segmentation for analysis of multisize particles in a packed particle bed, Powder Technology 301 (2016) 160–168.

[117] Y. Wang, C. Lin, J. Miller, Quantitative analysis of exposed grain surface area for multiphase particles using x-ray microtomography, Powder Technology 308 (2017) 368–377.

[118] F. Reyes, Q. Lin, O. Udoudo, P. D. Lee, S. J. Neethling, Calibrated X-ray micro-tomography for mineral ore quantification, Minerals Engineering 110 (2017) 122–130. doi:10.1016/j.mineng.2017.04.015.

[119] P. I. Guntoro, G. Tiu, Y. Ghorbani, C. Lund, J. Rosenkranz, Application of machine learning techniques in mineral phase segmentation for X-ray microcomputed tomography (μCT) data, Minerals Engineering 142 (2019) 105882.

[120] M. Ghadiri, S. T. Harrison, M. A. Fagan-Endres, Quantitative X-ray μct measurement of the effect of ore characteristics on non-surface mineral grain leaching, Minerals 10 (9) (2020) 746.

[121] P. I. Guntoro, Y. Ghorbani, M. Parian, A. R. Butcher, J. Kuva, J. Rosenkranz, Development and experimental validation of a texture-based 3D liberation model, Minerals Engineering 164 (2021) 106828.

[122] P. I. Guntoro, Y. Ghorbani, A. R. Butcher, J. Kuva, J. Rosenkranz, Textural quantification and classification of drill cores for geometallurgy: Moving toward 3D with X-ray microcomputed tomography (μct), Natural Resources Research 29 (2020) 3547–3565.

[123] D. D. L. Chung, Review graphite, Journal of Materials Science 37 (8) (2002) 1475–1489. doi:10.1023/A:1014915307738.

[124] H. O. Pierson, Handbook of carbon, graphite, diamonds and fullerenes: processing, properties and applications, William Andrew, 2012.

[125] C. A. Bessel, K. Laubernds, N. M. Rodriguez, T. K. Baker, Graphite nanofibers as an electrode for fuel cell applications, The Journal of Physical Chemistry B 105 (6) (2001) 1115–1118. doi:10.1021/jp003280d.

[126] U.S. Geological Survey, List of critical minerals (2022).
URL https://www.usgs.gov/news/national-news-release/usgeological-survey-releases-2022-list-critical-minerals

[127] USGS, Mineral commodity summaries: graphite (2022).
URL https://hcss.nl/wp-content/uploads/2022/03/Graphite-HCSS-2022.pdf

[128] G. J. Simandl, S. Paradis, Graphite deposit types, their origin, and economic significance, British Columbia Ministry of Energy and Mines & British Colombia Geological Survey 3 (2015) 163–171.

[129] F. J. Luque, J.-M. Huizenga, E. Crespo-Feo, H. Wada, L. Ortega, J. F. Barrenechea, Vein graphite deposits: Geological settings, origin, and economic significance, Mineralium Deposita 49 (2) (2014) 261–277. doi:10.1007/s00126-013-0489-9.

[130] S. Chehreh Chelgani, M. Rudolph, R. Kratzsch, D. Sandmann, J. Gutzmer, A review of graphite beneficiation techniques, Mineral Processing and Extractive Metallurgy Review 37 (1) (2016) 58–68. doi:10.1080/08827508.2015.1115992.

[131] S. Damm, Rohstoffrisikobewertung - Graphit, Vol. 51 of DERA-Rohstoffinformationen, Deutsche Rohstoffagentur (DERA) in der Bundesanstalt für Geowissenschaften und Rohstoffe (BGR), Berlin, 2021.

[132] B. Moradi, G. G. Botte, Recycling of graphite anodes for the next generation of lithium ion batteries, Journal of Applied Electrochemistry 46 (2) (2016) 123–148. doi:10.1007/s10800-015-0914-0.

[133] H. G. Dill, J. Kus, S. Goldmann, I. Suárez-Ruiz, T. Neumann, S. Kaufhold, The physical-chemical regime of a sulfide-bearing semi-graphite mineral assemblage in metabasic rocks (SE Germany) – a multidisciplinary study of the missing link between impsonite and graphite, International Journal of Coal Geology 214 (245406) (2019) 103262. doi:10.1016/j.coal.2019.103262.

[134] E. Crespo, F. J. Luque, J. F. Barrenechea, M. Rodas, Influence of grinding on graphite crystallinity from experimental and natural data: Implications for graphite thermometry and sample preparation, Mineralogical Magazine 70 (6) (2006) 697–707. doi:10.1180/0026461067060358.

[135] D. Sandmann, S. Haser, J. Gutzmer, Characterisation of graphite by automated mineral liberation analysis, Mineral Processing and Extractive Metallurgy 123 (3) (2014) 184–189. doi:10.1179/1743285514Y.0000000063.

[136] T. Al-Ani, S. Leinonen, T. Ahtola, D. Salvador, High-grade flake graphite deposits in metamorphic schist belt, central Finland—mineralogy and beneficiation of graphite forlithium-ion battery applications, Minerals 10 (8) (2020) 680. doi:10.3390/min10080680.

[137] A. Scogings, Graphite: Where size matters, Australia's Paydirt (2015).

[138] D. A. Jerram, A. Mock, G. R. Davis, M. Field, R. J. Brown, 3D crystal size distributions: A case study on quantifying olivine populations in kimberlites, Lithos 112 (2009) 223–235. doi:10.1016/j.lithos.2009.05.042.

[139] D. A. Jerram, M. D. Higgins, 3D analysis of rock textures: quantifying igneous microstructures, Elements 3 (4) (2007) 239–245. doi:10.2113/gselements.3.4.239.

[140] G. A. Gualda, M. Rivers, Quantitative 3D petrography using X-ray tomography: Application to Bishop Tuff pumice clasts, Journal of Volcanology and Geothermal Research 154 (1-2) (2006) 48–62.

[141] L. Vásrhelyi, Z. Kónya, Á. Kukovecz, R. Vajtai, Microcomputed tomography-based characterization of advanced materials: a review, Materials Today Advances 8 (2020) 100084. doi:10.1016/j.mtadv.2020.100084.

[142] Z.-H. Zhou, Machine learning, Springer Nature, 2021.

[143] L. Breiman, Random forests, Machine Learning 45 (1) (2001) 5–32.

[144] O. Ronneberger, P. Fischer, T. Brox, U-net: Convolutional networks for biomedical image segmentation, in: N. Navab, J. Hornegger, W. M. Wells, A. F. Frangi (Eds.), Medical Image Computing and Computer-Assisted Intervention – MICCAI 2015, Springer International Publishing, 2015, pp. 234–241.

[145] A. Novikov, D. Major, M. Wimmer, D. Lenis, K. Bühler, Deep sequential segmentation of organs in volumetric medical scans, IEEE Transactions on Medical Imaging 38 (5) (2019) 1207–1215. doi:10.1109/TMI.2018.2881678.

[146] X. Zhang, L. Y. Zhang, Y. S. Qiu, X. Qu, Beneficiation of a low-grade flaky graphite ore from Australia by flotation, Advanced Materials Research 1090 (2015) 188–192. doi:10.4028/www.scientific.net/AMR.1090.188.

[147] C. J. Mitchell, Flake graphite, British Geological Society (1993).

[148] B. G. Kim, s. K. Choi, C. L. Park, H. S. Chung, H. S. Jeon, Inclusion of gangue mineral and its mechanical separation from expanded graphite, Particulate Science and Technology 21 (4) (2003) 341–351. doi:10.1080/716100574.

[149] R. A. Ketcham, Accurate three-dimensional measurements of features in geological materials from X-ray computed tomography data, in: Desrues, J.,Viggiani, G., Bésuelle, P. (Ed.), Advances in X-ray Tomography for Geomaterials, 2006, pp. 143–148. doi:10.1002/9780470612187.ch9.

[150] D. N. Sutherland, P. Gottlieb, Application of automated quantitative mineralogy in mineral processing, Minerals Engineering Vol. 4 (753-762) (1991). doi:10.1016/0892-6875(91)90063-2.

[151] S. J. B. Reed, Electron microprobe analysis and scanning electron microscopy in geology, Cambridge University Press, 2005.

[152] Y. Liu, Z. Hu, M. Li, S. Gao, Applications of LA-ICP-MS in the elemental analyses of geological samples, Chinese Science Bulletin 58 (32) (2013) 3863–3878. doi:10.1007/s11434-013-5901-4.

[153] B. Lavina, P. Dera, R. T. Downs, Modern X-ray diffraction methods in mineralogy and meosciences, Reviews in Mineralogy and Geochemistry 78 (1) (2014) 1–31. doi:10.2138/rmg.2014.78.1.

[154] F. Reyes, J. J. Lin, S. J. Neethling, Quantifying mineral liberation by particle grade and surface exposure using x-ray microct, Minerals Engineering 125 (2018) 75–82. doi:10.1016/j.mineng.2018.05.028.

[155] T. Ueda, T. Oki, S. Koyanaka, Stereological bias for spherical particles with various particle compositions, Advanced Powder Technology 27 (4) (2016) 1828–1838. doi:10.1016/j.apt.2016.06.016.

[156] T. Ueda, T. Oki, S. Koyanaka, Experimental analysis of mineral liberation and stereological bias based on X-ray computed tomography and artificial binary particles, Advanced Powder Technology 29 (23) (2018) 462–470. doi:10.1016/j.apt.2017.11.004.

[157] A. Jansson, L. Pejryd, A dual-energy approach for improvement of the measurement consistency in computed tomography, Measurement Science and Technology 27 (11) (2016) 115013. doi:10.1088/0957-0233/27/11/115013.

[158] N. Grozmani, D. Chupina, B. Montavon, R. H. Schmitt, Sinogram interpretability based CT artefact reduction for multi-material workpieces, Nondestructive Testing and Evaluation 37 (5) (2022) 679–691. doi:10.1080/10589759.2022.2091134.

[159] R. Garnett, A comprehensive review of dual-energy and multi-spectral computed tomography, Clinical Imaging 67 (2020) 160–169. doi:10.1016/j.clinimag.2020.07.030.

[160] L. Martin, A. Tuysuzoglu, W. C. Karl, P. Ishwar, Learning-based object identification and segmentation using dual-energy CT images for security, IEEE Transactions on Image Processing (Volume 24 // 11) (2015). doi:10.1109/TIP.2015.2456507.

[161] J. Leisner, C. Bauer, R. Wagner, Circular economy: Material sorting in waste streams using dual energy x-ray transmission, in: Proceedings of the 8th International Conference on Sensors and Electronics Instrumentation Advances (SEIA'2022), 2022, pp. 93–96.

[162] S. Chen, X. Zhong, S. Dorn, N. Ravikumar, Q. Tao, X. Huang, M. Lell, M. Kachelriess, A. Maier, Improving generalization capability of multiorgan segmentation models using dual-energy CT, IEEE Transactions on Radiation and Plasma Medical Sciences 6 (1) (2022) 79–86. doi:10.1109/TRPMS.2021.3055199.

[163] J. G. Fletcher, N. Takahashi, R. Hartman, L. Guimaraes, J. E. Huprich, D. M. Hough, L. Yu, C. H. McCollough, Dual-energy and dual-source CT: Is there a role in the abdomen and pelvis?, Radiologic Clinics of North Ameria 47 (1) (2009) 41–57. doi:10.1016/j.rcl.2008.10.003.

[164] H. Scheffel, P. Stolzmann, T. Frauenfelder, T. Schertler, L. Desbiolles, S. Leschka, B. Marincek, H. Alkadhi, Dual-energy contrast-enhanced computed tomography for the detection of urinary stone disease, Investigative Radiology 42 (12) (2007) 823–829. doi:10.1097/RLI.0b013e3181379bac.

[165] F. F. Behrendt, B. Schmidt, C. Plumhans, S. Keil, S. G. Woodruff, D. Ackermann, G. Mühlenbruch, T. Flohr, R. W. Günther, A. H. Mahnken, Image fusion in dual energy computed tomography, Investigative Radiology 44 (1) (2009). doi:10.1097/RLI.0b013e31818c3d4b.

[166] J. Fornaro, S. Leschka, D. Hibbeln, A. Butler, N. Anderson, G. Pache, H. Scheffel, S. Wildermuth, H. Alkadhi, P. Stolzmann, Dual- and multi-energy CT: approach to functional imaging, Insights Imaging 2 (2011). doi:10.1007/s13244-010-0057-0.

[167] H. Alves, I. Lima, R. T. Lopes, Methodology for attainment of density and effective atomic number through dual energy technique using microtomographic images, Applied Radiation and Isotopes 89 (2014) 6–12. doi:10.1016/j.apradiso.2014.01.018.

[168] H. Alves, I. Lima, J. T. de Assis, A. A. Neves, R. T. Lopes, Mineralogy evaluation and segmentation using dual-energy microtomography, X-Ray Spectrometry 44 (3) (2015) 99–104. doi:10.1002/xrs.2582.

[169] S. R. Stock, Microcomputed tomography: methodology and applications, second edition Edition, CRC Press, Boca Raton, FL 33487-2742, 2019. doi:10.1201/9780429186745.

[170] A. Kraemer, E. Kovacheva, G. Lanza, Projection based evaluation of CT image quality in dimensional metrology, e-Journal of Nondestructive Testing 20 (8) (2015).
URL https://www.ndt.net/search/docs.php3?id=18024

[171] A. Du Plessis, M. Tshibalanganda, S. G. Le Roux, Not all scans are equal: X-ray tomography image quality evaluation, Materials Today Communications 22 (2020) 100792. doi:10.1016/j.mtcomm.2019.100792.

[172] M. Reiter, D. Weiß, C. Gusenbauer, M. Erler, C. Kuhn, S. Kasperl, J. Kastner, Evaluation of a histogram-based image quality measure for X-ray computed tomography, e-Journal of Nondestructive Testing 19 (6) (2014).
URL https://www.ndt.net/?id=15715

[173] A. A. Markowicz, X-ray physics: handbook of X-ray spectrometry, Marcel Dekker, Inc., New York, 1993.

[174] J. A. Seibert, X-ray imaging physics for nuclear medicine technologists. part 1: Basic principles of X-ray production, Journal of Nuclear Medicine Technology 32 (3) (2004) 139–147.
URL https://tech.snmjournals.org/content/32/3/139.short

[175] R. H. Schmitt, A. Buratti, N. Grozmani, C. Voigtmann, M. Peterek, Model-based optimisation of CT imaging parameters for dimensional measurements on multimaterial workpieces, CIRP Annals 67 (1) (2018) 527–530.

[176] V. Kovalevsky, Modern algorithms for image processing, Apress, Berkeley, CA, 2019. doi:10.1007/978-1-4842-4237-7.

[177] R. C. Gonzalez, R. E. Woods, Digital image processing, 4th Edition, Pearson, 330 Hudson Street, New York, NY 10013, 2017.

[178] R. B. Sandler, Tungsten, U.S. Geological Survey, Reston, VA, USA (2023).

[179] A. Hughes, Australian resource reviews, Geoscience Australia, Canberra (2020).

[180] R. Todesco, The tungsten revival, Mining Magazine (21.11.2023).
URL https://miningmagazine.com.au/the-tungsten-revival/

[181] A. R. Butcher, Q. Dehaine, A. H. Menzies, S. P. Michaux, Characterisation of ore properties for geometallurgy, Elements 19 (6) (2023) 352–358. doi:10.2138/gselements.19.6.352.

[182] Q. Zhan, X.-Y. Gao, L. Meng, T.-P. Zhao, Ore genesis and fluid evolution of the sandaozhuang supergiant W-Mo skarn deposit, southern margin of the North China Craton: Insights from scheelite, garnet and clinopyroxene geochemistry, Ore Geology Reviews 139 (3) (2021) 104551.

[183] S. G. Soloviev, Geology, mineralization, and fluid inclusion characteristics of the kumbel oxidized W–Cu–Mo skarn and Au–W stockwork deposit in Kyrgyzstan, Tien Shan, Mineralium Deposita 50 (2) (2015) 187–220. doi:10.1007/s00126-014-0531-6.

[184] L. Krebbers, Gainov, Ramil, B.G. Lottermoser, A. H. Stephanie Lohmeier, Applications of industrial computed tomography in the mining sector, Mining Report: Glückauf! 157 (4) (2021).

[185] P. I. Guntoro, X-ray microcomputed tomography (μCT) as a potential tool in geometallurgy, University of Lulea, 2019.

[186] D. E. Barret, Geology, mineralogy and conditions of formation of the Kara scheelite skarn, Hobart, University of Tasmania, 1980.

[187] A. D. Fudge, Kara no. 1 magnetite deposit ore reserve report January 2016.

[188] T. Callaghan, Kara no. 1 mineral resource estimate.

[189] K. Zaw, B. Singoyi, Formation of magnetite-scheelite skarn mineralization at Kara, northwestern Tasmania: evidence from mineral chemistry and stable isotopes, Economic Geology (95) (2000) 1215–1230.

[190] B. Singoyi, K. Zaw, A petrological and fluid inclusion study of magnetite–scheelite skarn mineralization at Kara, northwestern Tasmania: implications for ore genesis, Chemical Geology 173 (2001) 239–253.

[191] Collins, P.L.F., Brown, S.G., Dronseika, E.V., Morland, R., Mid-paleozoic ore deposits, Geological Society of Australia Special Publication 10 (1989) 270–292.

[192] M. R. Banks, P. W. Baillie, Late Cambrian to Devonian, in: Geology and mineral resources of Tasmania, Vol. 15, Geological Society of Australia, 1989, pp. 182–237.

[193] D. E. Leaman, R. G. Richardson, Production of a residual gravity field map for tasmania and some implications, Exploration Geophysics 20 (1-2) (1989) 181–184.

[194] E. Williams, McClenaghan, M.P., Collins, P.L.D., mid-paleozoic deformaiton, granitoid and ore deposits, Geological Society of Australia Special Publication, v. 15 (1989) 238–292.

[195] R. F. Berry, The history of movement on the Henty Fault Zone, western Tasmania: An analysis of fault striations, Australian Journal of Earth Sciences 36 (2) (1989) 189–205. doi:10.1080/08120098908729481.

[196] X. Yang, Beneficiation studies of tungsten ores – a review, Minerals Engineering 125 (6) (2018) 111–119. doi:10.1016/j.mineng.2018.06.001.

[197] R. Sivamohan, E. Forssberg, Recovery of heavy minerals from slimes, International Journal of Mineral Processing 15 (4) (1985) 297–314. doi:10.1016/0301-7516(85)90047-X.

[198] J. Y. Huang, J. R. Kerns, J. L. Nute, X. Liu, P. A. Balter, F. C. Stingo, D. S. Followill, D. Mirkovic, R. M. Howell, S. F. Kry, An evaluation of three commercially available metal artifact reduction methods for CT imaging, Physics in Medicine & Biology 60 (3) (2015) 1047.

[199] B. De Man, J. Nuyts, P. Dupont, G. Marchal, P. Suetens, Metal streak artifacts in X-ray computed tomography: a simulation study, IEEE Transactions on Nuclear Science 46 (3) (1999) 691–696. doi:10.1109/23.775600.

[200] G. Van Gompel, K. Joost Batenburg, E. Van de Casteele, W. van Aarle, J. Sijbers, A discrete tomography approach for superresolution micro-CT images: application to bone, in: 2010 IEEE International Symposium on Biomedical Imaging: From Nano to Macro, 2010, pp. 816–819. doi:10.1109/ISBI.2010.5490111.

[201] M. Krumm, S. Kasperl, M. Franz, Reducing non-linear artifacts of multi-material objects in industrial 3D computed tomography, NDT & E International 41 (4) (2008) 242–251. doi:https://doi.org/10.1016/j.ndteint.2007.12.001.

[202] J. Lifton, Multi-material linearization beam hardening correction for computed tomography, Journal of X-ray Science and Technology 25 (4) (2017) 629–640.

[203] J. A. Meganck, K. M. Kozloff, M. M. Thornton, S. M. Broski, S. A. Goldstein, Beam hardening artifacts in micro-computed tomography scanning can be reduced by X-ray beam filtration and the resulting images can be used to accurately measure BMD, Bone 45 (6) (2009) 1104–1116. doi:https://doi.org/10.1016/j.bone.2009.07.078.

[204] O. W. Hamer, C. B. Sirlin, M. Strotzer, I. Borisch, N. Zorger, S. Feuerbach, M. Volk, Chest radiography with a flat-panel detector: image quality with dose reduction after copper filtration, Radiology 237 (2) (2005) 691–700.

[205] G. Grodstein, X-ray attenuation coefficients from 10 Kev to 100 Mev, Circular (United States), U.S. Department of Commerce, National Bureau of Standards, 1957.

[206] O. Brunke, E. Neuser, A. Suppes, High resolution industrial CT systems: advances and comparison with synchrotron-based ct, in: International symposium on digital industrial radiology and computed tomography, Vol. 20, 2011, pp. 1–9.

[207] A. Buratti, N. Grozmani, C. Voigtmann, L. Sartori, R. Schmitt, Determination of the optimal imaging parameters in industrial computed tomography for dimensional measurements on monomaterial workpieces, Measurement Science and Technology 29 (11) (2018) 115009.

[208] W. A. Kalender, Y. Kyriakou, Flat-detector computed tomography (FD-CT), European radiology 17 (2007) 2767–2779.

[209] L. Rigon, E. Vallazza, F. Arfelli, R. Longo, D. Dreossi, A. Bergamaschi, B. Schmitt, R. Chen, M. A. Cova, R. Perabò, Synchrotron-radiation microtomography for the non-destructive structural evaluation of bowed stringed instruments, E-Preserv. Sci 7 (2010) 71–77.

[210] E. H. Cooperdock, F. Hofmann, R. M. Tibbetts, A. Carrera, A. Takase, A. J. Celestian, Rapid phase identification of apatite and zircon grains for geochronology using X-ray micro-computed tomography, Geochronology 4 (2) (2022) 501–515.

[211] J. F. Barrett, N. Keat, Artifacts in CT: recognition and avoidance, Radiographics 24 (6) (2004) 1679–1691.

[212] H. Villarraga-Gómez, A. Amirkhanov, C. Heinzl, S. T. Smith, Assessing the effect of sample orientation on dimensional X-ray computed tomography through experimental and simulated data, Measurement 178 (2021) 109343. doi:https://doi.org/10.1016/j.measurement.2021.109343.

[213] H. Gautneb, J. S. Rønning, A. K. Engvik, I. H. Henderson, B. E. Larsen, J. K. Solberg, F. Ofstad, J. Gellein, H. Elvebakk, B. Davidsen, The graphite occurrences of northern Norway, a review of geology, geophysics, and resources, Minerals 10 (7) (2020) 626. doi:10.3390/min10070626.

[214] S. Hongjuan, P. Tongjiang, L. Bo, M. Caifeng, L. Liming, W. Quanjun, D. Jiaqi, L. Xiaoyi, Study of oxidation process occurring in natural graphite deposits, RSC Advances 7 (81) (2017) 51411–51418. doi:10.1039/C7RA10327A.

[215] A. Badran, D. Marshall, R. Makovetsky, B. Provencher, N. Piché, M. Marsh, Automated segmentation of computed tomography images of fiber-reinforced composites by deep learning, Journal of Materials Science 55 (2020) 16273–16289.

[216] A. J. Enríquez-León, T. D. de Souza, F. T. S. Aragão, D. Braz, A. M. B. Pereira, L. P. Nogueira, Determination of the air void content of asphalt concrete mixtures using artificial intelligence techniques to segment micro-CT images, International Journal of Pavement Engineering 23 (11) (2022) 3973–3982.

[217] L. Bam, J. Miller, M. Becker, F. De Beer, I. Basson, X-ray computed tomography–determination of rapid scanning parameters for geometallurgical analysis of iron ore, in: Proceedings of the 3rd International Geometallurgy Conference, Perth, 15 -16 June 2016, 2016, pp. 209–219.

[218] Y. Qian, Development of image processing strategies for the quantitative analysis of CT datasets, Master thesis, RWTH Aachen University, 2024.

[219] Y. Jusman, A. Pusparini, A. N. Nazilah Chamim, S. N. A. M. Kanafiah, Comparison of malaria parasite image segmentation algorithm using thresholding and watershed method, Journal of Physics: Conference Series 1783 (1) (2021) 012092. doi:10.1088/1742-6596/1783/1/012092.

[220] N. Salem, N. M. Sobhy, M. E. Dosoky, A comparative study of white blood cells segmentation using otsu threshold and watershed transformation, Journal of Biomedical Engineering and Medical Imaging 3 (3) (2016). doi:10.14738/jbemi.33.2078.

[221] R. Fandrich, Y. Gu, D. Burrows, K. Moeller, Modern SEM-based mineral liberation analysis, International Journal of Mineral Processing 84 (1) (2007) 310–320, special Issue To Honor The Late Professor R. Peter King. doi:https://doi.org/10.1016/j.minpro.2006.07.018.
URL https://www.sciencedirect.com/science/article/pii/S0301751606001621

[222] P. Zhang, Y. I. Lee, J. Zhang, A review of high-resolution X-ray computed tomography applied to petroleum geology and a case study, Micron 124 (2019) 102702. doi:https://doi.org/10.1016/j.micron.2019.102702.
URL https://www.sciencedirect.com/science/article/pii/S0968432819301313

[223] C. Lund, P. Lamberg, Geometallurgy–a tool for better resource efficiency, European Geologist 37 (2014) 39–43.

[224] S. C. Dominy, L. O'Connor, A. Parbhakar-Fox, H. J. Glass, S. Purevgerel, Geometallurgy—a route to more resilient mine operations, Minerals 8 (12) (2018) 560.

[225] K. G. van den Boogaart, R. Tolosana-Delgado, Predictive geometallurgy: an interdisciplinary key challenge for mathematical geosciences, Handbook of Mathematical Geosciences: Fifty Years of IAMG (2018) 673–686doi:10.1007/978-3-319-78999-6_33.

[226] A. R. Butcher, Q. Dehaine, A. H. Menzies, S. P. Michaux, Characterisation of ore properties for geometallurgy, Elements 19 (6) (2023) 352–358.

[227] L. Pereira, E. Schach, R. Tolosana-Delgado, M. Frenzel, All about particles: modelling ore behaviour in mineral processing, Elements 19 (6) (2023) 359–364.

[228] J. Jeswiet, A. Szekeres, Energy consumption in mining comminution, Procedia CIRP 48 (2016) 140–145.

[229] T. Vizcarra, S. Harmer, E. Wightman, N. Johnson, E. Manlapig, The influence of particle shape properties and associated surface chemistry on the flotation kinetics of chalcopyrite, Minerals Engineering 24 (8) (2011) 807–816.

[230] J. R. A. Godinho, A. Hassanzadeh, T. Heinig, 3D quantitative mineral characterization of particles using X-ray computed tomography, Natural Resources Research 32 (2) (2023) 479–499. doi:10.1007/s11053-023-10169-5.

[231] J. Miller, C. Lin, Three-dimensional analysis of particulates in mineral processing systems by cone beam x-ray microtomography, Mining, Metallurgy & Exploration 21 (3) (2004) 113–124.

[232] Y. Zhang, N. Francois, L. Deakin, A. Barron, C. Evans, S. Bensley, P. D. Lösel, N. Kandula, R. Henley, M. Knackstedt, Improved particle separation, characterisation and analysis for ore beneficiation studies using 3D X-ray micro-computed tomography, Minerals Engineering 216 (2024) 108835. doi:https://doi.org/10.1016/j.mineng.2024.108835.

[233] Y. Zhang, N. Francois, R. W. Henley, L. Knuefing, M. Turner, M. Saadatfar, F. Brink, M. Knackstedt, In-situ study of texture-breakage coupling in a copper ore using X-ray micro-CT, Minerals Engineering 205 (2024) 108464. doi:https://doi.org/10.1016/j.mineng.2023.108464.
URL https://www.sciencedirect.com/science/article/pii/S0892687523004788

[234] A. Siddique, J. R. Godinho, J. Sittner, L. Pereira, Overcoming stereological bias: A workflow for 3D mineral characterization of particles using X-ray micro-computed tomography, Minerals Engineering 201 (10) (2023). doi:10.1016/j.mineng.2023.108200.

[235] M. Bergqvist, E. Landström, S. Luth, Access to geological structures, density, minerals and textures through novel combination of 3D tomography, XRF and sample weight, ASEG Extended Abstracts 2019 (1) (2019) 1–3. doi:10.1080/22020586.2019.12073146.

[236] Orexplore Technologie AB, Geocore X10, accessed: 2024-08-28.
URL https://www.orexplore.com/

[237] M.-E. Cioacă, M. Munteanu, E. P. Lynch, N. Arvanitidis, M. Bergqvist, G. Costin, D. Ivanov, V. Milu, R. Arvidsson, A. Iorga-Pavel, K. Högdahl, V. Stoilov, Mineralogical setting of precious metals at the assarel porphyry copper-gold deposit, Bulgaria, as supporting

information for the development of new drill core 3D XCT-XRF scanning technology, Minerals 10 (11) (2020). doi:10.3390/min10110946.

[238] S. Luth, F. Sahlström, M. Bergqvist, A. Hansson, E. P. Lynch, S. Sädbom, E. Jonsson, S. S. Andersson, N. Arvanitidis, Combined X-ray computed tomography and X-ray fluorescence drill core scanning for 3-D rock and ore characterization: Implications for the Lovisa stratiform Zn-Pb deposit and its structural setting, Bergslagen, Sweden, Economic Geology 117 (6) (2022) 1255–1273.

[239] F. Buyse, S. Dewaele, M. N. Boone, V. Cnudde, Contribution of 3D automated mineralogy in unraveling the formation history of Nb-Ta-Sn mineralized LCT pegmatites in the Karagwe-Ankole belt (central Africa), Geologica Belgica 27 (1-2) (2024) 1–14. doi:10.20341/gb.2024.001.

[240] L. Sun, C.-P. Xu, K.-Y. Xiao, Y.-S. Zhu, L.-y. Yan, Geological characteristics, metallogenic regularities and the exploration of graphite deposits in China, China Geology 1 (3) (2018) 424–433. doi:10.31035/cg2018044.

[241] Y. Ma, Y. Huang, L. Liu, Genesis of the Tianping flake graphite deposit at the western margin of Yangtze Block, SW China, Ore Geology Reviews 139 (1) (2021) 104434. doi:10.1016/j.oregeorev.2021.104434.

[242] J. Palosaari, R.-M. Latonen, J.-H. Smått, S. Raunio, O. Eklund, The flake graphite prospect of Piippumäki—an example of a high-quality graphite occurrence in a retrograde metamorphic terrain in Finland, Mineralium Deposita 55 (8) (2020) 1647–1660. doi:10.1007/s00126-020-00971-z.

[243] A. Butcher, Upscaling of 2D mineralogical information to 3D volumes for geoscience applications using a multi-scale, multi-modal and multi-dimensional approach, in: IOP Conference Series: Materials Science and Engineering, no. 1, IOP Publishing, 2020, p. 012006.

[244] E. Naumov, Y. Kalinin, G. Palyanova, L. Kryuchkova, V. Voitenko, V. Abramova, F. Pirajno, Combined study of Au-bearing arsenopyrite of orogenic gold deposits (NE Asia): high resolution 3D X-ray computed tomography, LA-ICP-MS, EMPA data, Geoscience Frontiers (2024) 101953doi:https://doi.org/10.1016/j.gsf.2024.101953.

[245] C. Siégel, L. Schoneveld, C. Spaggiari, M. L. Vaillant, S. Barnes, B. Godel, D. Mahon, L. Martin, S. Caruso, T. Shelton, A newly recognised mafic sill-hosted Ni-sulfide deposit emplaced during the 2.4 ga Widgiemooltha dike swarm event, Eastern Goldfields, Western Australia, Mineralium Deposita (2024) 1432–1866doi:10.1007/s00126-024-01305-z. URL https://www.sciencedirect.com/science/article/pii/S1674987124001774

[246] B. Wei, C. Y. Wang, Y. Cao, J. Wang, In-situ study of texture-breakage coupling in a copper ore using X-ray micro-CT, Mineralium Deposita (2024) 1432–1866doi:10.1007/s00126-024-01296-x.

[247] J. Wang, M. Wang, B. Wei, In situ crystallization of Fe-Ti oxides in the panzhihua layered intrusion, SW China: constraints from crystal size distribution and high-resolution X-ray computed tomography analyses, Journal of Asian Earth Sciences 257 (2023) 105858. doi:

https://doi.org/10.1016/j.jseaes.2023.105858.
URL https://www.sciencedirect.com/science/article/pii/S136791202300319X

[248] H. Rahman, A. R. Khan, T. Sadiq, A. H. Farooqi, I. U. Khan, W. H. Lim, A systematic literature review of 3D deep learning techniques in computed tomography reconstruction, Tomography 9 (6) (2023) 2158–2189. doi:10.3390/tomography9060169.

[249] S. Bellens, P. Guerrero, P. Vandewalle, W. Dewulf, Machine learning in industrial X-ray computed tomography–a review, CIRP Journal of Manufacturing Science and Technology 51 (2024) 324–341.

[250] L. R. Koetzier, D. Mastrodicasa, T. P. Szczykutowicz, N. R. van der Werf, A. S. Wang, V. Sandfort, A. J. van der Molen, D. Fleischmann, M. J. Willemink, Deep learning image reconstruction for CT: technical principles and clinical prospects, Radiology 306 (3) (2023) e221257.

[251] H. Villarraga-Gómez, C. Frederick, P. Brackman, A. Andreyev, Y. Trenikhina, N. Johnson, H. Bale, Non-destructive characterization of additive manufacturing components with computed tomography and 3D X-ray microscopy, in: 13th Conference on Industrial Computed Tomography (iCT), Wels, Austria, 2024.

[252] H. Villarraga-Gómez, K. Crosby, M. Terada, M. N. Rad, Assessing electronics with advanced 3D X-ray imaging techniques, nanoscale tomography, and deep learning, Journal of Failure Analysis and Prevention (2024) 1–16.

[253] R. L. Mitchell, A. Holwell, G. Torelli, J. Provis, K. Selvaranjan, D. Geddes, A. Yorkshire, S. Kearney, Cements and concretes materials characterisation using machine-learning-based reconstruction and 3D quantitative mineralogy via X-ray microscopy, Journal of Microscopy 294 (2) (2024) 137–145. doi:10.1111/jmi.13278.

[254] C. Zhang, G. Zhu, J. Fu, A deep learning reconstruction method for fast assembly line computed tomography, in: 2021 IEEE International Conference on Electrical Engineering and Mechatronics Technology (ICEEMT), IEEE, 2021, pp. 748–752.

[255] C. Hai, J. He, B. Li, P. He, L. Sun, Y. Wu, M. Yang, Dual-domain metal trace inpainting network for metal artifact reduction in baggage CT images, Measurement 207 (2023) 112420. doi:https://doi.org/10.1016/j.measurement.2022.112420.

[256] A. Ziabari, S. V. Venkatakrishnan, Z. Snow, A. Lisovich, M. Sprayberry, P. Brackman, C. Frederick, P. Bhattad, S. Graham, P. Bingham, et al., Enabling rapid X-ray CT characterisation for additive manufacturing using CAD models and deep learning-based reconstruction, npj Computational Materials 9 (1) (2023) 91.

[257] P. Moonen, J. Dhaene, J. Van den Bulcke, M. N. Boone, L. Van Hoorebeke, Calibration-free retrieval of density information from computed tomography data, Precision Engineering 76 (2022) 377–384.

[258] F. Spiers, Effective atomic number and energy absorption in tissues, The British journal of radiology 19 (218) (1946) 52–63.

[259] R. Murty, Effective atomic numbers of heterogeneous materials, Nature 207 (4995) (1965) 398–399.

[260] M. Taylor, R. Smith, F. Dossing, R. Franich, Robust calculation of effective atomic numbers: the auto-Z_{eff} software, Medical Physics 39 (4) (2012) 1769–1778.

[261] A. Bonnin, P. Duvauchelle, V. Kaftandjian, P. Ponard, Concept of effective atomic number and effective mass density in dual-energy X-ray computed tomography, Nuclear Instruments and Methods in Physics Research Section B: Beam Interactions with Materials and Atoms 318 (2014) 223–231.

[262] M. Van Geet, R. Swennen, M. Wevers, Quantitative analysis of reservoir rocks by microfocus X-ray computerised tomography, Sedimentary Geology 132 (1-2) (2000) 25–36.

[263] Oxford Reference, Artificial intelligence, accessed: 2024-08-29.
URL https://www.oxfordreference.com/display/10.1093/oi/authority.20110803095426960

[264] A. Nelson, Dictionary of Mining, Philosophical Library, 1965.

[265] F. Milletari, N. Navab, S.-A. Ahmadi, V-net: Fully convolutional neural networks for volumetric medical image segmentation, in: 2016 Fourth International Conference on 3D Vision (3DV), 2016, pp. 565–571. doi:10.1109/3DV.2016.79.

[266] S. Krig, Computer Vision Metrics: Textbook Edition, Springer International Publishing, 2016.

[267] S. Kurgalin, S. Borzunov, A practical approach to high-performance computing, Springer International Publishing, 2019.

[268] J. Petersen, Heap leaching as a key technology for recovery of values from low-grade ores – a brief overview, Hydrometallurgy 165 (2016) 206–212. doi:https://doi.org/10.1016/j.hydromet.2015.09.001.

- this page is intentionally left blank -

Contributions not related to this thesis

Conference presentations and abstracts

A. Özarslan, L. T. Krebbers, M. Bilen, R. M. Akmaz, B. G. Lottermoser, Preliminary assessment of graphite resources in Turkey, in: Sustainable Development in the Minerals Industry, 10th International Conference, 15 - 20 September 2022, Windhoek (Namibia).

R. Alvarado, T. Wintges, V. Linnemann, A. Garcia, L. Krebbers, O. Frederic, Investigation of hydraulic conductivity on permeable pavement bonded with a novel polyurethane binder, in: 16th International Conference on Urban Drainage (ICUD), 9-14 June 2024, Delft (The Netherlands).

- this page is intentionally left blank -

Supplementary material

The supplementary material of this thesis contains acquisition protocols, numerical raw and processed data of each study. It is stored on the attached SD card.